Clean ballistic quantum point contact in $SrTiO_3$

Evgeny Mikheev,[1,2] Ilan T. Rosen,[3,2] Johannes Kombe,[4] François Damanet,[5] Marc A. Kastner,[1,2,6] and David Goldhaber-Gordon[1,2]

[1]*Department of Physics, Stanford University, Stanford, CA 94305, USA*
[2]*Stanford Institute for Materials and Energy Sciences, SLAC National Accelerator Laboratory, Menlo Park, CA 94025, USA*
[3]*Department of Applied Physics, Stanford University, Stanford, CA, 94305, USA*
[4]*Department of Physics and SUPA, University of Strathclyde, Glasgow G4 0NG, United Kingdom.*
[5]*Institut de Physique Nucléaire, Atomique et de Spectroscopie, CESAM, University of Liège, B-4000 Liège, Belgium*
[6]*Department of Physics, Massachusetts Institute of Technology, Cambridge, MA 02139, USA*

Two dimensional electron gases based on $SrTiO_3$ are an intriguing platform for exploring mesoscopic superconductivity combined with spin-orbit coupling, offering electrostatic tunability from insulator to metal to superconductor within a single material. So far, however, quantum effects in $SrTiO_3$ nanostructures have been complicated by disorder. Here we introduce a facile approach to achieving high mobility and patterning gate-tunable structures in $SrTiO_3$, and use it to demonstrate ballistic constrictions with clean normal state conductance quantization. Conductance plateaus show two-fold degeneracy that persists to magnetic fields of at least 5 T – far beyond what one would expect from the $g-$factor extracted at high fields – a potential signature of electron pairing extending outside the superconducting regime.

Advances in the cleanliness of low-dimensional electron systems are typically produced by painstaking optimization of material quality. But occasionally, simplification of fabrication flows or material synthesis can play a key role. One prominent example is the invention of the mechanical exfoliation method to isolate monolayer graphene [1], a non-resource-intensive technique that democratized access to high quality 2D systems rich with new physics. In the same spirit, here we present a widely accessible fabrication method for a clean, ballistic quantum system in $SrTiO_3$, a material known for its rich physics [2–4]. We forgo the expensive and complex epitaxial growth techniques typically used to achieve high mobility in dimensional electron gases (2DEGs), using only commercially available single crystals, standard ionic liquid gating, electron beam lithography, and widely available, low-temperature deposition techniques: sputtering and atomic layer deposition.

Development of clean quantum systems is a central goal in condensed matter physics and materials science, driven in part by the promise of large-scale quantum computing. Architectures for solid-state quantum computing [5, 6] often involve superconductivity and nanoscale patterning, and can benefit from electrostatic tunability (as in gatemons [7, 8].) For topological qubits [9, 10], these three elements are required, along with spin-orbit coupling. A challenge for all routes towards large-scale quantum computation is in mitigating disorder, dissipation, and noise [5], which prevent high-fidelity quantum state control. Disorder-induced localized states are particularly problematic for demonstrating topological qubits, as they can mimic the most easily detectable signatures of Majorana states [10, 11].

The predominant approach for combining gate tunability and superconductivity is through proximitization of a high-mobility semiconductor (e.g. InAs, InSb) by a metallic superconductor (e.g. Al, Nb). Despite major progress in improving interfaces between such dissimilar materials, they remain major sources of the types of imperfections mentioned above [9].

An alternative approach is to construct a monolithic quantum system from a single material that inherently possesses the full collection of desired properties – superconducting pairing, spin-orbit coupling, gate-tunable chemical potential, low dimensionality – obviating the need for coupling across interfaces between dissimilar materials. One such material is the oxide perovskite $SrTiO_3$: a wide-band gap insulator in the undoped state, which transitions upon electron doping into an electrostatically-tunable superconductor. At present, this route faces basic nanofabrication challenges: whereas 2D electron gases (2DEGs) with high electron mobility of order 10^4 cm^2/Vs have been demonstrated in micron-scale $SrTiO_3$-based Hall bars and unpatterned samples [12–15], shaping them into nanostructures without degrading the system's cleanliness has been difficult.

Several reports to date used nanopatterned split gates [16–21] or nanopatterned hard masking of $LaAlO_3$ [22–25] to define a narrow constriction in a $SrTiO_3/LaAlO_3$ 2DEG. Recently, we reported studies of a quasi-ballistic superconducting constriction in $SrTiO_3$, formed by using nanopatterned split gates to locally screen surface doping by an ionic liquid (IL) [26]. Some of these efforts detected signs of quantization in constriction conductance [20, 22, 26] and/or critical supercurrent [26]. But like most studies of $SrTiO_3$ 2DEG-based devices reported to date [16–20, 22–26], these have been restricted to the quasi-ballistic regime (electron mean free path comparable to device length). A parallel approach is to use a voltage-biased scanning probe tip to "write" patterns by locally triggering a metal insulator transition in a $SrTiO_3/LaAlO_3$ heterostructure that is fine-tuned to the verge of this transition [27]. This was successful in demonstrating feasibility of clean, quantized behavior in the normal state of $SrTiO_3$ [28, 29]. To our knowledge, a comparable level of clean ballistic transport has not been reproduced by other groups, likely due to the required fine tuning of material properties and writing process parameters.

In this work, we report a small but transformative mod-

This is a peer-reviewed, accepted author manuscript of the following article: Mikheev, E., Rosen, I. T., Kombe, J., Damanet, F., Kastner, M. A., & Goldhaber-Gordon, D. (2023). A clean ballistic quantum point contact in strontium titanate. Nature Electronics, 6(6), 417–424. https://doi.org/10.1038/s41928-023-00981-5

ification to the fabrication flow reported in [26] for a quantum constriction in $SrTiO_3$. The mean free path in the adjacent electron reservoir is improved by an order of magnitude, bringing it into the clean ballistic regime. Working in the non-superconducting state, charge transport across the constriction shows unambiguous signatures of a discretized electronic subband spectrum.

The electronic cleanliness of both the constriction and the adjacent 2DEG allows for observation of intriguing interplay between mesoscopic device physics and the unusual material properties of $SrTiO_3$. We demonstrate that our device is in an unconventional regime of comparable vertical and lateral confinement, owing to electron mass anisotropy, resulting in an unusual sequence of subband degeneracies that are intermittent in magnetic field. Additionally, we observe in the constriction subband spectrum striking persistence of two-fold (presumably spin) degeneracy to high magnetic field before it eventually splits. This phenomenology is consistent with that reported in scanned probe-written wires [28, 41], and with the theoretical explanation in terms of attractive electron-electron interaction supporting short-range superconducting correlations without long-range superconducting order [41, 42]. Finally, the increased cleanliness of these new structures coincides with a surprising absence of long-range superconducting order in both the leads and the constriction, whereas it is commonly observed at the same carrier densities in very similar devices with more disorder [26]. The microscopic mechanism of superconducting pairing in $SrTiO_3$ is an important and difficult open question. Many non-BCS scenarios are being considered, including pairing by critical fluctuations from a nearby ferroelectric quantum critical point [4]. This work opens paths to test theoretical proposals using mesoscale probes, controlled 2DEG confinement, and deliberate crossovers between dirty and clean limits.

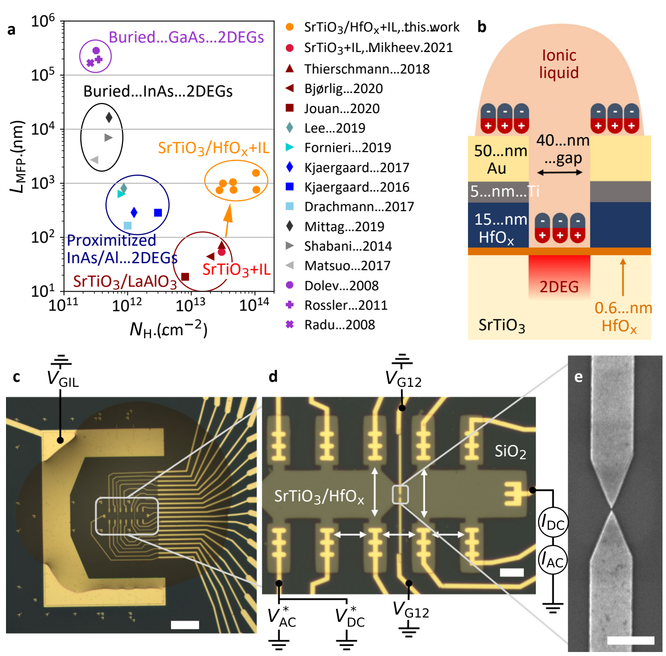

FIG. 1. **Clean and nanopatternable 2DEG in $SrTiO_3$.** (a) Mean free path plotted against Hall density in 2DEGs with nanopatterned constrictions or wires, comparison with references [19–21, 26, 30–40]. (b) Schematic cross-section of the constriction region. (c,d) Optical and (e) scanning electron microscopy images of the devices. Arrows in (d) indicate the measured potential differences between voltage probes. Scale bars in (c,d,e) are 100, 10 and 1 μm, respectively.

Patterning a clean 2DEG in $SrTiO_3$

The key enabler for this experiment is combining 1) nanoscale control of the channel width through nanopatterned local dielectric gates and 2) an ultrathin barrier layer between the $SrTiO_3$ 2DEG channel and the ionic liquid. The latter dramatically reduces disorder levels in both unpatterned channels and narrow constrictions. Including a few-layer hexagonal boron nitride (hBN) barrier was previously found to improve electron mobility by an order of magnitude in ionic liquid-gated $SrTiO_3$ [14]. The likely causes are blocking electrochemical reactions and reducing scattering from charge disorder in the ionic liquid [14, 43].

Large few-layer flakes of hBN are difficult to obtain by exfoliation, and fragile during subsequent fabrication. Here, we introduce ultrathin amorphous HfO_x deposited by atomic layer deposition (ALD) as a more repeatable and robust alternative barrier layer, enabling integration with nanopatterned HfO_x/Ti/Au split gates. These gates define the quantum constriction (Fig. 1) by selectively screening electric fields from the ionic liquid and thus spatially patterning electron accumulation in the $SrTiO_3$. Initially, the device channel is completely insulating. But a large 2D electron density at the oxide surface can be accumulated and subsequently tuned by the voltage V_{GIL} applied to the large side gate (Fig. 1c) above 220 K. Below this temperature, the ionic liquid is frozen and so the charge density in the $SrTiO_3$ is only weakly affected by adjustments in side gate voltage.

The main device discussed in this report has been thermally cycled three times between near room temperature and 30 mK, with V_{GIL} adjusted each time near room temperature to tune global 2D carrier density. At base temperature, the measured Hall densities in the unpatterned 2DEG regions (Fig. 1d) were $N_{\mathrm{H}} = 10.4$, 3.0, and 4.6×10^{13} cm^{-2}, respectively. The Hall mobilities μ_{H} were near 10^4 cm^2/Vs for all three cooldowns, on par with the highest values reported for unpatterned $SrTiO_3/LaAlO_3$ 2DEGs [12, 13, 15, 44], and ionic liquid-gated $SrTiO_3$/hBN [14]. To enable these measurements, the constriction was tuned to an open (many-channel) state by applying split-gate voltage V_{G12}=0.8 V.

A useful metric for disorder in mesoscopic devices is the comparison between device length L and the electron mean free path L_{MFP} between scattering events. The latter can be estimated as a product of Fermi velocity and time between scattering: $L_{\mathrm{MFP}} = v_{\mathrm{F}}\tau = \mu_{\mathrm{H}} e^{-1}\hbar\sqrt{2\pi N_{\mathrm{H}}} = 0.8$-2 μm in our measurements. This is an order of magnitude larger than the constriction, whose lithographic width is 40 nm, a first indication that the constriction is in the clean ballistic regime ($L \ll L_{\mathrm{MFP}}$).

Figure 1 illustrates that this is an order of magnitude improvement from our previous report on quasi-ballistic ($L \approx L_{\mathrm{MFP}}$) constrictions in ionic liquid-gated $SrTiO_3$ with $L_{\mathrm{MFP}} = 55$ nm. Similarly, in recent reports on gate-

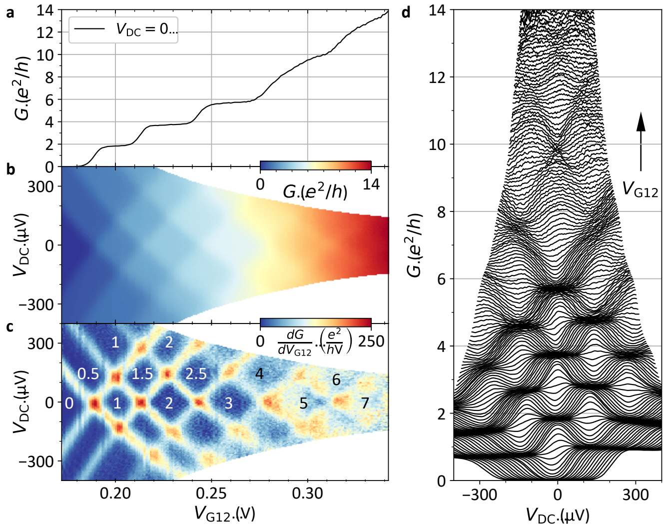

FIG. 2. **DC bias spectroscopy of the quantum point contact.** (a) Zero bias conductance trace with split gate voltage $V_{\rm G12}$. (b,c) Conductance and transconductance maps with $V_{\rm G12}$ and $V_{\rm DC}$. The numbers of spin-degenerate ballistic modes indicated by $G/(2e^2/h)$ are shown in (c). (d) G traces in $V_{\rm DC}$ at fixed $V_{\rm G12}$. All data shown are at $B = 5$ T, and are from the cooldown with $N_H = 4.6 \times 10^{13}$ cm^{-2}.

defined nanostructures in $SrTiO_3/LaAlO_3$ 2DEGs, $L_{\rm MFP}$ is typically 20-70 nm [19–21]. State of the art III-V semiconductor heterostructures can support gate-patternable 2DEGs with $L_{\rm MFP}$ of hundreds of μm in GaAs [38–40], and tens of μm in InAs [35–37]. However, if we aspire to achieve superconducting pairing in a III-V material, the 2DEG must be brought close to the heterostructure surface to allow proximitization by a superconducting metal. Scattering dramatically increases as a result: InAs-based epitaxially proximitized 2DEGs (with the superconductor subsequently removed) typically have $L_{\rm MFP}$ = 200-800 nm [30–34].

Based on comparison of disorder metrics from unpatterned normal state 2DEG transport, our devices are competitive with state-of-the-art InAs heterostructures designed for proximitization. To our knowledge, this work is a first realization of a ballistic constriction in a $SrTiO_3$ 2DEG that is clean enough to exhibit quantum oscillations, see Methods section and Extended Data Fig. 1a

Quantum transport across the constriction

Fig. 2 presents evidence for clean, ballistic quantum point contact (QPC) behavior in the gate-defined constriction. Fig. 2a shows constriction conductance G as a function of voltage $V_{\rm G12}$ on the split gates, at T = 32 mK, and in magnetic field B = 5 T normal to the 2DEG plane. The zero-bias G trace shows plateaus at integer multiples (n = 1, 2, 3) of the conductance quantum $\delta G = 2e^2/h$. This is a hallmark of a ballistic constriction with a discretized transverse momentum spectrum. Transitions between plateaus in G indicate the chemical potential crossing discrete subbands, corresponding to individual spin-degenerate ballistic modes. Subband onsets are signaled by peaks in transconductance $dG/dV_{\rm G12}$.

Fig. 2b and 2c show a "diamond" pattern in either G or $dG/dV_{\rm G12}$ as a function of gate voltage and DC bias $V_{\rm DC}$ added to the small AC excitation. Increasing the asymmetry of chemical potential between the left and right contact to the constriction eventually results in uneven occupation of ballistic subbands on the two sides. As a function of $V_{\rm DC}$, measured G alternates between adjacent integer (0, 1, 2, ...) and half-integer (0.5, 1.5, 2.5, ...) multiples of $2e^2/h$. Clean definition of such higher order plateaus is an indication of high quality and adiabaticity of the QPC [37, 40, 45].

Several sequences of higher order plateaus are clearly observable in the diamond pattern of G or $dG/dV_{\rm G12}$ (Fig. 2b,c), and in the crowding of line traces near integer multiples of e^2/h (Fig. 2d). For the first three subbands (up to $6e^2/h$), the pattern is regular and free of fluctuations typically present in the quasi-ballistic regime [19, 20, 26, 46]. Qualitatively, the diamond pattern definition seen here matches that of state of the art III-V QPC's [37], except some on deeply buried GaAs 2DEGs with hundreds of micron $L_{\rm MFP}$ [40].

There are, however, two unusual features in Fig. 2: first, the observed subbands are doubly degenerate (the G increment is $2e^2/h$), despite a field B = 5 T that would typically spin polarize subbands (each associated with an e^2/h increment in G). Second, some plateaus appear to be skipped, e.g. $G = 8$ and $12e^2/h$ at zero bias, implying an even higher level of degeneracy.

Both of these irregularities are clarified by considering an orthogonal cut in the parameter space shown in Fig. 3: the map of G dependence on B and $V_{\rm G12}$ at zero bias. Throughout this figure, $V_{\rm G12}$ is converted into chemical potential μ using the height of transconductance diamonds in $V_{\rm DC}$ to quantify the split gate lever arms (see supplementary section S2A for details). Examination of the first conductance step in line traces of G (Fig. 3a) or maps of $dG/d\mu$ (Fig. 3b-d) shows that the two-fold degeneracy of the first conductance steps persists up to $B \approx 7$ T. At higher B, the two-fold degeneracy is broken and the first few conductance step sizes become e^2/h. Separately, two distinct flavors of subbands are distinguishable at low B: those fast- and slow-moving in B. The slow-moving set of subbands become the lowest subbands for B above a few Tesla, and are responsible for the well-defined QPC behavior in Fig. 2. The fast-moving subbands cross the slow-moving ones, producing intermittent quadruple degeneracies, such as those at $G = 8$ and $12e^2/h$ in Fig. 2.

The physics of the different subband flavors can be captured by an extension of the classic 2D saddle potential model of a QPC [47] to a three-dimensional confinement potential [28, 48]. The 3D saddle potential is quadratic in the longitudinal (x), transverse (y), and vertical (z) directions (Fig. 4a) with polarity $P_x = -1$, $P_{y,z} = 1$. At zero magnetic field, this leads to characteristic energy $\epsilon_u(B{=}0) = \hbar\omega_u = \hbar^2/(m_u^* l_u^2)$ for each direction u, where l_u is the natural length scale and m_u^* is the electron mass along that direction. The momentum operators are $-i\hbar\partial/\partial u$. The resulting Hamiltonian is

$$\mathcal{H} = \sum_{u=x,y,z} \left(-\frac{\hbar^2}{2m_u^*} \cdot \frac{\partial^2}{\partial u^2} + P_u \frac{m_u^* \epsilon_u^2 u^2}{2\hbar^2} \right) + E_Z \sigma_z, \quad (1)$$

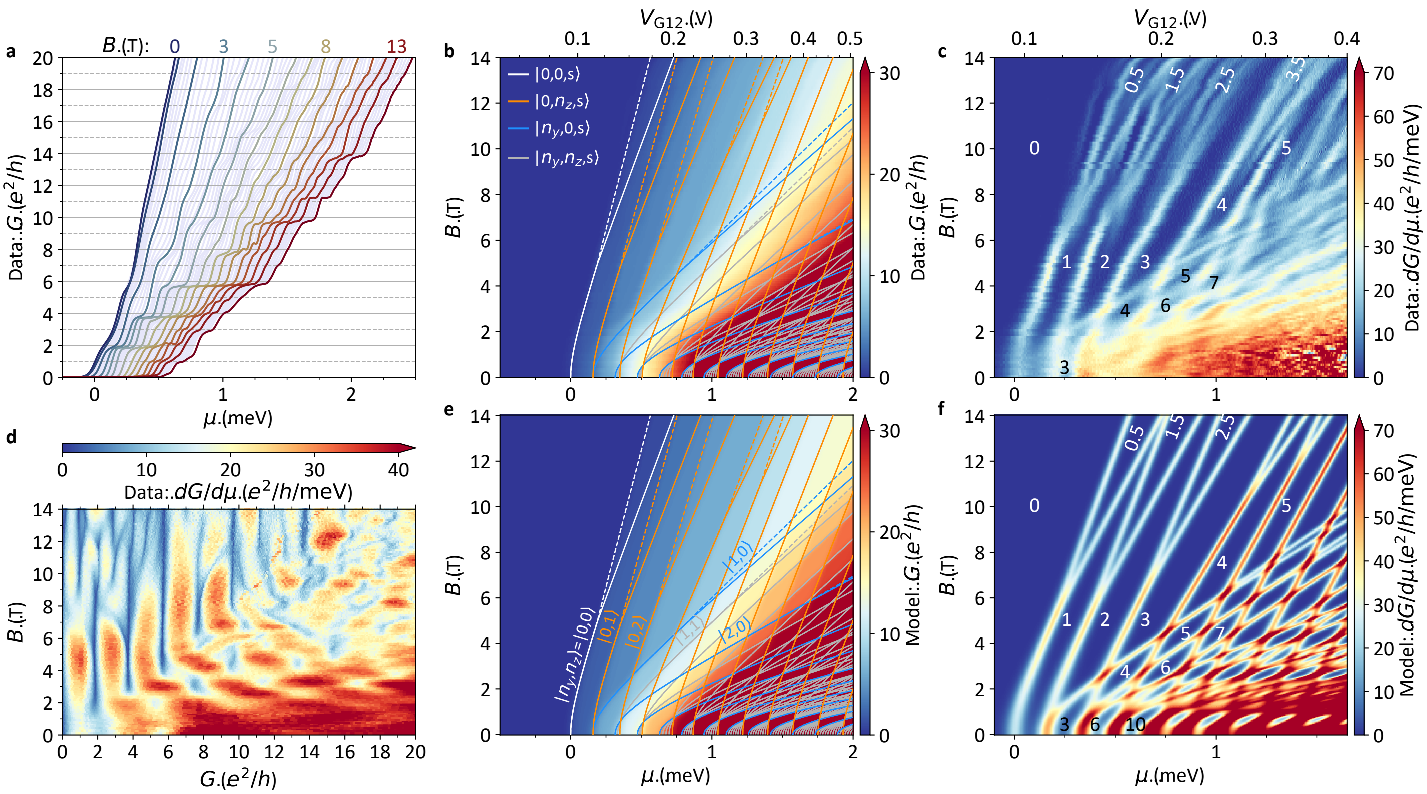

FIG. 3. **Subband evolution in magnetic field.** (a) zero-bias conductance G as a function of gate voltage V_{G12} (converted to chemical potential μ), with magnetic field B tuned between 0 and 14 T. Same data is shown as maps of (b) G and (c) transconductance $dG/d\mu$ with with μ and B. (d) The parametric map of $dG/d\mu$ with B and G emphasizes persistence of robust $2e^2/h$ quantization up to B of at least 5 T. (e,f) Simulation using a non-interacting model (equations 1 and 2) of (e) G and (f) $dG/d\mu$ matched to data in (b,c). Lines in (b,e) are $|n_y, n_z, s\rangle$ subband energies from the model after fitting. Number of spin degenerate ballistic modes is labeled on G plateau regions in (c,f).

where $E_Z = g\mu_B sB$ is the Zeeman energy, s is the spin, and σ_z is the Pauli matrix.

For a non-zero magnetic field oriented along the z direction, the cyclotron frequency $\hbar\omega_c = eB/m^*$ renormalizes the $x-y$ plane confinement [47, 48]: $\epsilon_x = \hbar\omega_x/(1+\omega_c^2/\omega_y^2)^{1/2}$, $\epsilon_y = \hbar(\omega_y^2+\omega_c^2)^{1/2}$, without affecting ϵ_z. The Hamiltonian in equation (1) is separable into $y-z$ subband wavefunctions discretized according to quantum numbers $|n_y, n_z, s\rangle$, and an x wavefunction component that broadens these subbands. Integers $n_{y,z} \geq 0$ and $s = \pm 1/2$ give the subband energy spectrum:

$$\epsilon_{yz} = \epsilon_y\left(n_y + \frac{1}{2}\right) + \epsilon_z\left(n_z + \frac{1}{2}\right) + E_Z(B, s), \quad (2)$$

where the standard description of the Zeeman effect is $E_Z(B, s) = g\mu_B sB$, resulting in spin splitting at any finite B. To account for the observed persistence of two-fold degeneracy, we empirically modify the Zeeman energy as $E_Z(B, s) = g\mu_B s(B - B_P)$ for $B \geq B_P$ and $E_Z(B, s) = 0$ for $B < B_P$, where B_P is a phenomenological field scale.

Given subband energy ϵ_{yz}, the subband contributes conductance $G(\mu) = e^2/h$ for $\mu \gg \epsilon_{yz}$, and no conductance for $\mu \ll \epsilon_{yz}$. The width of the transition is ϵ_x. Fig. 3e,f show the conductance modeled in this way. Simulation parameters were extracted by individually fitting the position of lowest-lying subbands, giving $m_y^* = 0.8$-$1.1m_e$, $\hbar\omega_{x,y,z} =$ 0.11, 0.16, 0.13-0.21 meV, respectively, $g = 0.22$-0.37, and B_P increasing from 5 T to above 14 T for higher lying subbands. For extensive discussion of the analysis procedure, including similar data from a different cooldown (3.0×10^{13} cm^{-2}) with B_P ranging from 4 T to above 14 T, see supplementary section S2C.

The model both captures and clarifies the essential features of the experimental data: the subbands that are slow-moving in B belong to the $|n_y{=}0, n_z, s{=}\pm 1/2\rangle$ series, while all bands with $n_y > 0$ are fast-moving in B due to renormalization of ϵ_y by the cyclotron frequency $\hbar\omega_c$. Our device is in an unusual regime with comparable lateral and vertical confinement ($\omega_y \approx \omega_z$), and B of a few Tesla isolates the subbands generated by ω_z as lowest lying. This contrasts with most conventional realizations of QPCs, where $\omega_z \gg \omega_y$ and only lateral confinement is relevant for the description of lowest subbands [47]. In our case the spacing between split gates (40 nm) is not dramatically larger than the finite vertical extent of the 2DEG (usually estimated in the 1-15 nm range depending on carrier density [49, 50]), and the anisotropic mass $m_z^* > m_y^*$ enhances ω_y relative to ω_z.

The second unusual aspect of our device is the persistence of two-fold degeneracy up to $B_P \geq 5$ T. Fig. 4b illustrates the difference from the conventional pattern of spin splitting. The shape of the subband splitting is a "Y"

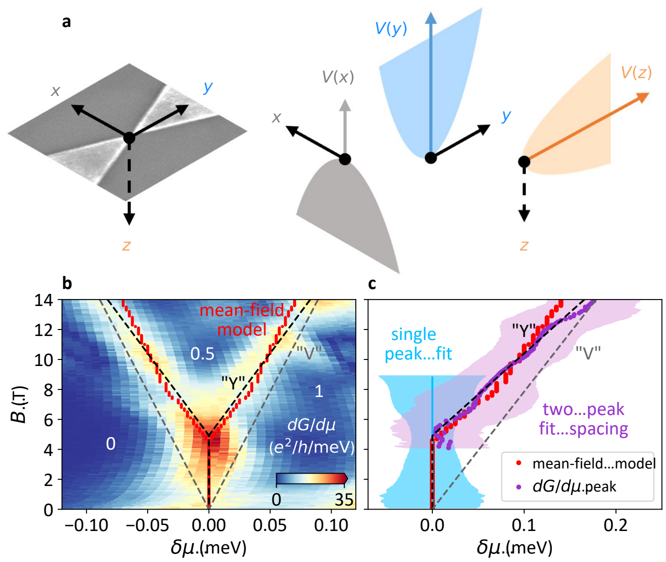

FIG. 4. **Understanding constriction conductance.** (a) Illustration of 1D cuts in the 3D confinement potential used to simulate G and $dG/d\mu$ maps in Fig. 3e and f (details in text). (b) $dG/d\mu$ map centered at the lowest lying subband by subtracting a B-dependent offset in μ. Dashed lines illustrate a "Y"-shaped subband splitting with $g = 0.32$, $B_P = 4.9$ T, and a "V" shape with $g = 0.22$, $B_P = 0$ T. Red circle symbols show conductance plateau boundaries in the mean field model that includes an electron pairing interaction (full details in supplementary section S2E). (c) Same parameters are used to plot the spin splitting in "V", "Y"-shape and mean field models. Purple circle symbols show experimentally observed spacing between $s = \pm 1/2$ subbands, extracted from double peak fitting to $dG/d\mu$. Shading shows broadening from both single and double peak fitting (added together in the latter case).

in $\mu - B$ space, in contrast to the "V" shape of standard Zeeman splitting (corresponding to $B_P = 0$). For small g-factors subband broadening can complicate distinguishing between a "Y" shape and a "V" shape. For example, apparent spin degeneracy up to $B \approx 9$ T has been observed in quantum wires based on hole-doped GaAs, where spin-orbit coupling creates a strong anisotropy in g [51]. Qualitatively, our data appear much more consistent with a "Y" rather than a "V" shape, with $s = \pm 1/2$ subbands sticking together until B_P. Quantitative fitting of $dG/d\mu$ at fixed B to single and double peak shapes (Fig. 4c) further corroborates our interpretation that $B_P > 0$ is not an artifact of subband broadening. In supplementary section S2C, we detail two separate approaches to quantify B_P: fitting two peaks to $dG/d\mu$ at each field, then finding the field at which extracted peak spacing extrapolates to zero (markers in Fig. 4c); and fitting a single peak to $dG/d\mu$ at each field, then finding the field at which this width is minimized (blue shaded region in Fig. 4c). These two approaches yield consistent results.

Similar "Y" shapes have been reported in other contexts in $SrTiO_3/LaAlO_3$-based nanostructures: in the Coulomb blockade levels of quantum dot wires written by biased atomic force microscope (AFM) tips [41], and in accidental quantum dots in split-gate QPCs [21, 46]. Double degeneracy of subbands in high fields has also recently been reported in AFM-written ballistic wires [28, 52]. Our data appear even clearer, and show that the phenomenology is not specific to $SrTiO_3/LaAlO_3$.

A compelling explanation for these observations invokes a phenomenological attractive ("negative-U") interaction between electrons, conceptually analogous to pairing interactions responsible for superconductivity [41, 42, 46]. In Fig. 4b and c, red circle symbols show G plateau boundaries in a mean-field model [42] for a 1D wire with an attractive interaction. The "Y" shape was closely reproduced by adjusting U and fixing $\omega_{y,z}$, $m_{y,z}$, g to values from the non-interacting model fits (see supplementary section S2E for simulation details). In this picture, B_P is the field at which the pairing interaction (favoring spin singlets) is balanced by Zeeman energy (favoring alignment of spins). The critical field and temperature scales in our experiment and several previous reports [28, 41, 46] are higher than any plausible upper bounds for globally coherent superconductivity in the 2DEG. This may reflect pre-formed pairs which then condense at a lower temperature, or pairing that is locally enhanced at ferroelastic domain walls or valence-skipping defects [46, 53].

The observed splitting of the "Y" above B_P gives g-factor values of 0.18-0.36 across all cooldowns, lower than other values reported in $SrTiO_3$ [21, 28, 41]. Experiments suggestive of pairing in ballistic wires yielded some of the lowest previous g-factor values in $SrTiO_3$, $g \approx 0.6$ [28]. A likely explanation is that strongly reduced g emerges in presence of significant atomic spin-orbit coupling, and comparable confinement in both z and y directions (see supplementary section S2D). Rashba spin-orbit coupling can also affect and possibly reduce E_Z through avoided crossings between closely-spaced subbands [54, 55].

When energy scales for confinement in the y and z directions are comparable, eq. (2) naturally leads to near-degenerate clustering of subbands with common $n = n_y + n_z$. The number of ways to partition between n_y and n_z, and hence the number of subbands in a cluster, grows with n. A corresponding "Pascal series" quantization pattern $G/(e^2/h) = 0, 1, 3, 6, 10, \ldots$ was observed in AFM-written $SrTiO_3$ nanowires [29]. In most of the devices studied, the mode spacing differed by 50 to 90% between the y and z directions, but at specific values of magnetic field normal to the sample surface a combination of Zeeman splitting and field-enhanced y confinement produced equal mode spacing. To explain apparent persistence of the Pascal conductance series over a finite field range the authors invoked interaction-driven subband locking. In our case, $\omega_y \approx \omega_z$, explaining Pascal-like quantization seen at $B = 0$ with additional two-fold degeneracy since Zeeman splitting is absent: $G/(2e^2/h) = 0, 1, 3, 6, 10, \ldots$ (see model output in Fig. 3f, data in Extended Data Fig. 3 (a $B = 0$ linecut through Fig. 3c), and supplementary sections S2B,C). Though our model has phenomenological pairing interactions as noted above, these do not influence the modeled conductance at $B = 0$.

Conclusion

Quantized plateaus in Figs. 2 and 3 present unambiguous evidence of clean ballistic transport through a nanopatterned region of a clean $SrTiO_3$-based 2DEG. The resulting quantum point contact behavior is unusual in two ways. A two-fold (presumably spin) degeneracy persists in magnetic field up to $B_P \geq 5$ T. Competition between comparable lateral and vertical confinement within the constriction results in higher order subband crossings that are intermittent in magnetic field.

The clean observation of these effects is enabled by advances in fabrication, without major material or process optimization. Our process is entirely based on commercially available single crystals and widely-available cleanroom-based fabrication and deposition tools (ALD and sputtering). In contrast to other approaches to nanodevice fabrication in $SrTiO_3$ [16, 17, 19–21, 23–25, 28, 41, 46], our method does not require specialized epitaxial deposition at high temperature and/or in ultra high vacuum, such as pulsed laser deposition of $LaAlO_3$ on $SrTiO_3$. Such steps are a bottleneck for device fabrication, and a source of device-to-device variability. The most specialized aspect of our approach is the use of ionic liquid gating, a cost-effective technique that has been successfully implemented in many research groups to tune carrier density in a wide variety of materials [56].

We have shown initial, exploratory steps in the development of this material as a clean mesoscopic platform. A huge parameter space remains to be explored, notably in aiming to recover a globally coherent superconducting order parameter. Replacing HfO_x with an epitaxial wide-band-gap perovskite may further improve device cleanliness. The choice of barrier layer material could also add or adjust functionalities such as magnetic spin order or spin-orbit coupling. For the channel layer, tailoring the vertical confinement through heterostructuring and band engineering is an important direction to explore. We also anticipate that our approach can be implemented in $KTaO_3$ (111)-based 2DEGs, where electrostatically tunable superconductivity with T_c up to ≈ 2 K has recently been discovered [57, 58].

[1] K. S. Novoselov, A. K. Geim, S. V. Morozov, D. Jiang, Y. Zhang, S. V. Dubonos, I. V. Grigorieva, and A. A. Firsov, Electric field effect in atomically thin carbon films, Science **306**, 666 (2004).

[2] Y.-Y. Pai, A. Tylan-Tyler, P. Irvin, and J. Levy, Physics of $SrTiO_3$-based heterostructures and nanostructures: a review, Reports on Progress in Physics **81**, 036503 (2018).

[3] C. Collignon, X. Lin, C. W. Rischau, B. Fauqué, and K. Behnia, Metallicity and superconductivity in doped strontium titanate, Annual Review of Condensed Matter Physics **10**, 25 (2019).

[4] M. N. Gastiasoro, J. Ruhman, and R. M. Fernandes, Superconductivity in dilute $SrTiO_3$: A review, Annals of Physics **6**, 168107 (2020).

[5] N. P. de Leon, K. M. Itoh, D. Kim, K. K. Mehta, T. E. Northup, H. Paik, B. Palmer, N. Samarth, S. Sangtawesin, and D. Steuerman, Materials challenges and opportunities for quantum computing hardware, Science **372** (2021).

[6] A. Gyenis, A. Di Paolo, J. Koch, A. Blais, A. A. Houck, and D. I. Schuster, Moving beyond the transmon: Noise-protected superconducting quantum circuits, PRX Quantum **2**, 030101 (2021).

[7] T. W. Larsen, K. D. Petersson, F. Kuemmeth, T. S. Jespersen, P. Krogstrup, J. Nygård, and C. M. Marcus, Semiconductor-nanowire-based superconducting qubit, Physical Review Letters **115**, 127001 (2015).

[8] G. De Lange, B. Van Heck, A. Bruno, D. Van Woerkom, A. Geresdi, S. Plissard, E. Bakkers, A. Akhmerov, and L. DiCarlo, Realization of microwave quantum circuits using hybrid superconducting-semiconducting nanowire Josephson elements, Physical Review Letters **115**, 127002 (2015).

[9] R. M. Lutchyn, E. P. A. M. Bakkers, L. P. Kouwenhoven, P. Krogstrup, C. M. Marcus, and Y. Oreg, Majorana zero modes in superconductor–semiconductor heterostructures, Nature Reviews Materials **3**, 52 (2018).

[10] E. Prada, P. San-Jose, M. W. A. de Moor, A. Geresdi, E. J. H. Lee, J. Klinovaja, D. Loss, J. Nygård, R. Aguado, and L. P. Kouwenhoven, From Andreev to Majorana bound states in hybrid superconductor–semiconductor nanowires, Nature Reviews Physics **2**, 575 (2020).

[11] H. Pan and S. D. Sarma, Physical mechanisms for zero-bias conductance peaks in Majorana nanowires, Physical Review Research **2**, 013377 (2020).

[12] Y. Z. Chen, F. Trier, T. Wijnands, R. J. Green, N. Gauquelin, R. Egoavil, D. V. Christensen, G. Koster, M. Huijben, N. Bovet, S. Macke, F. He, R. Sutarto, N. H. Andersen, J. A. Sulpizio, M. Honig, G. E. D. K. Prawiroatmodjo, T. S. Jespersen, S. Linderoth, S. Ilani, J. Verbeeck, G. Van Tendeloo, G. Rijnders, G. A. Sawatzky, and N. Pryds, Extreme mobility enhancement of two-dimensional electron gases at oxide interfaces by charge-transfer-induced modulation doping, Nature Materials **14**, 801 (2015).

[13] F. Trier, G. E. D. K. Prawiroatmodjo, Z. Zhong, D. V. Christensen, M. von Soosten, A. Bhowmik, J. M. G. Lastra, Y. Chen, T. S. Jespersen, and N. Pryds, Quantization of Hall Resistance at the Metallic Interface between an Oxide Insulator and $SrTiO_3$, Physical Review Letters **117**, 096804 (2016).

[14] P. Gallagher, M. Lee, T. A. Petach, S. W. Stanwyck, J. R. Williams, K. Watanabe, T. Taniguchi, and D. Goldhaber-Gordon, A high-mobility electronic system at an electrolyte-gated oxide surface, Nature Communications **6**, 6437 (2015).

[15] K. Rubi, J. Gosteau, R. Serra, K. Han, S. Zeng, Z. Huang, B. Warot-Fonrose, R. Arras, E. Snoeck, M. Goiran, and W. Escoffier, Aperiodic quantum oscillations in the two-dimensional electron gas at the $LaAlO_3/SrTiO_3$ interface, NPJ Quantum Materials **5**, 9 (2020).

[16] S. Goswami, E. Mulazimoglu, L. M. K. Vandersypen, and A. D. Caviglia, Nanoscale electrostatic control of oxide interfaces, Nano Letters **15**, 2627 (2015).

[17] A. M. R. V. L. Monteiro, D. J. Groenendijk, N. Manca, E. Mulazimoglu, S. Goswami, Y. Blanter, L. M. K. Vandersypen, and A. D. Caviglia, Side gate tunable Josephson junctions at the $LaAlO_3/SrTiO_3$ interface, Nano Letters **17**, 715 (2017).

[18] G. E. D. K. Prawiroatmodjo, F. Trier, D. V. Christensen, Y. Chen, N. Pryds, and T. S. Jespersen, Evidence of weak superconductivity at the room-temperature grown $LaAlO_3/SrTiO_3$ interface, Physical Review B **93**, 184504 (2016).

[19] H. Thierschmann, E. Mulazimoglu, N. Manca, S. Goswami, T. M. Klapwijk, and A. D. Caviglia, Transport regimes of a split gate superconducting quantum point contact in the two-dimensional $LaAlO_3/SrTiO_3$ superfluid, Nature Com-

munications **9**, 2276 (2018).

[20] A. Jouan, G. Singh, E. Lesne, D. C. Vaz, M. Bibes, A. Barthélémy, C. Ulysse, D. Stornaiuolo, M. Salluzzo, S. Hurand, J. Lesueur, C. Feuillet-Palma, and N. Bergeal, Quantized conductance in a one-dimensional ballistic oxide nanodevice, Nature Electronics **3**, 201 (2020).

[21] A. V. Bjørlig, D. J. Carrad, G. E. D. K. Prawiroatmodjo, M. Von Soosten, Y. Gan, Y. Chen, N. Pryds, J. Paaske, and T. S. Jespersen, g-factors in $LaAlO_3/SrTiO_3$ quantum dots, Physical Review Materials **4**, 122001 (2020).

[22] A. Ron and Y. Dagan, One-dimensional quantum wire formed at the boundary between two insulating $LaAlO_3/SrTiO_3$ interfaces, Physical Review Letters **112**, 136801 (2014).

[23] E. Maniv, A. Ron, M. Goldstein, A. Palevski, and Y. Dagan, Tunneling into a quantum confinement created by a single-step nanolithography of conducting oxide interfaces, Physical Review B **94**, 045120 (2016).

[24] D. Stornaiuolo, D. Massarotti, R. Di Capua, P. Lucignano, G. P. Pepe, M. Salluzzo, and F. Tafuri, Signatures of unconventional superconductivity in the $LaAlO_3/SrTiO_3$ two-dimensional system, Physical Review B **95**, 140502 (2017).

[25] M. Boselli, G. Scheerer, M. Filippone, W. Luo, A. Waelchli, A. B. Kuzmenko, S. Gariglio, T. Giamarchi, and J.-M. Triscone, Electronic transport in submicrometric channels at the $LaAlO_3/SrTiO_3$ interface, Physical Review B **103**, 075431 (2021).

[26] E. Mikheev, I. T. Rosen, and D. Goldhaber-Gordon, Quantized critical supercurrent in $SrTiO_3$-based quantum point contacts, Science Advances **7**, eabi6520 (2021).

[27] C. Cen, S. Thiel, G. Hammerl, C. W. Schneider, K. E. Andersen, C. S. Hellberg, J. Mannhart, and J. Levy, Nanoscale control of an interfacial metal–insulator transition at room temperature, Nature Materials **7**, 298 (2008).

[28] A. Annadi, G. Cheng, H. Lee, J.-W. Lee, S. Lu, A. Tylan-Tyler, M. Briggeman, M. Tomczyk, M. Huang, D. Pekker, C.-B. Eom, and J. Irvin, P.and Levy, Quantized ballistic transport of electrons and electron pairs in $LaAlO_3/SrTiO_3$ nanowires, Nano Letters **18**, 4473 (2018).

[29] M. Briggeman, M. Tomczyk, B. Tian, H. Lee, J.-W. Lee, Y. He, A. Tylan-Tyler, M. Huang, C.-B. Eom, D. Pekker, R. S. K. Mong, P. Irvin, and J. Levy, Pascal conductance series in ballistic one-dimensional $LaAlO_3/SrTiO_3$ channels, Science **367**, 769 (2020).

[30] M. Kjærgaard, F. Nichele, H. Suominen, M. Nowak, M. Wimmer, A. R. Akhmerov, J. A. Folk, K. Flensberg, J. Shabani, C. J. Palmstrøm, and C. M. Marcus, Quantized conductance doubling and hard gap in a two-dimensional semiconductor–superconductor heterostructure, Nature Communications **7**, 12841 (2016).

[31] M. Kjærgaard, H. J. Suominen, M. P. Nowak, A. R. Akhmerov, J. Shabani, C. J. Palmstrøm, F. Nichele, and C. M. Marcus, Transparent semiconductor-superconductor interface and induced gap in an epitaxial heterostructure Josephson junction, Physical Review Applied **7**, 034029 (2017).

[32] A. C. C. Drachmann, H. J. Suominen, M. Kjaergaard, B. Shojaei, C. J. Palmstrøm, C. M. Marcus, and F. Nichele, Proximity effect transfer from NbTi into a semiconductor heterostructure via epitaxial aluminum, Nano Letters **17**, 1200 (2017).

[33] A. Fornieri, A. M. Whiticar, F. Setiawan, E. Portolés, A. C. Drachmann, A. Keselman, S. Gronin, C. Thomas, T. Wang, R. Kallaher, G. C. Gardner, E. Berg, M. J. Manfra, A. Stern, C. M. Marcus, and F. Nichele, Evidence of topological superconductivity in planar Josephson junctions, Nature **569**, 89 (2019).

[34] J. S. Lee, B. Shojaei, M. Pendharkar, A. P. McFadden, Y. Kim, H. J. Suominen, M. Kjaergaard, F. Nichele, H. Zhang, C. M. Marcus, and C. J. Palmstrøm, Transport studies of Epi-Al/InAs two-dimensional electron gas systems for required building-blocks in topological superconductor networks, Nano Letters **19**, 3083 (2019).

[35] J. Shabani, A. McFadden, B. Shojaei, and C. Palmstrøm, Gating of high-mobility InAs metamorphic heterostructures, Applied Physics Letters **105**, 262105 (2014).

[36] S. Matsuo, H. Kamata, S. Baba, R. S. Deacon, J. Shabani, C. J. Palmstrøm, and S. Tarucha, Magnetic field inducing Zeeman splitting and anomalous conductance reduction of half-integer quantized plateaus in InAs quantum wires, Physical Review B **96**, 201404 (2017).

[37] C. Mittag, M. Karalic, Z. Lei, C. Thomas, A. Tuaz, A. T. Hatke, G. C. Gardner, M. J. Manfra, T. Ihn, and K. Ensslin, Gate-defined quantum point contact in an InAs two-dimensional electron gas, Physical Review B **100**, 075422 (2019).

[38] M. Dolev, M. Heiblum, V. Umansky, A. Stern, and D. Mahalu, Observation of a quarter of an electron charge at the $\nu = 5/2$ quantum Hall state, Nature **452**, 829 (2008).

[39] I. P. Radu, J. B. Miller, C. M. Marcus, M. A. Kastner, L. N. Pfeiffer, and K. W. West, Quasi-particle properties from tunneling in the $\nu = 5/2$ fractional quantum Hall state, Science **320**, 899 (2008).

[40] C. Rössler, S. Baer, E. De Wiljes, P. L. Ardelt, T. Ihn, K. Ensslin, C. Reichl, and W. Wegscheider, Transport properties of clean quantum point contacts, New Journal of Physics **13**, 113006 (2011).

[41] G. Cheng, M. Tomczyk, S. Lu, J. P. Veazey, M. Huang, P. Irvin, S. Ryu, H. Lee, C.-B. Eom, C. S. Hellberg, and J. Levy, Electron pairing without superconductivity, Nature **521**, 196 (2015).

[42] F. Damanet, E. Mansfield, M. Briggeman, P. Irvin, J. Levy, and A. J. Daley, Spin-orbit-assisted electron pairing in one-dimensional waveguides, Physical Review B **104**, 125103 (2021).

[43] T. A. Petach, K. V. Reich, X. Zhang, K. Watanabe, T. Taniguchi, B. I. Shklovskii, and D. Goldhaber-Gordon, Disorder from the bulk ionic liquid in electric double layer transistors, ACS Nano **11**, 8395 (2017).

[44] Y. Xie, C. Bell, M. Kim, H. Inoue, Y. Hikita, and H. Y. Hwang, Quantum longitudinal and Hall transport at the $LaAlO_3/SrTiO_3$ interface at low electron densities, Solid State Communications **197**, 25 (2014).

[45] B. J. van Wees, L. P. Kouwenhoven, E. M. M. Willems, C. J. P. M. Harmans, J. E. Mooij, H. Van Houten, C. W. J. Beenakker, J. G. Williamson, and C. T. Foxon, Quantum ballistic and adiabatic electron transport studied with quantum point contacts, Physical Review B **43**, 12431 (1991).

[46] G. E. D. K. Prawiroatmodjo, M. Leijnse, F. Trier, Y. Chen, D. V. Christensen, M. Von Soosten, N. Pryds, and T. S. Jespersen, Transport and excitations in a negative-U quantum dot at the $LaAlO_3/SrTiO_3$ interface, Nature Communications **8**, 395 (2017).

[47] M. Büttiker, Quantized transmission of a saddle-point constriction, Physical Review B **41**, 7906 (1990).

[48] A. Scherbakov, E. Bogachek, and U. Landman, Quantum electronic transport through three-dimensional microconstrictions with variable shapes, Physical Review B **53**, 4054 (1996).

[49] N. Reyren, S. Gariglio, A. D. Caviglia, D. Jaccard, T. Schneider, and J.-M. Triscone, Anisotropy of the superconducting transport properties of the $LaAlO_3/SrTiO_3$ interface, Applied Physics Letters **94**, 112506 (2009).

[50] G. Khalsa and A. H. MacDonald, Theory of the $SrTiO_3$ surface state two-dimensional electron gas, Physical Review B **86**, 125121 (2012).

[51] R. Danneau, O. Klochan, W. Clarke, L. Ho, A. Micolich, M. Simmons, A. Hamilton, M. Pepper, D. Ritchie, and U. Zülicke, Zeeman splitting in ballistic hole quantum wires, Physical Review Letters **97**, 026403 (2006).

[52] M. Briggeman, H. Lee, J.-W. Lee, K. Eom, F. Damanet, E. Mansfield, J. Li, M. Huang, A. J. Daley, C.-B. Eom, P. Irvin, and J. Levy, One-dimensional Kronig–Penney superlattices at the LaAlO 3/SrTiO 3 interface, Nature Physics , 1 (2021).

[53] I. Božović and J. Levy, Pre-formed Cooper pairs in copper oxides and $LaAlO_3$—$SrTiO_3$ heterostructures, Nature Physics **16**, 712 (2020).

[54] F. Nichele, S. Chesi, S. Hennel, A. Wittmann, C. Gerl, W. Wegscheider, D. Loss, T. Ihn, and K. Ensslin, Characterization of spin-orbit interactions of GaAs heavy holes using a quantum point contact, Physical Review Letters **113**, 046801 (2014).

[55] K. Kolasiński, A. Mreńca-Kolasińska, and B. Szafran, Transconductance and effective Landé factors for quantum point contacts: Spin-orbit coupling and interaction effects, Physical Review B **93**, 035304 (2016).

[56] C. Leighton, Electrolyte-based ionic control of functional oxides, Nature Materials **18**, 13 (2019).

[57] C. Liu, X. Yan, D. Jin, Y. Ma, H.-W. Hsiao, Y. Lin, T. M. Bretz-Sullivan, X. Zhou, J. Pearson, B. Fisher, J. S. Jiang, W. Han, J.-M. Zio, J. Wen, D. D. Fong, J. Sun, H. Zhou, and A. Bhattacharya, Two-dimensional superconductivity and anisotropic transport at $KTaO_3$ (111) interfaces, Science **371**, 716 (2021).

[58] Z. Chen, Y. Liu, H. Zhang, Z. Liu, H. Tian, Y. Sun, M. Zhang, Y. Zhou, J. Sun, and Y. Xie, Electric field control of superconductivity at the $LaAlO_3/KTaO_3$ (111) interface, Science **372**, 721 (2021).

[59] A. Caviglia, S. Gariglio, C. Cancellieri, B. Sacépé, A. Fete, N. Reyren, M. Gabay, A. F. Morpurgo, and J.-M. Triscone, Two-dimensional quantum oscillations of the conductance at $LaAlO_3/SrTiO_3$ interfaces, Physical Review Letters **105**, 236802 (2010).

[60] B. Jalan, S. Stemmer, S. Mack, and S. J. Allen, Two-dimensional electron gas in δ-doped $SrTiO_3$, Physical Review B **82**, 081103 (2010).

[61] A. Chikina, D. V. Christensen, V. Borisov, M.-A. Husanu, Y. Chen, X. Wang, T. Schmitt, M. Radovic, N. Nagaosa, A. S. Mishchenko, R. Valenti, N. Pryds, and V. N. Strocov, Band-Order Anomaly at the γ-$Al_2O_3/SrTiO_3$ Interface Drives the Electron-Mobility Boost, ACS nano **15**, 4347 (2021).

[62] A. Joshua, S. Pecker, J. Ruhman, E. Altman, and S. Ilani, A universal critical density underlying the physics of electrons at the $LaAlO_3/SrTiO_3$ interface, Nature Communications **3**, 1129 (2012).

[63] A. Jouan, S. Hurand, G. Singh, E. Lesne, A. Barthélémy, M. Bibes, C. Ulysse, G. Saiz, C. Feuillet-Palma, J. Lesueur, and N. Bergeal, Origin of the dome–shaped superconducting phase diagram in $SrTiO_3$–based interfaces, arXiv:2104.08220 (2021).

[64] M. B. Shalom, M. Sachs, D. Rakhmilevitch, A. Palevski, and Y. Dagan, Tuning spin-orbit coupling and superconductivity at the $SrTiO_3/LaAlO_3$ interface: a magnetotransport study, Physical Review Letters **104**, 126802 (2010).

[65] H. Noad, E. M. Spanton, K. C. Nowack, H. Inoue, M. Kim, T. A. Merz, C. Bell, Y. Hikita, R. Xu, W. Liu, A. Vailionis, H. Y. Hwang, and K. A. Moler, Variation in superconducting transition temperature due to tetragonal domains in two-dimensionally doped $SrTiO_3$, Physical Review B **94**, 174516 (2016).

[66] S. Hameed, D. Pelc, Z. Anderson, A. Klein, R. Spieker, L. Yue, B. Das, J. Ramberger, M. Lukas, Y. Liu, M. J. Krogstad, R. Osborn, C. Leighton, and M. Greven, Enhanced superconductivity and ferroelectric quantum criticality in plastically deformed strontium titanate, Nature Materials (2021).

[67] J. A. Bert, K. C. Nowack, B. Kalisky, H. Noad, J. R. Kirtley, C. Bell, H. K. Sato, M. Hosoda, Y. Hikita, H. Y. Hwang, and K. A. Moler, Gate-tuned superfluid density at the superconducting $LaAlO_3/SrTiO_3$ interface, Physical Review B **86**, 060503 (2012).

[68] C. Collignon, B. Fauqué, A. Cavanna, U. Gennser, D. Mailly, and K. Behnia, Superfluid density and carrier concentration across a superconducting dome: The case of strontium titanate, Physical Review B **96**, 224506 (2017).

Acknowledgments: This work benefited greatly from discussions with Praveen Sriram, Connie Hsueh, Molly Andersen, Joe Finney, Jimmy Williams, Jin Yue, Bharat Jalan, Jonathan Ruhman, Kam Moler, Jay Sau, and Elliott Mansfield.

Funding: Experimental work (fabrication and measurement) by E. M. was primarily supported the U.S. Department of Energy, Office of Science, Basic Energy Sciences, Materials Sciences and Engineering Division, under Contract DE-AC02-76SF00515, and by the Gordon and Betty Moore Foundation through Grant GBMF9460. Early experimental development by E.M. was supported by the Air Force Office of Scientific Research through grant no. FA9550-16-1-0126. E. M. was also supported by the Nano- and Quantum Science and Engineering Postdoctoral Fellowship at Stanford University and by internal Stanford University funds. Measurement contribution by I. T. R. was supported by the U.S. Department of Energy, Office of Science, Basic Energy Sciences, Materials Sciences and Engineering Division, under Contract DE-AC02-76SF00515, and by the ARCS foundation. Engagement by M. A. K and D. G.-G. was supported by the U.S. Department of Energy, Office of Science, Basic Energy Sciences, Materials Sciences and Engineering Division, under Contract DE-AC02-76SF00515. Measurement infrastructure was funded in part by the Gordon and Betty Moore Foundation's EPiQS Initiative through grant GBMF3429 and grant GBMF9460. Part of this work was performed at the Stanford Nano Shared Facilities (SNSF)/Stanford Nanofabrication Facility (SNF), supported by the National Science Foundation under award ECCS-1542152. Work at the University of Strathclyde was supported by the EPSRC Programme Grant DesOEQ (EP/P009565/1).

Author contributions: E.M. and D.G.-G. designed the experiment. E.M. fabricated the devices. E.M. and I.T.R. performed the measurements. E.M. carried out data analysis. J.K. and F.D. performed theoretical simulations. All authors discussed the results and wrote the manuscript.

Competing interests: The authors declare that they have no competing interests.

Data availability: The data that support the findings of this study are available at https://doi.org/10.5281/zenodo.5590921

Methods

Device Fabrication.

Fabrication is based on commercial (001)-oriented $SrTiO_3$ single crystal substrates, purchased from MTI. To obtain a Ti-terminated surface with terrace step morphology, these substrates were soaked in heated deionized water for 20 minutes and annealed at 1000 °C for 2 hours in flowing Ar and O_2 in a tube furnace.

The HfO_x barrier layer was deposited by atomic layer deposition (ALD), with only 4 alternated cycles of Hf precursor and water. Extrapolating from measured thickness of many-cycle growths, we estimate this barrier at 0.6 nm. The deposition stage temperature was 85 °C.

Subsequent fabrication follows the method described in [26]. All patterning was performed with lift-off processes using e-beam patterned PMMA 950K, 4% in anisole for the first step, 8% for all subsequent steps. The first step is the local split-gate pattern, written on a 100 kV e-beam lithography system. ALD was then used to deposit 15 nm HfO_x (100 cycles) at 85 °C. The 5 nm Ti / 50 nm Au gate contact was deposited by e-beam evaporation. Lift-off of both HfO_x and Ti/Au layers was performed by soaking in heated NMP, followed by ultrasonication in acetone. Imaging by scanning electron microscopy was performed on reference structures on the same chip as the measured device. The remaining patterning was performed with a 50 kV e-beam lithography system. The second step is the contact line to the split gate, using lift-off of 40 nm Ti / 100 nm Au in acetone. The third step is the ohmic contact deposition, which requires exposing the pattern to Ar^+ ion milling prior to e-beam evaporation of 10 nm Ti / 80 nm Au, followed by lift-off in acetone. The fourth patterning step is the mesa insulation, deposited by magnetron sputtering 80 nm SiO_2, followed by lift-off in acetone.

The finished device was annealed for 50 minutes at 130 °C in air. Immediately after depositing a drop of ionic liquid Diethylmethyl(2-methoxyethyl)ammonium bis(trifluoromethylsulfonyl)imide (DEME-TFSI) to cover both the device and the surrounding side gate, the sample was loaded into the dilution refrigerator system, then vacuum pumped overnight to minimize contamination of the ionic liquid by water from exposure to air.

Unless explicitly stated otherwise, all presented measurements are in a 4-probe configuration shown in Fig.1d: nominal DC and AC voltage excitations (V^*_{DC} and $V^*_{\mathrm{AC}} = 10$ or 20 μV) are sourced through the constriction. I_{DC} and I_{AC} are the measured DC and AC currents through the drain. Voltage probes are used to measure the DC and AC voltage difference across the constriction (V_{DC} and V_{QPC}, respectively) and the AC longitudinal (V_{xx}) and Hall (V_{H}) voltages outside the constriction. The constriction conductance is given by $G = I_{\mathrm{AC}}/V_{\mathrm{QPC}}$, the 2DEG resistance by $R_{xx} = V_{xx}/I_{\mathrm{AC}}$, and the Hall density by $N_{\mathrm{H}} = I_{\mathrm{AC}}B/eV_{\mathrm{H}}$. No series resistance subtraction was made for G. Split gate voltage V_{G12} was applied on both arms of the QPC. In the supplementary material, data with unequal voltages on the two arms (V_{G1} and V_{G2}) are also shown.

Supplementary material to this report presents extensive additional data and background. Section S1 discusses the tuning of the Hall bar channel by V_{GIL} near room temperature, the equivalence between back-gating and adjusting V_{GIL} at cryogenic temperatures, absence of globally coherent superconductivity, and Shubnikov-De Haas oscillations. Section S2 presents split gate lever arm analysis, the 3D confined constriction Hamiltonian, and the extended analysis of QPC subbands in B. Section S3 presents extensive data on stability of conductance quantization with respect to V_{GIL}, and asymmetrically swept split gate voltages. Section S4 presents images of devices during the fabrication process, and transport data from additional devices.

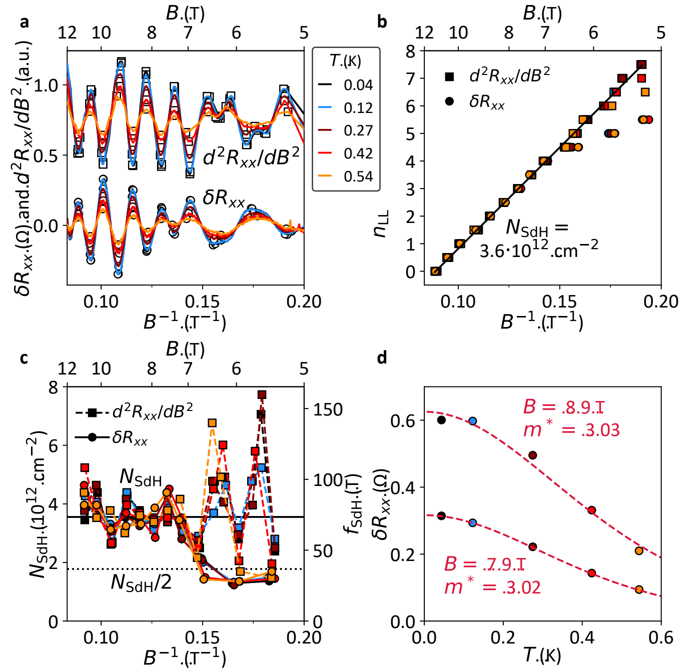

Extended Data Fig. 1. Quantum oscillations in the 2DEG. (a) Temperature dependence of Shubnikov-de Haas oscillations. Same data are shown as background-subtracted resistance and its second derivative with B. Markers indicate indexed maxima and minima. (b) Landau level index n_{LL} plotted against peak positions in $1/B$. (c) Spacing between individual oscillations, converted to local frequency and implied carrier density. Solid line in (b,c) is a constant-frequency fit for $B > 7$ T. Dotted line in (c) is half of fitted value. (d) Temperature dependence of oscillation amplitude at $B = 7.9$ and 8.9 T, dashed lines are fits to Lifshitz-Kosevich model with $m^* = 3$.

Quantum oscillations

Extended Data Fig. 1a shows background-subtracted magnetoresistance δR_{xx} of an unpatterned 2DEG section directly adjacent to the constriction. Its second derivative $d^2\delta R_{xx}/dB^2$ is also shown.

Shubnikov-de Haas (SdH) type oscillatory behavior is clearly present when the data are plotted against $1/B$. But its periodicity is uneven, leading to failure of standard analysis with fast Fourier transforms. Instead, we adopt the "Landau plot" procedure by indexing the minimum and maximum locations of individual oscillations (Extended Data Fig. 1b). From the linear-slope region at $B > 7$T, we extract an oscillation frequency $f_{\mathrm{SdH}} = 74$ T. The corresponding carrier density $N_{\mathrm{SdH}} = f_{\mathrm{SdH}}\nu_s e/h$ for spin degeneracy $\nu_s = 1$ is 3.6×10^{12} cm^{-2}. The spacing between oscillation peaks is also converted into local, B-dependent f_{SdH} and N_{SdH} in Extended Data Fig. 1c. The factor of ≈ 10 discrepancy between N_{SdH} and the Hall density (4.6×10^{13} cm^{-2}) is a ubiquitous and poorly-understood feature of quantum oscillations in $SrTiO_3$ (see e.g. [15, 59, 60])

The temperature dependence of the oscillation amplitude encodes information on the effective electron mass. Extended Data Fig. 1d shows a fit of peak-to-peak amplitude to the thermal suppression factor in the Lifschitz-Kosevich model (see e.g. [15]): $\delta R_{xx} \sim \alpha T/\sinh(\alpha T)$, with $\alpha = 2\pi^2 k_B/\hbar\omega_c$ and the cyclotron frequency $\hbar\omega_c = eB/m_e^*$. Reflecting the sharp reduction of oscillation amplitude by a factor of ≈ 3 between 40 mK and 600 mK, this analysis gives $m_e^* = 3m_e$, higher than $m^* =$ 1-2m_e reported in most experiments on quantum oscillations in $SrTiO_3$ [13, 15, 44, 59, 60]. In most $SrTiO_3/LaAlO_3$ 2DEGs, the light-in-plane-mass $m^* =$ 1-2m_e d_{xy} band is lowest-lying, followed by the heavier d_{yz} band. However, an inversion of this band order has recently been reported in high mobility $SrTiO_3/\gamma\text{-}Al_2O_3$ 2DEGs [61], and a similar effect may be occurring in our 2DEG. In contrast, the field evolution of quantum subbands in our constriction gives $m^* =$ 0.8-1.1, suggesting that the confinement potential favors the lighter d_{xy} or d_{zx} as the lowest band.

Below 7 T, oscillation frequency in δR_{xx} is approximately halved, consistent with a spin-degenerate state ($\nu_s = 2$). Analysis using $d^2\delta R_{xx}/dB^2$ at low temperature can resolve faint high-frequency peaks even at lower fields. Though one expects the spin degeneracy to be broken at any nonzero B, *apparent* spin degeneracy can persist in large B if the Zeeman and cyclotron energy scales are comparable, leading to overlap between adjacent spin-polarized Landau levels. This situation has been reported for other $SrTiO_3$-based 2DEGs [13, 44, 60]. As discussed further in supplementary section S1C, this is likely applicable in our case. Therein we also consider an alternative explanation that pairing occurs in the 2D bulk, not just in the constriction. This is motivated by the rough match between two field scales: the field at which bulk SdH oscillation frequency doubles, and B_{P} at which two-fold degeneracy in the constriction subbands is broken. Without conclusively discriminating between these two possibilities, we conclude that the conventional explanation based on overlap between broadened Landau levels is more likely.

Absence of long range superconducting order. A surprising aspect of this experiment is the absence of superconductivity in all 4-terminal measurements of both the 2DEG and the constriction. Current-voltage non-linearity is only seen in 2-terminal measurements, indicating that superconductivity is only present in a region near the ohmic contacts (fabricated by ion milling into $SrTiO_3$ to locally induce a high density of oxygen vacancies and thus a high local carrier density).

Extended Data Fig. 2 illustrates that the explored Hall carrier densities correspond to the near-optimal and over-doped regions of the superconducting dome in similar devices without the HfO_x barrier (and much lower mobility [26]) and $SrTiO_3/LaAlO_3$ [62–64], in which T_c peaks at 350 mK near 2-3$\times10^{13}$ cm^{-2}. In high-mobility ionic liquid gated $SrTiO_3$ with hBN barrier layers, a narrower superconducting dome appears with reduced $T_c = 200$ mK and at higher density of 6-8$\times10^{13}$ cm^{-2}. These comparisons point to an overall trend of suppression of a globally coherent superconducting order parameter in clean $SrTiO_3$ 2DEGs.

More investigations are needed to elucidate the microscopic underpinnings of this trend, but at this stage we can outline several likely relevant factors. (1) The pairing mechanism is defect-mediated. Several recent studies suggest that extended defects such as tetragonal domain walls and dislocations favor superconductivity in $SrTiO_3$ [65, 66]. In our case, however, the disorder reduction is likely driven by reduced scattering from charge disorder near the surface. It is not clear that structural defects should be suppressed by adding a thin HfO_x layer. (2) Rearrangement of electronic structure and/or t_{2g} band order due to the lowest-lying band changing from d_{xy} (in $SrTiO_3$/IL and $SrTiO_3/LaAlO_3$) to $d_{xz,yz}$ (in $SrTiO_3/HfO_x$+IL), as suggested by the increased in-plane cyclotron mass in our 2DEG. (3) Crossover from dirty to clean limit BCS. Superconducting 2DEGs in $SrTiO_3$ are usually in the dirty limit: $\pi\Delta\tau/\hbar \ll 1$ (τ is the scattering rate and Δ the superconducting gap), and superfluid density N_S is correspondingly a fraction of the total carrier density N [67]. In uniformly doped $SrTiO_3$, a crossover to the clean limit ($\pi\Delta\tau/\hbar \gtrapprox 1$, $N_S \approx N$) has been observed at low N [68]. The decreased disorder in our case would put the system into the clean limit if the superconducting T_c remained near typical values 0.1-0.4 K. A possible interpretation is thus that superconducting order is unstable in the 2D clean limit. Moreover, comparison between this work and Refs. [14, 26, 64] suggests an overall trend of decreasing critical field B_c at low disorder (see supplementary section S1B). The corresponding increase of superconducting coherence length and its interplay with lateral 2DEG inhomogeneity are likely important pieces of the puzzle.

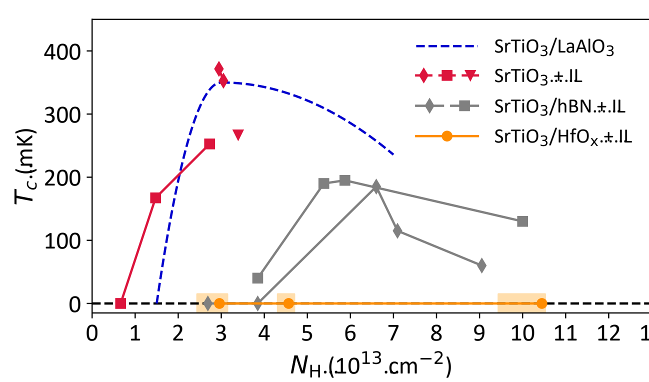

Extended Data Fig. 2. Absence of long range superconducting order. Connected symbols show superconducting T_c for the same device with Hall density tuned by ionic liquid gate voltage. Lateral shading for $SrTiO_3/HfO_x$+IL data represents the N_{H} region explored by V_{GIL} modulation with frozen ionic liquid. $SrTiO_3$+IL data are from [26], $SrTiO_3$/hBN+IL data are from [14], Typical location of the superconducting dome in $SrTiO_3/LaAlO_3$ is drawn consistent with [62, 63].

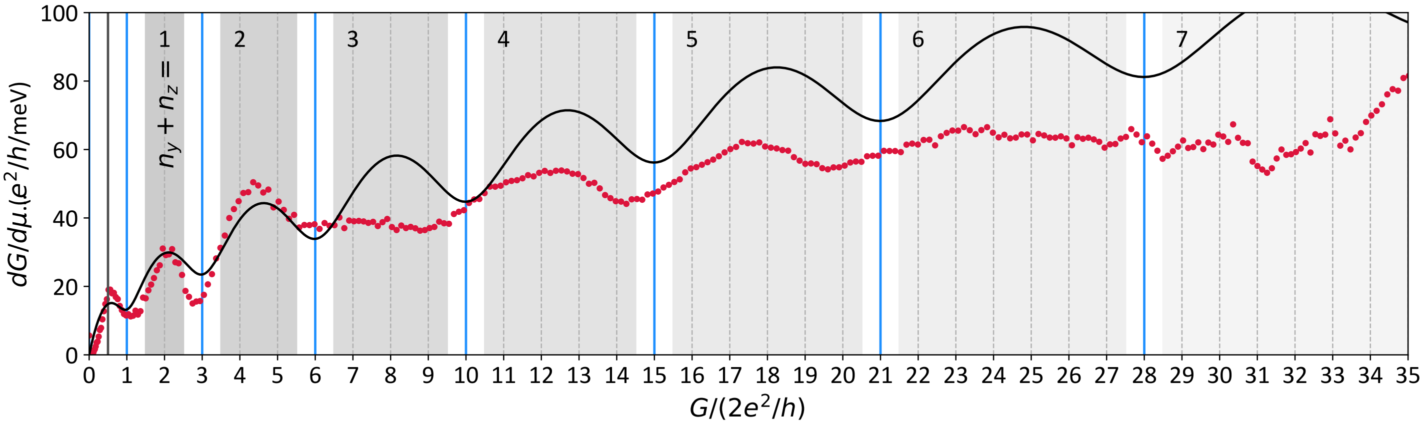

Extended Data Fig. 3. Subband packets and Pascal sequence. Parametric plot of transconductance against conductance at $B = 0$. Markers are a line cut from data shown in Fig. 3c at zero field. The dips in transconductance follow the Pascal sequence $G/(2e^2/h) = 0, 1, 3, 6, 10, 15, 21, \ldots$ (blue vertical lines). Shaded regions indicate the extent of subband packets with same $n_y + n_z$ that are quasi-degenerate, within broadening. Black line is the model of transconductance generated by Eq. (2) with broadening by $\hbar\omega_x = 0.11$ meV, see supplementary sections S2B,C for details.

Supplementary material for "Clean ballistic quantum point contact in $SrTiO_3$"

CONTENTS

S1. UNPATTERNED 2DEG TRANSPORT

A. Gate tuning of the Hall bar channel

In this section, the details of global carrier density tuning in the Hall bar channel are presented. The control knob used for this purpose in this work is the ionic liquid gate voltage $V_{\rm GIL}$. We note a departure from the procedure in our previous work [S1], in which $V_{\rm GIL}$ was set near room temperature, remained unchanged throughout the cooldown, and the back gate voltage applied to the bottom of the $SrTiO_3$ was used to modulate the vertical extent of the 2DEG. In this work, $V_{\rm GIL}$ was used for both of these purposes and no back gate contact was made. In our testing of the main QPC device and control Hall bar devices, we found that at low temperatures, the functionality of adjusting $V_{\rm GIL}$ is very similar to the one of a back gate voltage. The low temperature is required to freeze the ionic liquid (below 220 K) and to maximize the dielectric constant of $SrTiO_3$ (which increases up to $\approx 10^4$ in the few Kelvin range [S2]). Consequently, there are two relevant values of $V_{\rm GIL}$ for each device state: the voltage used above 220 K to coarsely set the global 2DEG carrier density, and the voltage used near base temperature for finer modulation of the 2DEG. Throughout the manuscript, cited values of $V_{\rm GIL}$ refer to its low temperature state.

For the near room temperature values of $V_{\rm GIL}$, the Hall density measured at base temperature is used as a proxy. $V_{\rm GIL}$ was first set to 3.5 V at room temperature prior to the first cooldown of the main device, yielding a Hall density $N_{\rm H} = 10.4 \times 10^{13}$ cm^{-2} at base temperature. For the second and third cooldowns, $V_{\rm GIL}$ was set to 1 and 3.9 V at 280 K, yielding $N_{\rm H} = 3.0$ and 4.6 $\times 10^{13}$ cm^{-2}, respectively.

In comparison to our previous work on ionic liquid-gated $SrTiO_3$ devices without HfO_x barriers [S1], there was a notable difference in the time scale required for device state stabilization after adjusting $V_{\rm GIL}$ near room temperature. For devices described in [S1], this time scale was on the order of tens of seconds to several minutes (depending on temperature). In this work, stabilization on the scale of tens of minutes was necessary even for small adjustments on the order of 0.1 V. This explains why large $V_{\rm GIL}$ swings described above were needed to obtain desired carrier densities. Qualitatively, these observations are consistent with presence of a dielectric capacitor (HfO_x barrier layer) between the polarized ionic liquid molecules and the channel, resulting in slower charging of the system under voltage difference.

Fig. S1 shows the effect of $V_{\rm GIL}$ at base temperature on the 4-probe measurements of 2DEG Hall density $N_{\rm H}$, its sheet resistance $R_{\rm xx}$, and Hall mobility $\mu_{\rm H} = (eN_{\rm H}R_{\rm xx})^{-1}$. Measurements from 20×20 μm squares on both sides of the constriction are shown. The constriction in the middle is tuned into an open (many-channel) state by setting $V_{\rm G12}$=0.8 V. Small non-linearity of the Hall effect in B (less than 15% between 0 and 14 T for all cooldowns) was neglected. For all cooldowns, tuning by $V_{\rm GIL}$ with frozen ionic liquid is marginal. Its direction is consistent with the back-gating mechanism described in [S1, S3]: higher back gate voltage or $V_{\rm GIL}$ increases the vertical extent of the 2DEG, moving it away from surface disorder and thus increasing $\mu_{\rm H}$. This effect is overlayed with a similarly marginal capacitive modulation of $N_{\rm H}$. Similarly to back gating in [S1], the available range of $V_{\rm GIL}$ at low temperature is restricted by: 1) degradation of ohmic contacts at $V_{\rm GIL}$ below a certain threshold, 2) hysteretic saturation of the modulation at high $V_{\rm GIL}$, similarly to [S1, S4].

Modulation by $V_{\rm GIL}$ has a more pronounced effect on the adjacent constriction. In particular, it allowed us to tune the constriction pinch-off point (see section S3), and avoid the regime of negative split gate voltage $V_{\rm G12}$ where ohnic

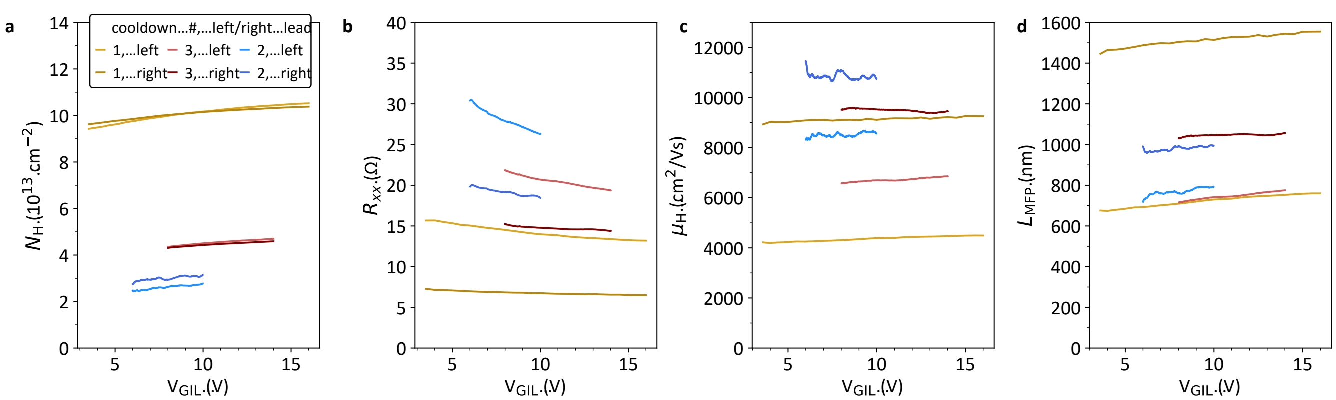

Fig. S1. 2DEG tuning by $V_{\rm GIL}$ with frozen ionic liquid. (a) Hall density at $B = 14$ T for cooldowns 1 and 3, 5T for cooldown 2. (b) 2DEG sheet resistance at $B = 0.2$, 0, 0.5 T for cooldowns 1, 2, 3 respectively. (c) Hall mobility. (d) Mean free path.

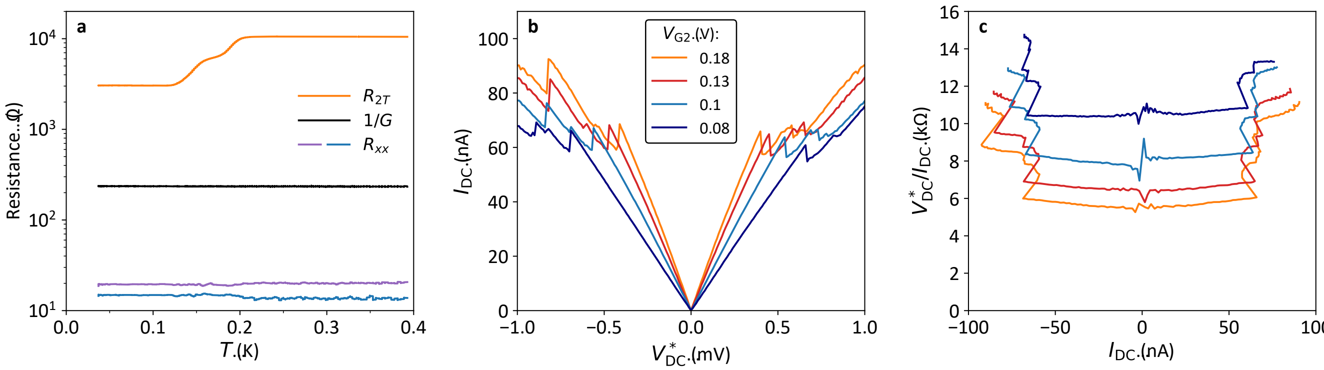

Fig. S2. Non linearity in two-terminal measurements. (a) Temperature dependence of the AC two-terminal resistance $R_{2\mathrm{T}}$, and 4 terminal measurements of the constriction and 2DEG resistances. Data from the 4.6×10^{13} cm^{-2} cooldown. (b) Drained DC current - nominal DC voltage curve at base T, and different split gate voltages. (c) Corresponding 2-terminal DC resistance, showing jumps at same DC current. Data in (b,c) are from the 3.0×10^{13} cm^{-2} cooldown, same measurement is also shown in Fig. S7d.

contacts are also prone to damage. V_{GIL} values used for detailed characterization of the constriction were 7 and 10 V for the 3.0 $\times 10^{13}$ cm^{-2} cooldown and 12 V for the 4.6 $\times 10^{13}$ cm^{-2} cooldown. The N_{H} values used throughout the manuscript to identify the 3.0, 4.6, and 10.4 $\times 10^{13}$ cm^{-2} cooldowns are for $V_{\mathrm{GIL}} = 10$, 12, and 16 V, respectively, averaged between the 2DEG sections on the left and right of the constriction.

B. Absence of superconductivity

A noteworthy surprise discussed in the main text is the absence of superconductivity in 4-terminal measurements of the 2DEG resistance. Fig. S2a illustrates that the temperature dependence of R_{xx} is flat down to the base temperature (37 mK here). The same is true for the resistance of the constriction (R_{QPC}) tuned into an open state by V_{G12}. However, a strong superconductor-like down turn is clearly seen between 130 and 200 mK in the two-terminal resistance $R_{2\mathrm{T}} = V_{\mathrm{AC}}/I_{\mathrm{d}}$, where V_{AC} is the nominal source voltage excitation and I_{d} is the measured drain current. Since the measurement configuration involves sourcing a voltage across the constriction, $R_{2\mathrm{T}}$ is approximately a series sum of $2R_{\mathrm{xx}}$, $1/G$ (constriction resistance), 2DEG-to-metal ohmic contact resistances, two sets of metallic lines on the device and dilution refrigerator lines, including cryogenic filtering setups (with 2-3 kΩ DC resistance per line). Of these contributions, the most likely candidate for the location of the observed drop in $R_{2\mathrm{T}}$ is the 2DEG-to-metal ohmic contact, which was fabricated by patterned ion milling of $SrTiO_3$, followed by Ti/Au metal deposition. The ion milling procedure is typically understood to dope $SrTiO_3$ with oxygen vacancies, creating robustly metallic 2DEGs [S7]. Consequently, our device likely has a narrow superconducting region below and/or near the ohmic contacts.

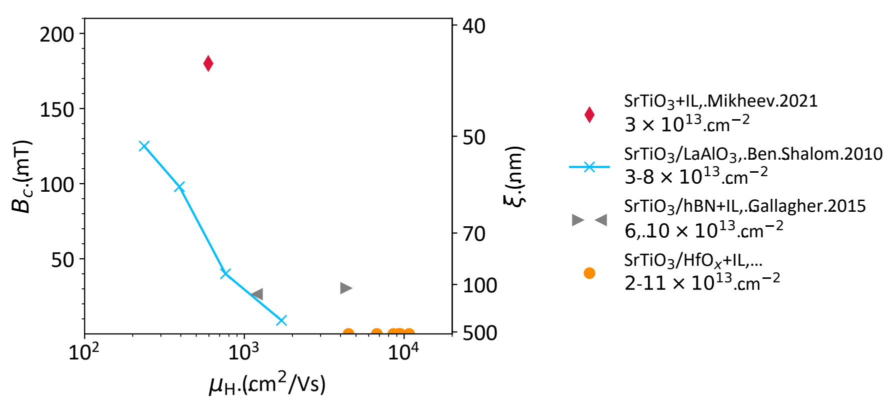

Fig. S3. Superconducting critical field and inferred coherence length as a function of Hall mobility. Comparison with [S1, S5, S6].

This explanation is consistent with the observation of a drop in $R_{2\mathrm{T}}$ driven by temperature, small magnetic field (at ≈ 50 mT), and DC source current (shown in Fig. S2b and S2c).

Extended Data Fig. 2 in the main text compares the range of carrier density studied in our $SrTiO_3$/HfO_x+IL device (IL stands for ionic liquid gate) to closely related superconducting 2DEGs: $SrTiO_3$+IL devices with very similar design but lower mobility [S1] and $SrTiO_3$/hBN+IL Hall bar devices with comparably high mobility [S6], and $SrTiO_3$/$LaAlO_3$ 2DEGs [S8, S9]. The overall trend is suppression of peak T_c value and its movement to higher N_H for $SrTiO_3$ 2DEGs with high mobility. A potentially related trend is the suppression of the superconducting critical field B_c and the corresponding increase of the inferred superconducting coherence length $\xi = (\Phi_0/2\pi B_c)^{1/2}$ at low disorder. This is based on comparison with [S1, S5, S6] in Fig. S3, where B_c and corresponding ξ are shown as a function of Hall mobility. For the device in this work, $B_c = 0$. This is not an ideal cut in the $B_c - \mu_\mathrm{H}$ space, as carrier densities and sources of disorder are different across these works, but rather a coarse illustration of a big picture trend.

C. Shubnikov-De Haas oscillations

This section presents supplementary data on quantum oscillations in the 2DEG resistance, and describes in detail their analysis. The measurement configuration was similar to all other measurements described in this work, but the constriction was tuned into an open state by V_{G12}, and a large AC source current (500 nA) was sourced through the constriction to improve the signal-to-noise ratio in the 4-probe measurement of 2DEG resistance R_{xx}. For all three cooldowns of the main device, strong oscillatory features were present in the longitudinal magnetoresistance of the 2DEG. For the 4.6×10^{13} cm^{-2} cooldown, a detailed analysis of the temperature dependence of such oscillations is shown in Extended Data Fig. 1 in the main text and Fig. S6. Fig. S4 shows base temperature (≈ 40 mK) traces for all three cooldowns, measured on both sides of the constriction.

As demonstrated below, oscillation periodicity was typically not regular in $1/B$. This caused the Fourier analysis to be overly sensitive to the choice of data range, and thus not reliable in our case. As an alternative, we algorithmically identified the minima and maxima of individual oscillations, indicated by red and orange markers in Fig. S4. For corroboration, we carried out this analysis on δR_{xx} (4-terminal resistance of the 2DEG after subtraction of a smooth background), and on its second derivative d^2R_{xx}/dB^2 (without any background subtraction).

The spacing between oscillations extrema is shown in Fig. S4 as a B-dependent frequency f_{SdH}. Within the picture of Shubnikov-de Haas oscillations, the corresponding carrier density is $N_{\mathrm{SdH}} = 2eh^{-1}f_{\mathrm{SdH}}\nu^{-1}$, where is ν is the degeneracy number. The conversion between the N_{SdH} and f_{SdH} axes in Fig. S4 is shown assuming $\nu = 1$ (spin-resolved Landau levels). An alternative representation is the "Landau plot" shown in Fig. S4: oscillation extrema are indexed as integer Landau Level number n_{LL}, and plotted with respect to their position in $1/B$. A straight line with a slope given by f_{SdH} is expected for conventional Shubnikov-de Haas oscillations.

A recurring pattern in Fig. S4 is the abrupt increase in oscillation periodicity as B is increased past a certain value B_X of order 4-8 T. As summarized in Fig. S5, f_{SdH} was typically 60-100 T at high $B > B_\mathrm{X}$, which corresponds to N_{SdH} of 3-5$\times10^{12}$ cm^{-2}. At low $B < B_\mathrm{X}$, f_{SdH} is lowered by a factor of 2-3.

In Fig. S4, the Landau plots were fitted to B_X, f_{SdH} above B_X, and a numerical multiplicative factor F_X for f_{SdH} below B_X. B_X is 5.5-7.5 T from analysis of δR_{xx} and 4-6 T from analysis of its second derivative. This discrepancy is expected since the latter procedure captures more of the vanishing high frequency extrema near B_X. Due to the difficulty of accurately resolving all peaks near and below B_X, both B_X and F_X are not reliably measured quantities. Least squares fitting gives $F_\mathrm{X} = 1.5$-3, but it is likely to be overestimated due to unresolved oscillation peaks.

A natural explanation for this increase in f_{SfH} is breaking of the spin degeneracy, bringing ν from 2 to 1 above B_X. This would be consistent with $F_\mathrm{X} = 2$. A conventional explanation for the persistence of this two-fold degeneracy up to a fairly large B_X involves a situation where cyclotron and Zeeman energy scales (or their integer multiples) are approximately equal ($\hbar\omega_c \approx g\mu_B B$). If their difference is less than Landau level broadening, than the adjacent spin up and down Landau levels will end up overlapping in finite B. This will result in apparent spin degeneracy, persistent up to a field where $\hbar\omega_c - g\mu_B B$ becomes larger than the broadening. This situation has been observed in $SrTiO_3$-based 2DEGs [S10, S11]. The condition $\hbar\omega_c \approx E_Z$ is likely to be satisfied in our case as well. Taking $m^* = 3$ (value extracted below from T dependence of oscillation amplitude), $\hbar\omega_c = E_Z$ if $g = 0.67$. This is approximately double of the value extracted from analysis of QPC subbands (see section S2 C), and very close to the value reported in [S12].

A compelling alternative explanation involves comparing the B_X scale from quantum oscillations in the 2DEG with the B_P scale observed in the Y subband shape observed in transport across the adjacent gated constriction (see section S2 C). Both B_X and B_P are indicative of a two-fold degeneracy (presumably from spin) that persists in finite field. $B_\mathrm{X} = 4$-8 T is approximately coincident with $B_\mathrm{P} = 5$-6 T observed for the lowest lying subbands of the constriction. It is therefore natural to speculate whether the physics behind non-zero B_X and B_P could be the same. A likely mechanism for the Y shape in QPC subbands is from an attractive pairing interaction between electrons, as

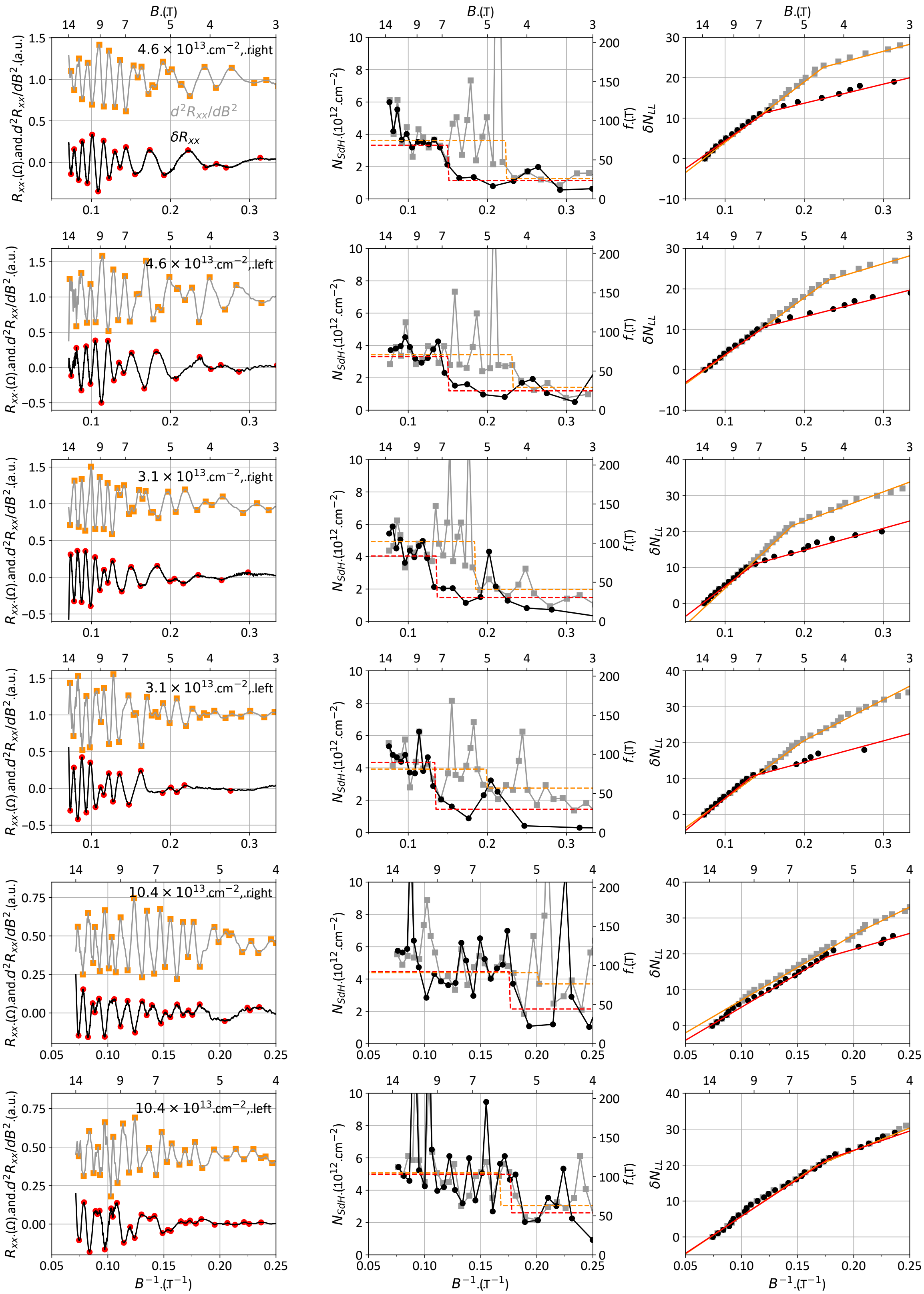

Fig. S4. Supplementary quantum oscillation data. Left column: background subtracted magnetoresistance (black) and its second derivative with B (grey), markers are indexed oscillation peaks. Middle column: Peak-to-peak spacing, converted into local frequency and carrier density. Right column: Landau plot of Landau level index against $1/B$. Lines in middle and right columns are fits to separate oscillation frequencies above and below B_{X}. For each row, Hall carrier density and R_{xx} measurement on right or left side of the constriction are labeled in the leftmost plot.

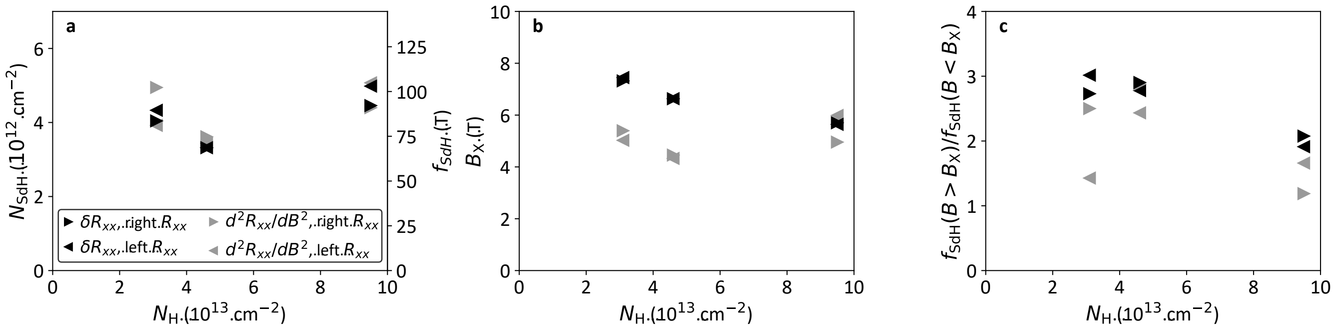

Fig. S5. Summary of quantum oscillation frequencies. From data in Fig. S4: (a) $f_{\rm SdH}$ above $B_{\rm X}$ is shown against Hall density. (b) Crossover point to lower $f_{\rm SdH}$ below $B_{\rm X}$. (c) Ratio of $f_{\rm SdH}$ above and below $B_{\rm X}$. Data in (b) and (c) are particularly prone to analysis error in peak identification (see text).

discussed in the main text and [S13]. If this interaction is intrinsic to the 2DEG, regardless of quantum confinement in the constriction, it could result in a genuine (as opposed to apparent for the conventional explanation) spin degeneracy that is persistent in large B. Within the present study, we cannot conclusively discriminate between the conventional and alternative explanation for persistent two-fold degeneracy in the 2DEG. The progressive nature of periodicity doubling indicated by the different transition field scales extracted from analysis of δR_{xx} and d^2R_{xx}/dB^2 appears more consistent with the conventional explanation.

Conversely, it is important to note that the conventional mechanism ($\hbar\omega_c \approx E_Z$) cannot explain persistent two-fold degeneracy in the constriction: its subbands are further split by quantum confinement in lateral and vertical directions, preventing the possibility of overlap between adjacent Zeeman-split subbands. Therefore, if the conventional explanation is valid for oscillations in the unpatterned 2DEG, the coincidence with $B_{\rm P}$ in the constriction is most likely accidental.

The oscillation amplitude ΔR_{xx} is typically analysed in the framework of the Lifshitz–Kosevich formula, which describes its suppression with B and T:

$$\begin{aligned} \delta R_{xx}(B,T) &= 4R_0 A_T A_B, \\ A_T &= \frac{\alpha T}{\sinh(\alpha T)}, \\ A_B &= \exp(-\alpha T_{\rm D}), \\ \alpha &= 2\pi^2 k_B/\hbar\omega_c, \end{aligned} \tag{S1}$$

Where $\omega_c = eB/m_e^*$ is the cyclotron frequency, R_0 is a constant amplitude factor, $T_{\rm D}$ is the Dingle temperature.

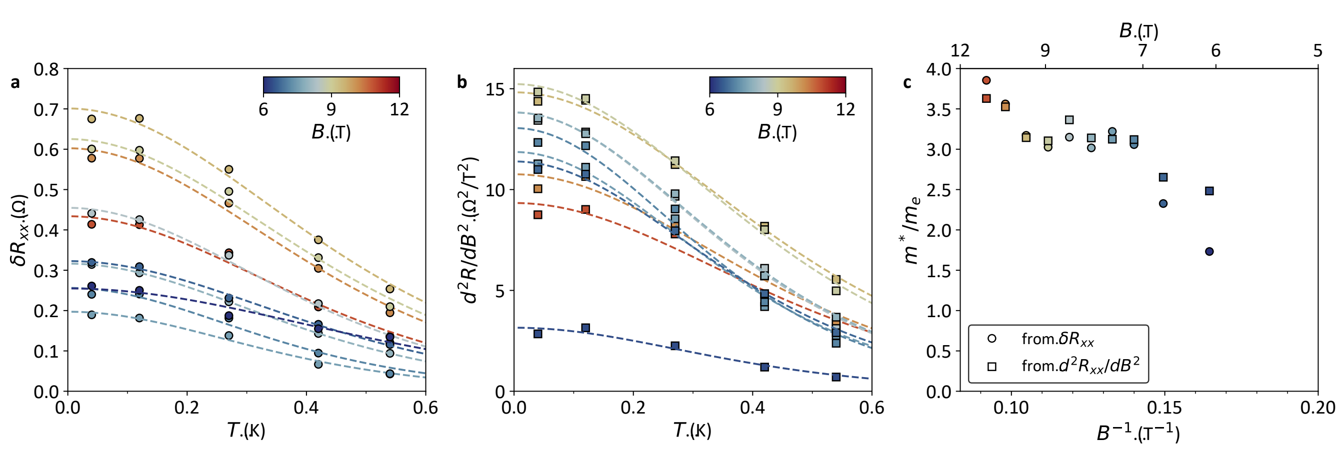

Fig. S6. Effective mass extraction. Full data for Extended Data Fig. 2d in the main text. Temperature dependence of oscillations in (a) δR_{xx}, (b) d^2R_{xx}/dB^2. Dashed lines are fits to A_T in equation S1, giving the effective elecetron mass shown in (c).

Figures S6a and S6b show the temperature dependence of peak-to-peak amplitude of oscillations in both δR_{xx} and d^2R_{xx}/dB^2. Both were fitted to the thermal suppression factor A_T, giving the effective mass m^* shown in Fig. S4c. For peaks in the B = 7-9.5 T range, m^* = 3 - 3.2 from both procedures. At low B close to B_{X} (<7 T), peak-to-peak amplitude is affected by the transition to larger oscillation periodicity. At high B (>9.5 T), a faint low frequency oscillation (difficult to distinguish from smooth background) interfered with the extraction of the dominant oscillation amplitude. Presence of multiple oscillation components has been documented in other $SrTiO_3$-based 2DEGs [S6, S10, S14–S16].

Analysis of the magnetic suppression factor A_B was not reliable due to the narrow range in B where oscillations were not subject to such beating patterns. Within the available B range, it was not possible to accurately disentangle secondary oscillation contributions for our case. Estimates in the intermediate range B = 8-10 T gave T_{D} = 0.6-1.7 K (from δR_{xx}) and 0.2-0.6K (from d^2R_{xx}/dB^2). With m^* = 3.1, the estimate range for the corresponding quantum mobility $\mu_Q = \hbar/(2\pi m_e^* k_B T_{\mathrm{D}})$ is 400-3500 cm^2/Vs.

S2. QPC TRANSPORT

A. DC bias spectroscopy and lever arm analysis

In this section, supplementary DC bias spectroscopy data are presented. The transconductance diamond pattern in such measurements is evidence of ballistic transport across the constriction. It also allows for extraction of a "lever arm" coefficient f_{LA} for conversion of split gate voltage into chemical potential.

Fig. S7a illustrates the physical mechanism behind DC bias spectroscopy. At $V_{\mathrm{DC}} = 0$, the conductance of the QPC (G) is determined by the number of discrete subbands below the chemical potential (μ), which is locally controlled by one or two split gates (V_{G12} or V_{G2}, interchangeably referred to as V_{G} below). Each subband contributes a quantum of $\nu_s e^2/h$ to G, with $\nu_s = 1$ or 2 being the spin degeneracy. Gradually increasing μ with V_{G} creates a step structure in G. Equivalently, peaks in $dG/d\mu$ (or dG/dV_{G}) occur at subband energies. A non-zero V_{DC} creates a difference between the chemical potential in the left and right lead (μ_{L} and μ_{R}). Therefore, the number of filled subbands needs to be counted separately for the left and right moving electrons. Each subband now contributes a quantum of $\nu_s e^2/2h$, allowing for fractional filling with μ_{L} or μ_{R}) only. In the example in Fig. S7a, applying V_{DC} changes G from $4e^2/h$ to $5e^2/h$ (if $\nu_s = 2$).

For a two-dimensional measurement of G with V_{G} and V_{DC}, this mechanism creates a diamond pattern with alternating rows of "integer" plateaus at $G = n\nu_s e^2/h$ ($n = 0, 1, 2, ...$), and "half-integer" plateaus at $G = (n + 0.5) \cdot \nu_s e^2/h$. Such patterns are observed in our device in the cooldowns with global Hall density at 3.0 and 4.6×10^{13} cm^{-2}. At $B = 5$ T, $\nu_s = 2$ (Fig. S7b,e). At $B = 14$ T, $\nu_s = 1$ (Fig. S7c,d). Deviations from the pattern are present in the form of overlapping subbands, either from Zeeman splitting at high B (Fig. S7c) or from overlap between subbands generated by lateral and vertical confinement (see sections S2 B, S2 C). At $B = 0$ T, the diamond pattern from ballistic subbands is clearly observable (Fig. S7d). But the quantization pattern in G deviates strongly from

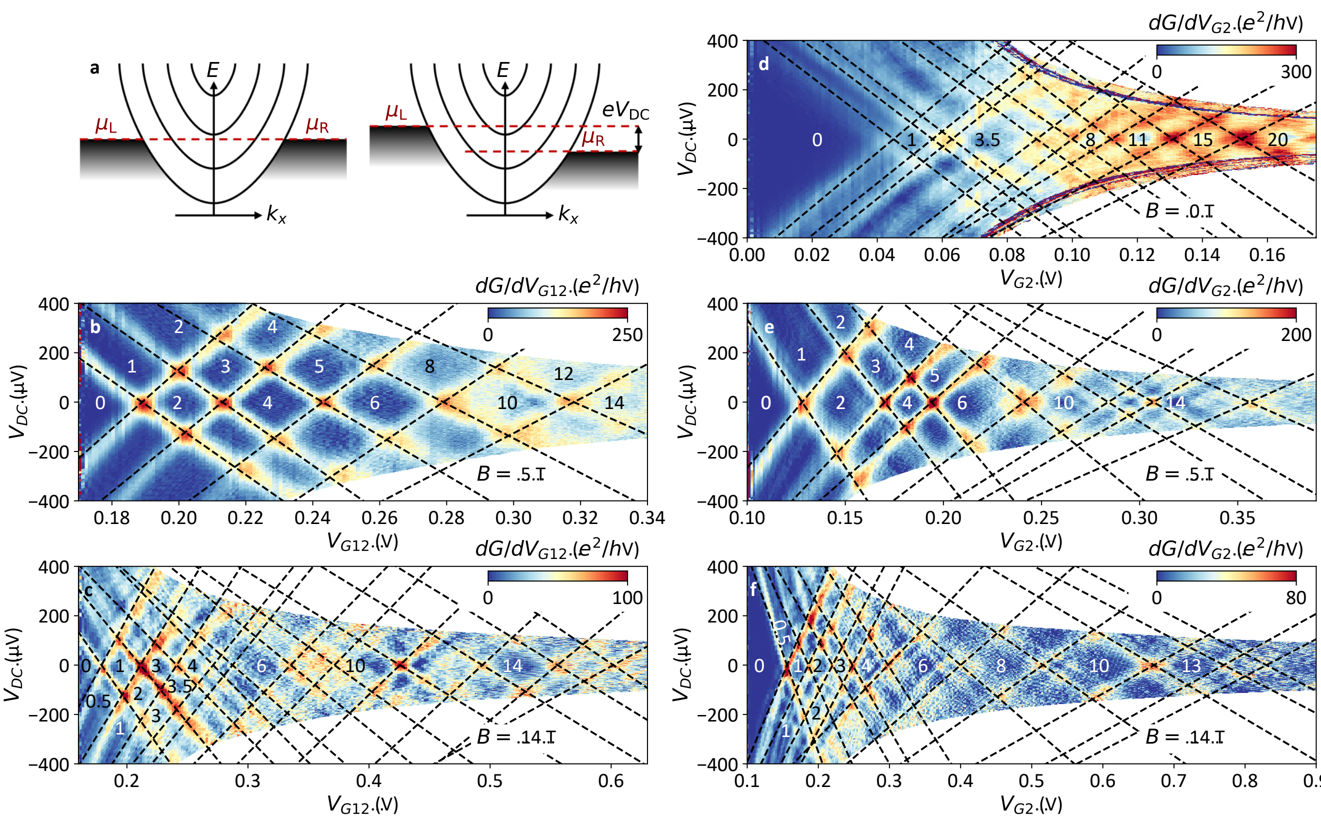

Fig. S7. DC bias spectroscopy of the QPC. (a) illustration of the constriction subband spectrum at (left) zero and (right) finite DC bias. (b-f) Transconductance maps with DC bias and split gate voltage. 4.6×10^{13} cm^{-2} cooldown at (b) $B = 5$ T (b), (c) 14 T. 3.0×10^{13} cm^{-2} cooldown at (d) $B = 0$ T, (e) 5 T, (f) 14 T. Conductance in units of e^2/h is labeled at selected well-defined plateaus. Dashed lines indicate subband slopes used to quantify the split gate lever arm.

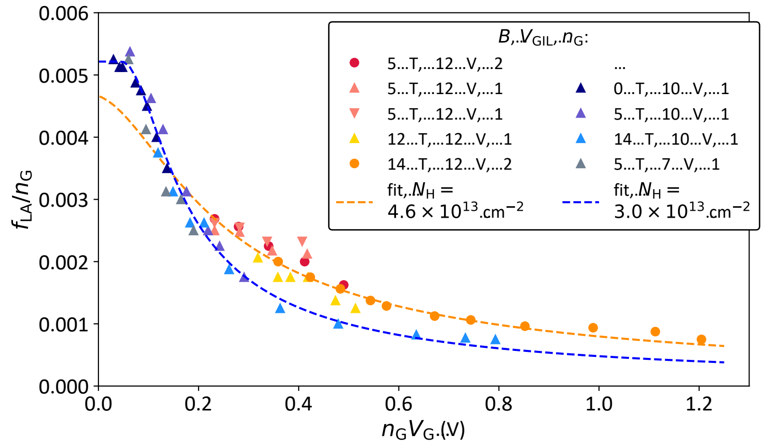

Fig. S8. Split gate lever arm non-linearity. Gate lever arm is shown against split gate voltage for the 4.6 (red symbols) and 3.0×10^{13} cm^{-2} (blue symbols) cooldowns. Both are normalized to number of gates used, $n_\mathrm{G} = 1$ if $V_\mathrm{G} = V_\mathrm{G2}$ or 2 if $V_\mathrm{G} = V_\mathrm{G12} = V_\mathrm{G1} = V_\mathrm{G2}$. Dashed lines are fits to equation S2.

the conventional pattern described above, due to strong subband overlap and, additionally, subband fractionalization that is discussed in more detail in section S3.

The gate lever arm factor can be extracted from the slope of the subbands: $f_\mathrm{LA} = dV_\mathrm{DC}/2dV_\mathrm{G}$ at dG/dV_G peaks (at $V_\mathrm{DC} = 0$). Dashed lines in Fig. S7 illustrate this analysis. It is evident that f_LA decreases at high filling, particularly at high B where subbands are clearly resolvable at high V_G. To account for this gate dependence, the f_LA is extracted as a function of V_G, from the subband slope near zero bias. Fig. S8 shows that measurements at different B collapse onto a single curve for each cooldown, when f_LA is plotted against gate voltage. In this plot V_G is corrected for long term drift (on the scale of weeks) in V_G between DC bias spectroscopy measurements. This was done by matching traces of $G(V_\mathrm{G})$ at zero bias to cuts from a single $G(V_\mathrm{G}, B)$ measurement. Both quantities were also normalized by $n_\mathrm{G} = 1$ or 2, depending on whether V_G12 pr V_G2 was used to tune μ.

We found that the collapsed curve is well described by a renormalized expression for the dielectric constant non-linearity of $SrTiO_3$ in electric field [S17]:

$$f_\mathrm{LA}(V_\mathrm{G}) = \frac{f_\mathrm{LA}(0) \cdot V_\mathrm{NL}}{\sqrt{V_\mathrm{NL}^2 + (V_\mathrm{G} - V_\mathrm{G0})^2}}. \tag{S2}$$

Here, V_NL is a parameter describing the sharpness of non-linearity, V_G0 is a horizontal offset, and $f_\mathrm{LA}(0)$ is the

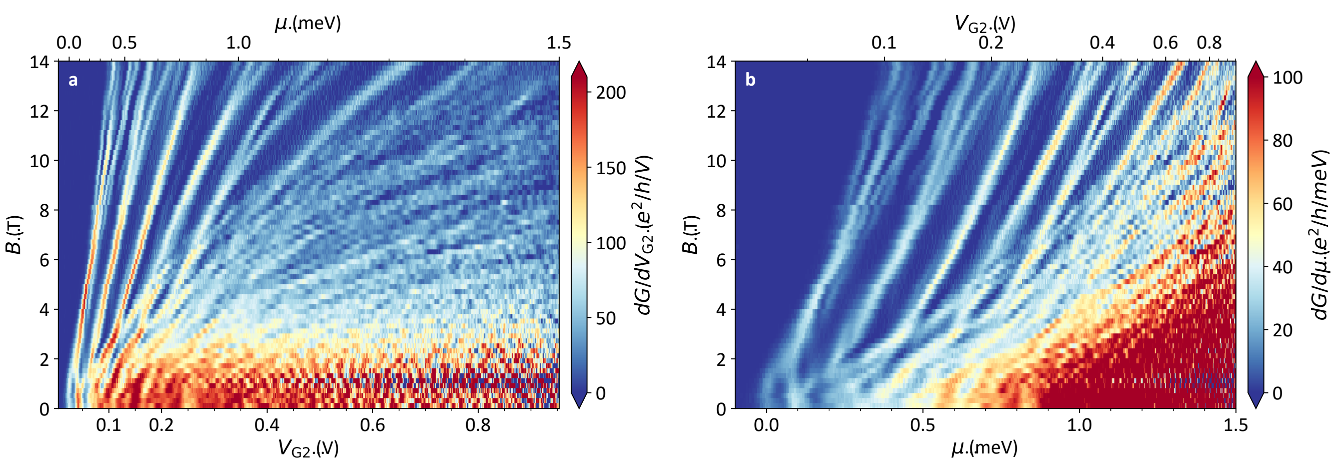

Fig. S9. Importance of accounting for gate lever arm non-linearity. Same measurement of transconductance with split gate voltage and B is plotted against (a) unprocessed V_G2, (b) V_G2 converted into μ with equation S3. Top axis shows the reversed conversion. Data are for the 3.0×10^{13} cm^{-2} cooldown, $V_\mathrm{GIL} = 10$ V.

maximum lever arm value at zero electric field across the split gate capacitor. This equation offers a compelling connection to the intrinsic dielectric non-linearity of $SrTiO_3$, arising from proximity to ferroelectricity. However, strong and qualitatively similar lever arm variations can be present even in conventional QPC's fabricated with linear gate dielectrics [S18]. We therefore do not attempt to disambiguate the physical origins of this non-linearity. The main utility of this analysis is in allowing for a straightforward conversion of $V_{\rm G}$ into an energy scale μ, at any B:

$$\mu(V_{\rm G}) = \int_{V_{\rm G0}}^{V_{\rm G}} f_{\rm LA}(V_{\rm G}) \cdot (V_{\rm G} - V_{\rm G0}) dV_{\rm G} = f_{\rm LA}(0) \cdot V_{\rm NL} \arctan\left(\frac{V_{\rm G} - V_{\rm G0}}{\sqrt{V_{\rm NL}^2 + (V_{\rm G} - V_{\rm G0})^2}}\right). \tag{S3}$$

To illustrate the importance of this correction, Fig. S9 presents the same measurement as $dG/dV_{\rm G12}(V_{\rm G12}, B)$ and $dG/d\mu(\mu, B)$. A measurement for the 3.0×10^{13} cm^{-2} cooldown is shown, where non-linearity is the strongest. Conversion of $V_{\rm G12}$ into μ reverses a significant warping of the subband shape, particularly at high filling. The validity of the conversion is also corroborated by the alignment of $d\mu/dB$ slopes for the lowest lying subbands in high B. In the framework of constriction subbands generated by both vertical and lateral confinement, this corresponds to electron mass being constant with subband index. Using a gate-independent $f_{\rm LA}$ would incorrectly indicate a decreasing mass at higher subband indices.

B. Constriction Hamiltonian in a three-dimensional confinement potential

In this section, we detail the theoretical framework used for the analysis of QPC subband evolution in magnetic field. The essential ingredient of the model is a three-dimensional potential (see main Figure 4a) with parabolic confinement in x, y (directions in the 2DEG plane, orthogonal and parallel to the current across the constriction, respectively), and z (normal to the 2DEG plane). A full derivation of the Hamiltonian and subband energies with x, y, and z confinement can be found in [S19]. A closely related model with y and z confinement has been presented in [S12]. The classic derivation with x and y saddle potential confinement can be found in [S20].

The expanded form of the Hamiltonian introduced in the main text, written in the Landau gauge with vector potential $A = (0, xB, 0)$, is:

$$\mathcal{H} = -\frac{\hbar^2}{2m_x^*} \cdot \frac{\partial^2}{\partial x^2} - \frac{\hbar^2}{2m_y^*} \cdot \frac{\partial^2}{\partial y^2} - \frac{\hbar^2}{2m_x^*} \cdot \frac{\partial^2}{\partial x^2} - \frac{m_x^* \epsilon_x^2 x^2}{2\hbar^2} + \frac{m_y^* \epsilon_y^2 y^2}{2\hbar^2} + \frac{m_z^* \epsilon_z^2 z^2}{2\hbar^2} + E_Z \sigma_z, \tag{S4}$$

Where the first three terms are the kinetic energy, the next three terms define the parabolic confinement potential, and the last term is the Zeeman energy with the B field applied in the z direction. At zero magnetic field, confinement potentials in $u = x, y, z$ can be approximated by the quantum harmonic oscillator model. With l_u, being the characteristic length scale of the constriction, $\omega_u = \hbar/m_u^*/l_u^2$ and $\epsilon_u(B{=}0) = \hbar\omega_u$. For $B > 0$, the cyclotron energy $\hbar\omega_c = eB/m_y^*$ renormalizes the x and y confinements [S19]:

$$\begin{aligned}
\epsilon_x^2(B) &= -\hbar^2\left(\omega_y^2 + \omega_c^2 - \omega_x^2\right) + \frac{\hbar^2}{2}\sqrt{\left(\omega_y^2 + \omega_c^2 - \omega_x^2\right)^2 + 4\omega_x^2\omega_y^2},\\
\epsilon_y^2(B) &= \hbar^2\left(\omega_y^2 + \omega_c^2 - \omega_x^2\right) + \frac{\hbar^2}{2}\sqrt{\left(\omega_y^2 + \omega_c^2 - \omega_x^2\right)^2 + 4\omega_x^2\omega_y^2},\\
\epsilon_z(B) &= \epsilon_z(B = 0) = \hbar\omega_z.
\end{aligned} \tag{S5}$$

In the limits of small ω_x, or large ω_c, or small ω_c the x and y confinement energies have a simpler form:

$$\begin{aligned}
\epsilon_x(B) &= \hbar\omega_x/\sqrt{1 + \omega_c^2/\omega_y^2},\\
\epsilon_y(B) &= \hbar\sqrt{\omega_y^2 + \omega_c^2},\\
\epsilon_z(B) &= \epsilon_z(B = 0) = \hbar\omega_z.
\end{aligned} \tag{S6}$$

For simplicity, the modeling of QPC subbands was carried using equation (S6). For ω_x/ω_y smaller than or of order unity, the energies given by equations (S5) and (S6) track each other closely with B, with the discrepancy peaking near $\omega_c = \omega_y$. It is below 12% for $\omega_x = \omega_y$, and below 6% for $\omega_x = 0.7\omega_y$ (typical value found in our analysis).

The Hamiltonian in equation (S4) is separable into x and y, z components. The y-z subband spectrum is discretized according to quantum numbers $|n_y, n_z, s\rangle$. $s = \pm 1/2$ is the electron spin and $n_{y,z} = 0, 1, 2, \ldots$ The x wavefunction

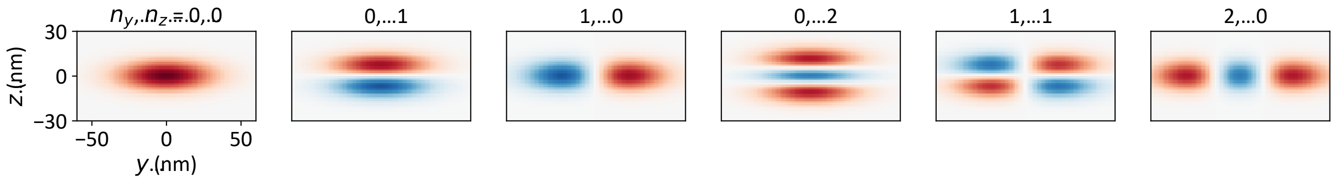

Fig. S10. Non-interacting model wavefunctions. Normalized harmonic oscillator wavefunction $(\phi_y(0,y)/\phi_y(0,0)) \cdot (\phi_z(0,z)/\phi_z(0,0))$ in the y–z plane for the six lowest lying subbands. Generated with equation (S10), using $\hbar\omega_y$, $\hbar\omega_z = 0.15$ meV, $m_y^* = m_e$, $m_z^* = 10m_e$. Natural length scales ares $l_y = 22.6$ nm, $l_z = 7.1$ nm.

component broadens these subbands. The subband energies are:

$$\epsilon_{yz}(n_y, n_z, s) = \epsilon_y\left(n_y + \frac{1}{2}\right) + \epsilon_z\left(n_z + \frac{1}{2}\right) + E_Z(B, s) \tag{S7}$$

To account for the unusual Y-shape of QPC subbands observed in B field, the Zeeman energy was modified to only turn on above a threshold field B_P:

$$\begin{aligned} E_Z(B{<}B_\mathrm{P}, s) &= 0 \\ E_Z(B{\geq}B_\mathrm{P}, s) &= g\mu_B s(B - B_\mathrm{P}) \end{aligned} \tag{S8}$$

The conventional Zeeman effect is recovered if $B_\mathrm{P} = 0$.

As a function of chemical potential μ (tuned in our experiment by V_G12), the contribution of each individual subband to the constriction conductance G is given by:

$$G(\mu, |n_y, n_z, s\rangle) = \frac{e^2}{h} \cdot \left[1 + \exp\left(-2\pi \cdot \frac{\mu - \epsilon_{yz}}{\epsilon_x}\right)\right]^{-1}. \tag{S9}$$

The subband conductance increases from 0 to e^2/h near $\mu = \epsilon_{yz}$. The step function-like transition is broadened by ϵ_x. The measured total conductance is a summation across all quantum numbers n_y, n_z, s.

The corresponding harmonic oscillator wavefunctions (shown in Fig. S10) along $u = y, z$ are:

$$\phi_u(n_u, u) = \left(\frac{\omega_u m_u}{\pi\hbar}\right)^{1/4} \frac{1}{\sqrt{2^{n_u} n_u!}} \exp\left(-\frac{\omega_u m_u u^2}{2\hbar}\right) H_{n_u}\left(u\sqrt{\frac{m_u\omega_u}{\hbar}}\right), \tag{S10}$$

Where H_{n_u} is Hermite polynomial of order n_u.

Fig. S11 shows a model spectrum generated by subbands up to $n = n_y + n_z = 9$ with approximately equal ω_z and ω_y. At $B = 0$, this generates dense packets of subbands with same total quantum number n. Both the width in μ and the number of subbands in each packer increases with n. The series of subbands generated by $n_z \geq 0$ and $n_y = 0$ is distinctive because of the low slope with B. It ends up isolated as the lowest lying at high B. Subbands with $n_y > 0$ generate a dense envelope under the $n_y = 1, n_z = 0$ subband. These features are distinctly present in our experiment, validating the use of this model.

A natural consequence of this model is the intermittent occurrence of high order subband degenaracies (beyond the spin degeneracy $s = \pm 1$). If $\omega_z = \omega_y$, the subband packets at constant $n = n_y + n_z$ become degenerate at $B = 0$. For small $\omega_z - \omega_y$, the packets can be quasi-degenerate within the broadening width in x. A full degeneracy is intermittently recovered when subbands at same n cross at a singular point in B. Furthermore, multiple series of coincident crossings in magnetic field between multiple subbands are generated naturally if the confinement potentials are harmonic, i.e. if the subband spacing is given by $\hbar\omega_y$ and $\hbar\omega_z$ that do not change with μ.

The conductance quantization between these packets follows the pattern $G \cdot h/e^2 = n(n+1) = 0, 2, 6, 12, 20, \ldots$ In [S21], a similar half-quantization pattern ($G \cdot h/e^2 = n(n+1)/2$) has been referred to as a "Pascal series". The factor of 2 comes from broken spin degeneracy, as the mechanism in [S21] for producing coincident subband crossing in B relied on matching the y and z confinement potentials to the cyclotron frequency and the Zeeman energy.

The discussion of our case above was for spin degenerate subbands at $B < B_\mathrm{P}$ and the Pascal-like series in G is generated by approximately matching y and z confinements only. Such subband crossings are a non-interacting effect and we do not make a claim of subband locking due to unconventional electron-electron interactions [S21]. The finite width of subband crossings in the B–μ space (as opposed to a point crossing) observed in our experiments (see main figures 3 and 4 in the main text and the following section S2 C) is consistent with subband broadening in x.

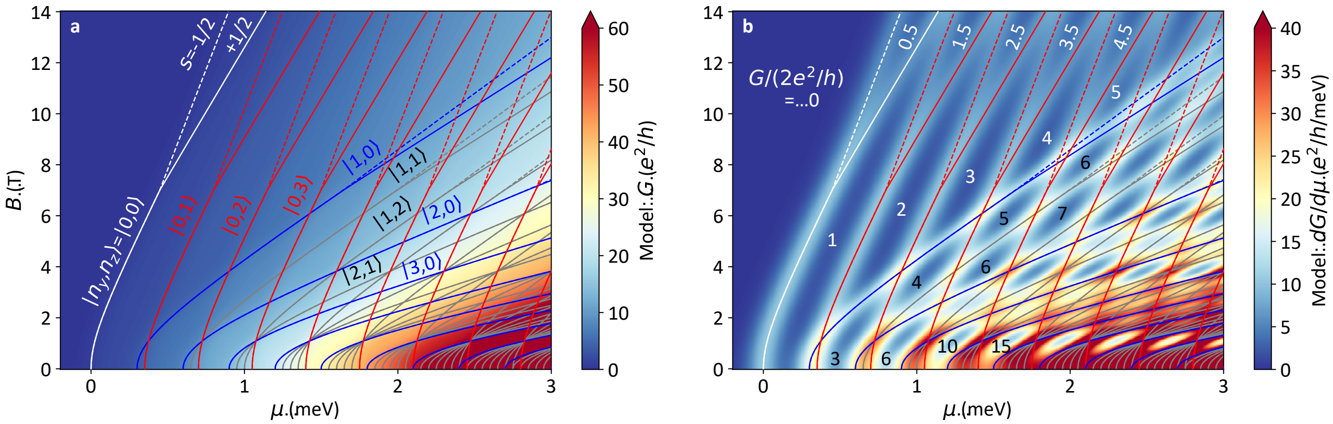

Fig. S11. 3D confined constriction model output. Model (a) conductance and (b) transconductance maps generated by the subband spectrum from equation S4-S9, using $\hbar\omega_x = 0.15$ meV, $\hbar\omega_y = 0.3$ meV, $\hbar\omega_z = 0.35$ meV, $m_y^* = 0.7m_e$, $B_{\mathrm{P}} = 7$ T, $g = 0.6$. Lines indicate subband energies. Selected quantum numbers are labeled in (a). Selected spin-degenerate mode numbers are labeled in (b).

C. Extended analysis of ballistic subbands in magnetic field

In this section, analysis of QPC conductance in magnetic field is presented in extended detail, starting from $dG/d\mu(B,\mu)$ maps, progressing to extraction of model parameters (ω_x, ω_y, ω_z, m_y^*, B_{P}, g), and generation of model transconductance maps for comparison with data. Discussion in the main text focuses on $dG/d\mu(B,\mu)$ data from the cooldown with Hall density $N_{\mathrm{H}} = 4.6 \times 10^{13}$ cm^{-2} and $V_{\mathrm{GIL}} = 12$ V. Here, it is analysed alongside two separate datasets measured during the 3.0×10^{13} cm^{-2} cooldown, at $V_{\mathrm{GIL}} = 10$ and 7 V.

Following the model framework from section S2 B, this analysis largely focuses on the $|n_y = 0, n_z, s = \pm 1/2\rangle$ set of subbands. They are clearly resolvable at magnetic fields above the position of the $|1, 0, \pm 1/2\rangle$ subband and the dense "forest" of subband crossings that lies below.

The $|0, n_z, \pm 1/2\rangle$ subband positions μ were identified algorithmically as points at which $G = (2n_z + 1) \cdot e^2/h$. In the spin degenerate state below B_{P}, this is the middle of the transition between conductance plateaus. In presence of non-zero Zeeman splitting above B_{P} that is symmetric with respect to spin, the procedure is still expected to give

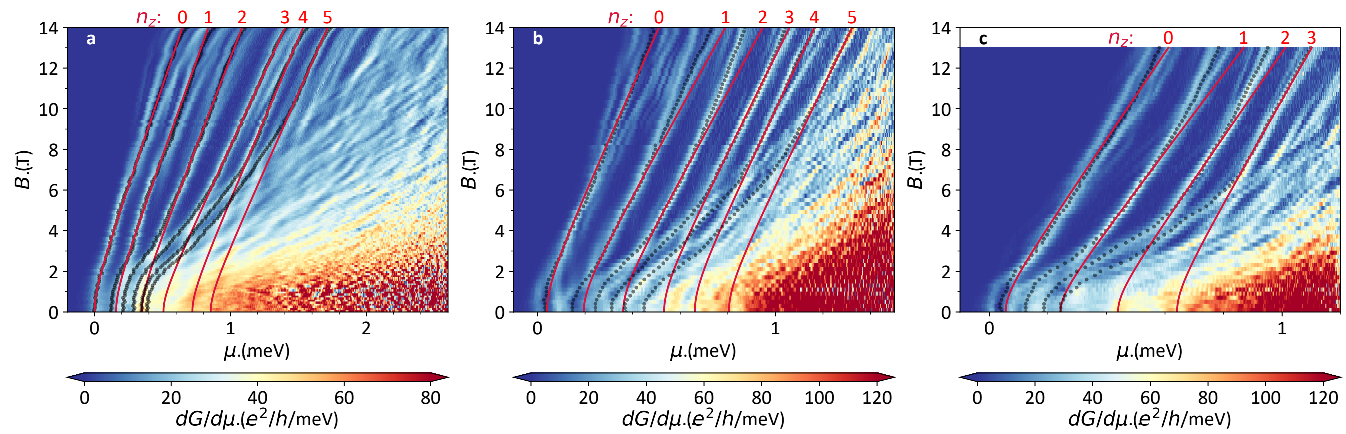

Fig. S12. Fits to individual subbands. Transconductance maps with μ and B are shown for N_{H} (10^{13} cm^{-2}), V_{GIL} (V) = 4.6, 12 (a); 3.0, 10 (b); 3.0, 7 (c). Black markers are fixed conductance points used to algorithmically identify subband positions. Red lines are fits to equation (S7) for $|0, n_z \geq 0, \pm 1/2\rangle$ subbands.

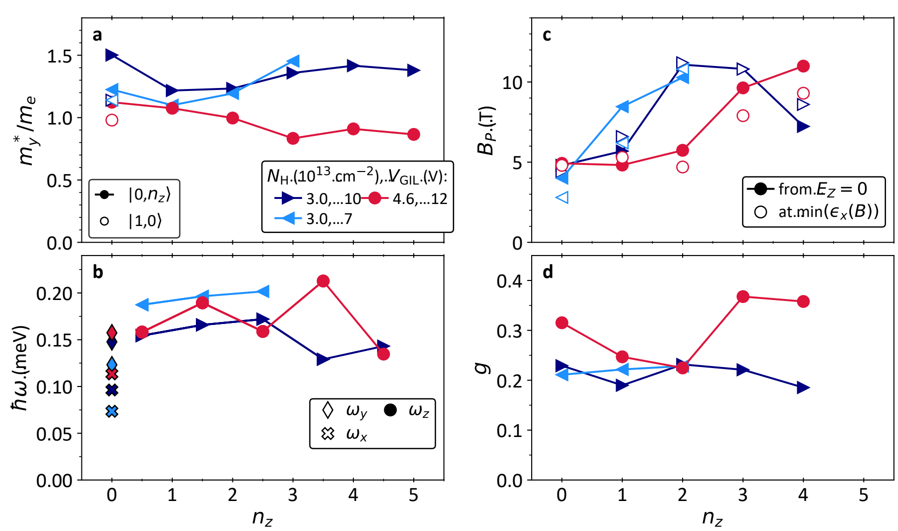

Fig. S13. Summary of subband parameters from analysis described in text. Marker color indicates device state, as noted in (a). (a) Effective electron mass, filled markers are from $|0, n_z > 0, \pm 1/2\rangle$ subbands, unfilled markers are from the $|1, 0, \pm 1/2\rangle$ subband. (b) x, y, and z confinement strengths. (c) Field scale for two-fold degeneracy breaking. Filled markers are from fits to Zeeman splitting above B_{P}, unfilled markers are from subband broadening minima in B. (d) g factors from fits to Zeeman splitting above B_{P}.

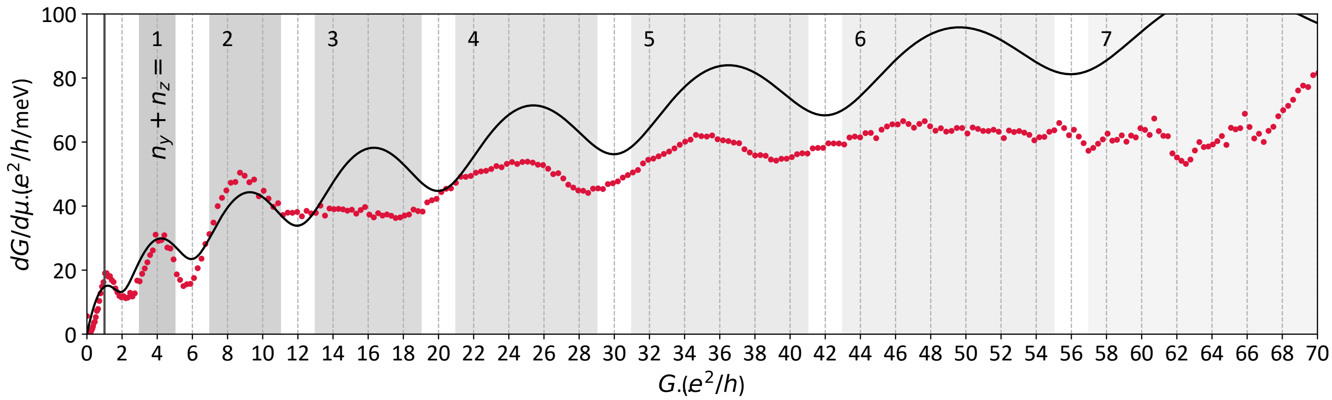

Fig. S14. Subband packets at zero field. Parametric plot of transconductance against conductance at $B = 0$. Markers are data for the 4.6×10^{13} cm^{-2} cooldown. Shaded regions indicate the extent of subband packets with same $n_y + n_z$, used to estimate $\hbar\omega_y$ and $\hbar\omega_z$ shown in Fig. S15. Black line is the resulting output of equations (S7) and (S9) with $\hbar\omega_x = 0.11$ meV.

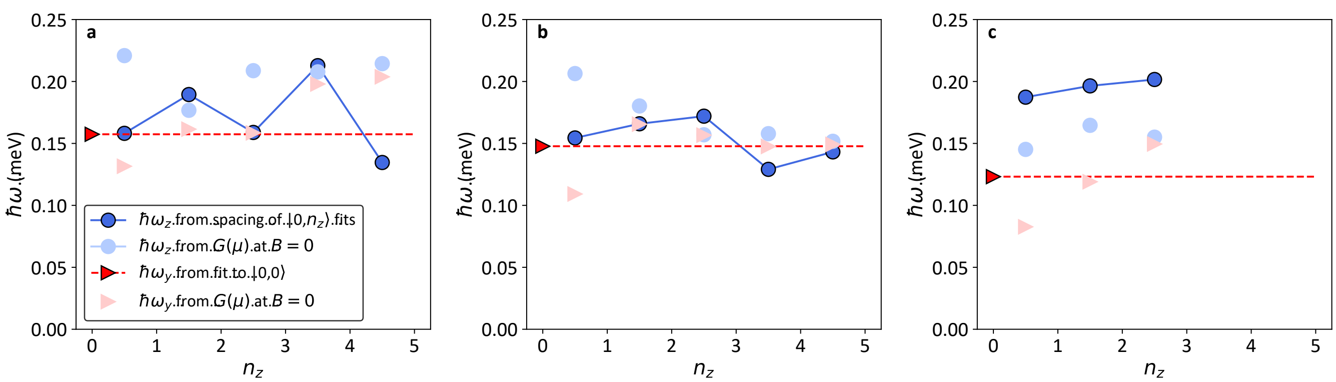

Fig. S15. Subband spacing. Comparison of separate estimates for $\hbar\omega_y$ amd $\hbar\omega_z$: from individual fits in the μ-B space, and from subband packet analysis in $G(\mu)$ at $B = 0$. $N_{\rm H}$, $V_{\rm GIL} = 4.6 \times 10^{13}$ cm^{-2}, 12 V (a); 3.0×10^{13} cm^{-2}, 10 V (b); 3.0×10^{13} cm^{-2}, 7 V (c).

an extrapolation of the spin degenerate subband. In practice, the target G needed to be adjusted slightly below the ideal value: $G = 1, 2.8, 4.7, 6.8, 8.9, 10.5\ e^2/h$ for the 4.6×10^{13} cm^{-2} cooldown. This is consistent with the presence of a small series resistance between the voltage probes and the constriction.

These subbands energies can be fitted to equation (S7). The relevant model parameters are m_y^* (giving $\hbar\omega_c$ and the slope at high B) and $\hbar\omega_z$ (subband spacing in μ). If μ is referenced to the lowest lying subband, $\hbar\omega_y$ only has a minor effect on the trace shape, changing its curvature near $B = 0$. Because of the crossings with the $|1, 0, \pm 1/2\rangle$ subband, $\hbar\omega_y$ can only be reliably fitted to the lowest-lying $|0, 0, \pm 1/2\rangle$ subband. This value of $\hbar\omega_y$ was used for subsequent fits to $|0, n_z > 0, \pm 1/2\rangle$, a choice corroborated by independent estimates from analysis of conductance at $B = 0$ (see below). The resulting fit traces are shown in Fig. S12. The extracted confinement parameters are shown in Fig. S13a,b.

A separate estimate of both $\hbar\omega_y$ and $\hbar\omega_z$ can be extracted from the $G(\mu)$ trace at $B = 0$. As illustrated in Fig. S11, in the case where $\hbar\omega_y$ is close to but smaller than $\hbar\omega_z$, the subbands are grouped in packets of increasing width. Fig. S14 shows that this picture is consistent with the experimental situation for the 4.6×10^{13} cm^{-2} cooldown, remarkably up to $G \approx 50\ e^2/h$. We see transconductance peaks with increasing width in G. In the 3D confined constriction model, these are packets of subbands with the same $n_y + n_z$ quantum number, and with increasing numbers of mixed $|n_y > 0, n_z > 0, s = \pm 1/2\rangle$ subbands. If $\omega_y < \omega_z$, $|n_y > 0, 0, s = \pm 1/2\rangle$ and $|0, n_z > 0, s = \pm 1/2\rangle$ are the first and last subbands in the packet, respectively. $\hbar\omega_y$ can be estimated as the spacing in μ between points with $G \cdot h/e^2 = 1, 3, 7, 13, 21, \ldots$ (first transition in each subband packet). Similarly an estimate for $\hbar\omega_z$ is the spacing in μ between points with $G \cdot h/e^2 = 1, 5, 11, 19, 29, \ldots$ (last transition in each subband packet). Deviations in the experiment from the simple subband packet pattern described here are likely due to a combination of finite

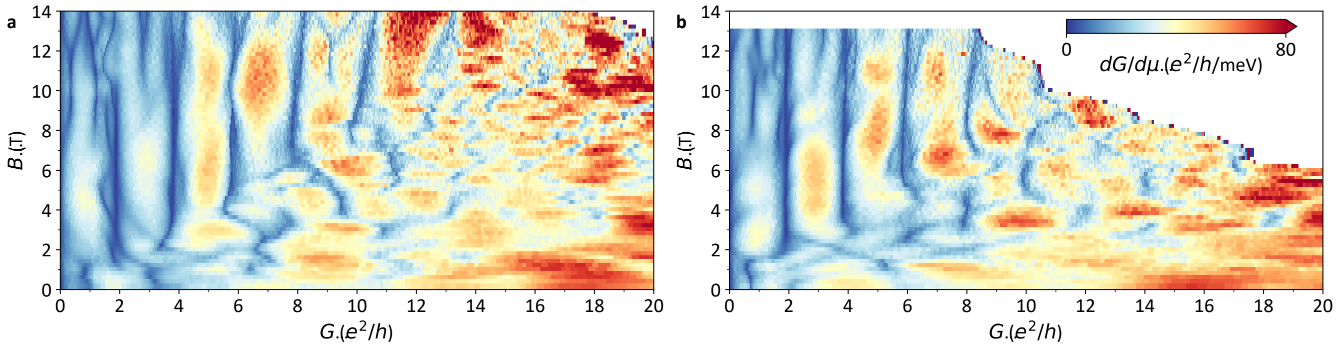

Fig. S16. Supplementary conductance quantization data. Parametric transconductance plots for the 3.0×10^{13} cm^{-2} cooldown, $V_{\rm GIL} = 10$ V (a), 7 V (b).

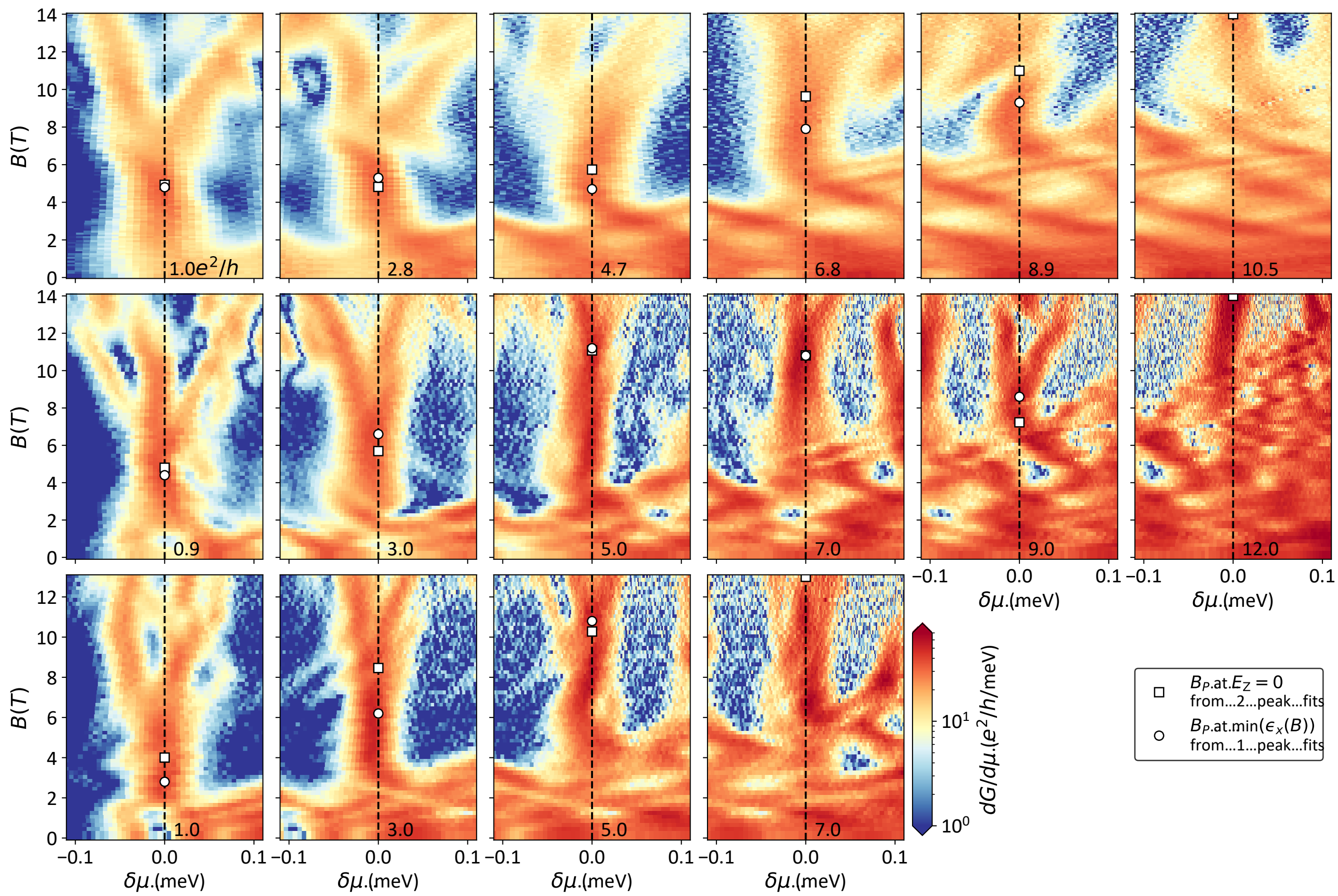

Fig. S17. Y shape of the subbands. Transconductance plots, centered in chemical potential based on G value indicated in each plot. From left to right, plots are for $|0, n_z > 0, \pm 1/2\rangle$ subbands with increasing n_z. $N_{\rm H}$ (10^{13} cm^{-2}), $V_{\rm GIL}$ (V) = 4.6, 12 (top row); 3.0, 10 (middle row); 3.0, 7 (bottom row). White markers indicate extracted $B_{\rm P}$ values, see Fig. S19, S20, and text for discussion of analysis procedure.

series resistance, increasing overlap between neighboring subband packets, and insufficiently granular quantification of subband broadening (discussed below). Fig. S15 shows that these estimates are consistent with the results from fitting individual subband positions in the μ-B space. For the 3.0×10^{13} cm^{-2} data taken at $V_{\rm GIL} = 7$ V (Fig. S15c), the assumption $\omega_y \approx \omega_z$ is not accurate, leading to a larger discrepancy between the two analysis approaches.

For the 3.0×10^{13} cm^{-2} cooldown, additional fractionalization physics are at play. The first transition at $B = 0$ is between $G = 0$ and $\approx 1\, e^2/h$ (in Fig. S16a), 0 and $\approx 0.5\, e^2/h$ (in Fig. S16b). An in-depth discussion of fractionalization

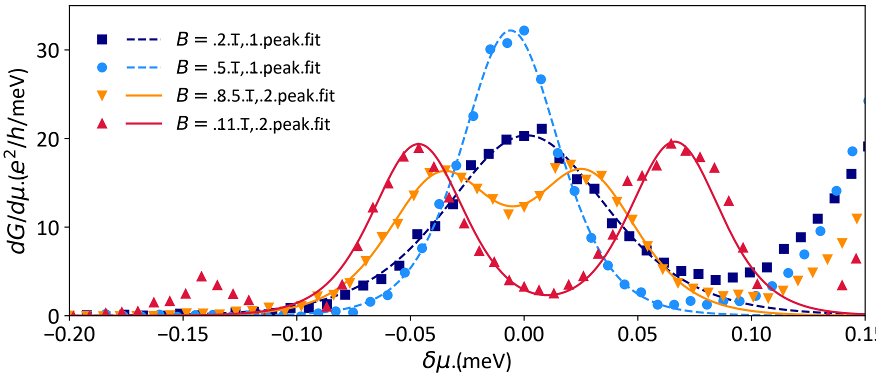

Fig. S18. Peak fitting. Examples of transconductance fits to equation (S11) and (S12). Data shown are $dG/d\mu$ line cuts at selected fields, centered at the $|0,0,\pm 1/2\rangle$ subband, 4.6×10^{13} cm^{-2} cooldown.

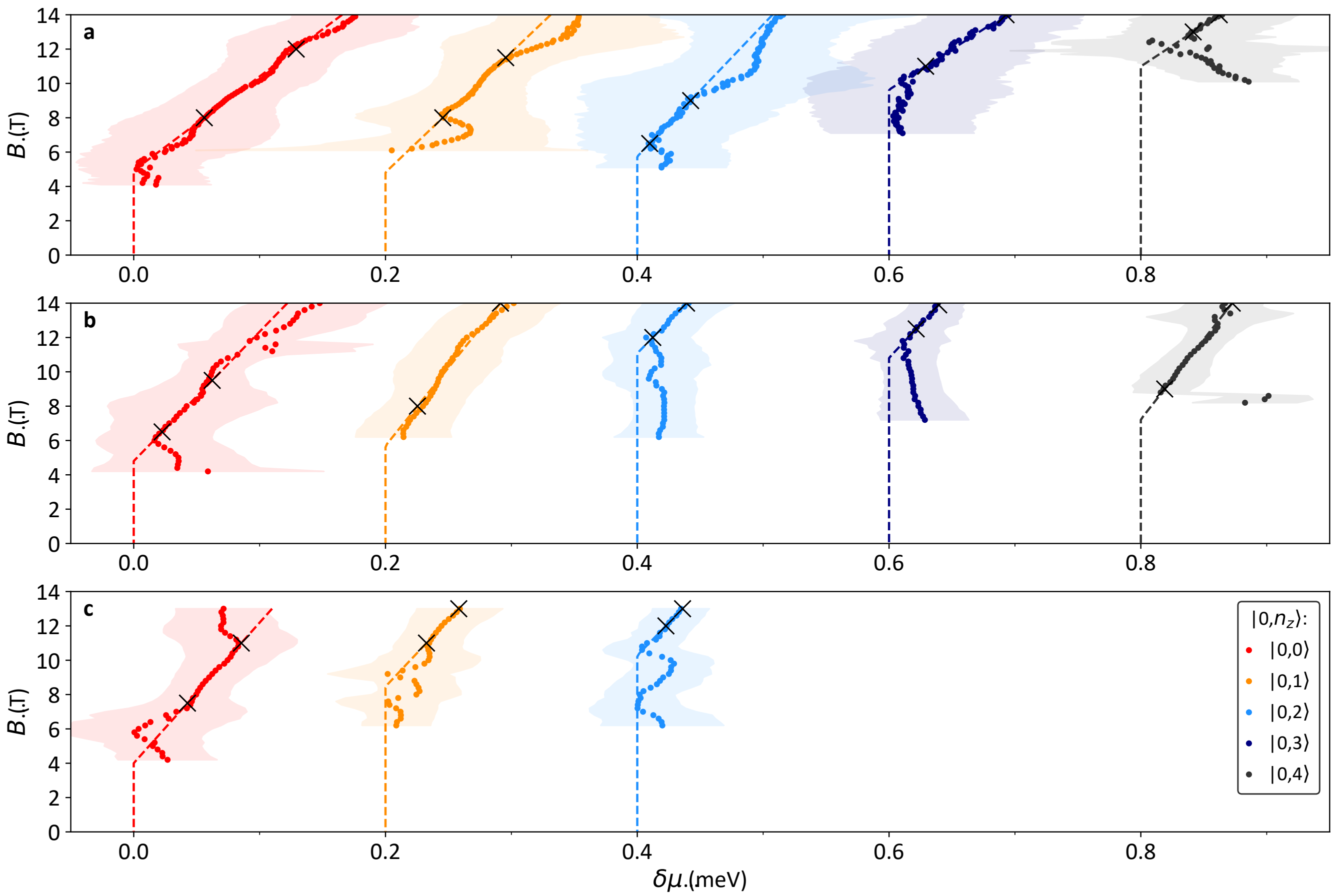

Fig. S19. Zeeman splitting. Fitted double peak spacing ($\epsilon_{\mathrm{F2R}} - \epsilon_{\mathrm{F2L}}$) is shown as markers. Shading is the combined fitted peak width ($\hbar\omega_{\mathrm{F2L}}/2+\hbar\omega_{\mathrm{F2R}}/2$). Dashed lines are fits to $g\mu_B(B - B_{\mathrm{P}})$. Data for different subbands are arbitrarily offset in $\delta\mu$ for clarity. N_{H} (10^{13} cm^{-2}), V_{GIL} (V) = 4.6, 12 (top row); 3.0, 10 (middle row); 3.0, 7 (bottom row).

is presented in section S3. For the purpose of subband analysis, we found that using the expected G as a proxy for subband location in μ gives results that are consistent with the fitting analysis at $B > 2$ T (where fractionalization is suppressed). Similarly to Zeeman splitting, one would expect this procedure to work reliably if the fractional splitting is symmetric in μ.

In Fig. S17, the $|0, n_z, \pm 1/2\rangle$ subbands are centered in μ, using the procedure described above to get the offset in μ

(location of G in the middle of transition between plateaus). The removal of the tilting in B from the ω_c contribution allows for a qualitative assessment of the Zeeman splitting being more consistent with a "Y" shape ($B_\mathrm{P} > 0$) rather than the conventional "V" shape ($B_\mathrm{P} = 0$).

For a more quantitative assessment, we performed least-squares peak fitting to individual $dG/d\mu$ cuts at constant B. We used the line shape given by the derivative of equation (S9):

$$\frac{dG}{d\mu} = \frac{2\pi I_\mathrm{F1}}{\hbar\omega_\mathrm{F1}} \cdot \frac{\exp\left(-2\pi \cdot \frac{\mu-\epsilon_\mathrm{F1}}{\hbar\omega_\mathrm{F1}}\right)}{\left(1+\exp\left(-2\pi \cdot \frac{\mu-\epsilon_\mathrm{F1}}{\hbar\omega_\mathrm{F1}}\right)\right)^2}, \tag{S11}$$

where the fitting parameters are I_F1 (peak height), ϵ_F1 (horizontal offset in μ), and $\hbar\omega_\mathrm{F1}$ (peak broadening). This single peak description is meaningful at small B above the $|1, 0, \pm 1/2\rangle$ subband, and up to B slightly above B_P where Zeeman split peaks become clearly resolved.

In the region above B_P, we separately fitted the $dG/d\mu$ cuts to a double-peak lineshape:

$$\frac{dG}{d\mu} = \frac{2\pi I_\mathrm{F2L}}{\hbar\omega_\mathrm{F2L}} \cdot \frac{\exp\left(-2\pi \cdot \frac{\mu-\epsilon_\mathrm{F2L}}{\hbar\omega_\mathrm{F2L}}\right)}{\left(1+\exp\left(-2\pi \cdot \frac{\mu-\epsilon_\mathrm{F2L}}{\hbar\omega_\mathrm{F2L}}\right)\right)^2} + \frac{2\pi I_\mathrm{F2R}}{\hbar\omega_\mathrm{F2R}} \cdot \frac{\exp\left(-2\pi \cdot \frac{\mu-\epsilon_\mathrm{F2R}}{\hbar\omega_\mathrm{F2R}}\right)}{\left(1+\exp\left(-2\pi \cdot \frac{\mu-\epsilon_\mathrm{F2R}}{\hbar\omega_\mathrm{F2R}}\right)\right)^2}, \tag{S12}$$

With the fitting parameters I_F2L, ϵ_F2L, $\hbar\omega_\mathrm{F2L}$ for the "left" peak and I_F2R, ϵ_F2R, $\hbar\omega_\mathrm{F2R}$ for the "right" peak. Examples of single and double peak fitting are shown in Fig. S18.

The quantity of interest for quantifying the Zeeman effect is the peak spacing $\epsilon_\mathrm{F2R} - \epsilon_\mathrm{F2L}$. Fig. S19 shows that its B dependence can be fitted to the modified Zeeman splitting in equation (S8), with B_P and g as fitting parameters. As indicated by red "x" markers, the fitting range in B was restricted to exclude spurious features, particularly near B_P and at very high B. Considerable interpretation uncertainty could not be excluded from the analysis of individual subbands. But the overall pattern in Fig. S19 is robustly consistent with $g = 0.15$-0.35 and B_P of at least 4 T (Fig. S16), increasing above 14 T (maximum available in our experiment) with n_z.

Separate quantities of interest from these fits are the broadening parameters $\hbar\omega_\mathrm{F1}$, $\hbar\omega_\mathrm{F2L}$, $\hbar\omega_\mathrm{F2R}$, shown in Fig. S20 for the $|0, 0, \pm 1/2\rangle$ subband. In the picture of constriction conductance given equation (S9), these broadening widths correspond to longitudinal potential energy ϵ_x and are expected to scale with B as in equation (S6). If one uses m_y^* and ω_y from subband position fitting described above, a fit to equation (S6) with ω_x provides a reasonably close description of $\hbar\omega_\mathrm{F1}$ at $B < B_\mathrm{P}$ (dashed line in Fig. S20), but with an overly abrupt decrease in B. The description is significantly improved by adding a B-independent contribution $\hbar\omega_{x0}$:

$$\epsilon_x(B) = \hbar\omega_{x0} + \frac{\hbar\omega_x}{\sqrt{1 + \omega_c^2/\omega_y^2}}. \tag{S13}$$

The solid line in Fig. S20 is a fit to $\hbar\omega_{x0}$ and $\hbar\omega_x$. It captures well the low B behavior. The increase seen in all broadening widths near B_P is a natural consequence of emergent peak splitting, which is not captured by this

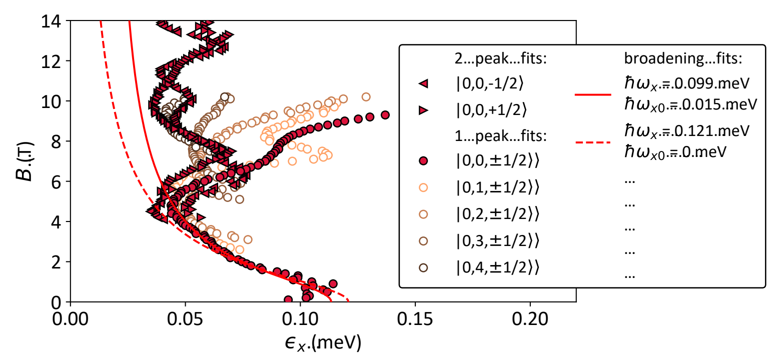

Fig. S20. Subband broadening. Fitted peak width in field. Circle symbols show single peak fits (valid below $B_\mathrm{P} = 5$ T) are shown for $|0, n_z > 0, \pm 1/2\rangle$ subbands. For $|0, 0, \pm 1/2\rangle$, broadening from double peak fits is also shown. Lines are fits to equation (S13) below B_P for $|0, 0, \pm 1/2\rangle$.

model. At high B, $\hbar\omega_{\mathrm{F2L}}$ and $\hbar\omega_{\mathrm{F2R}}$ fluctuate significantly due to spurious subband features. But the description by equation (S13) aligns well with lower range of $\hbar\omega_{\mathrm{F2L}}$ and $\hbar\omega_{\mathrm{F2R}}$, as one would expect for a saturating dependence overlayed with spurious peaks. A reliable extraction of broadening parameters is unfortunately only feasible for the $|0,0,\pm1/2\rangle$ subband. For $n_z > 0$, the key region at low B is overlayed with the $n_y > 0$ subbands. But the $\hbar\omega_{\mathrm{F1}}$ widths at extracted above $|1,0,\pm1/2\rangle$ for $n_z > 0$ are reasonably close to the $|0,0,\pm1/2\rangle$ case. Therefore, for the full modelling of the subband spectrum bellow, the $\hbar\omega_{x0}$ and $\hbar\omega_x$ fit values from $|0,0,\pm1/2\rangle$ were used for all subbands.

The B dependence of $\hbar\omega_{\mathrm{F1}}$ encodes another useful piece of information. Above we related its increase near B_{P} to the onset of peak splitting. Empirically, we found that the location of the minimum of $\hbar\omega_{\mathrm{F1}}$ in B provides an independent estimate of B_{P}. As illustrated in Fig. S13 and S17, such estimates are close to the values of B_{P} extracted from the double-peak analysis (fitting $\epsilon_{\mathrm{F2R}} - \epsilon_{\mathrm{F2L}}$ to equation (S8). The similarity between the two independently extracted values of B_{P} corroborates both its magnitude, and the increasing trend with n_z.

The ultimate goal of this analysis is to use equation (S9) to simulate the full spectrum of $|n_y, n_z, s\rangle$ states up to a sufficiently large $n = n_y + n_z$ to cover the experimental range in μ. This involves extrapolating the parameters measured at low n_z and $n_y = 0$ to high n, where the subbands are too densely packed for reliable analysis. For g, an average of measured values was used for all other subbands. Measured B_{P} was used for subbands within the same $n = n_y + n_z$ packet. At higher n it was set to 14 T (i.e. no splitting detected in the experimental range). For m_y^*, the last measured value was extrapolated to higher n_z for $|0, n_z, \pm1/2\rangle$ subbands. A separate m_y^* value was slightly adjusted to fit the $|1,0,\pm1/2\rangle$ state (unfilled symbols in Fig. S13a), which was then used for all subbands with $n_y > 0$. For ϵ_x, $\hbar\omega_{x0}$ and $\hbar\omega_x$ from the fit to $|0,0,\pm1/2\rangle$ was used for all subbands. For $\hbar\omega_z$, same measured value was used within the same $n = n_y + n_z$ packet, and the last measured value was used for higher n. For $\hbar\omega_y$, the $|0,0,\pm1/2\rangle$ fit value was used for all other subbands.

Figures S21, S22, S23 show direct comparisons in three different device states between measured $G(\mu, B)$, $dG/d\mu(\mu, B)$ maps and the model summing equation (S9) across quantum numbers $n_y, n_z = 0, 1, ..., 20$, and $s = \pm1/2$. Given the complexity of the measured pattern and the relative simplicity of the model, the correspondence between them is remarkable. Of particular note is the close capture of the dichotomy between "fast in B" $|n_y > 0, n_z, \pm1/2\rangle$ and "slow in B" $|0, n_z > 0, \pm1/2\rangle$ subbands. For lower lying bands, the model accurately captures subband broadening and peak heights $dG/d\mu$ (in real units of e^2/h/meV), including the maximized sharpness of $|0, n_z, \pm1/2\rangle$ transitions near B_{P}.

Some shortcomings of the model: 1) The broadening at high n and below the $|0,1,\pm1/2\rangle$ subband is underestimated. Increased broadening is likely a combination of a slowly-evolving longitudinal potential potential with split gate voltage and inter-subband scattering. We did not attempt to disentangle and quantify these effects; 2) in the 3.0×10^{13} cooldown data, G at low B is fractionalized in an unusual way that is not captured by the model, see further discussion in section S3; 3) At high B, a tendency of G quantization to fractionalize into steps smaller than e^2/h is present in all data sets. Very pronounced fractionalization effects are often present in III-V based QPC's in the quantum Hall regime, due to interplay with the disorder potential around the constriction [S22]. It is reasonable to speculate that in our device we might be seeing precursors to a similar regime.

Additional corroboration of the analysis is provided by comparing the characteristic length scales $l_u = \sqrt{\hbar/\omega_u/m_u^*}$ of the $u = x, y, z$ confinement potentials. The transverse length estimate (with $\hbar/\omega_y$ and m_y^** from the fit to the $|0,0,\pm1/2\rangle$ subband) is l_y = 22-23 nm for all cooldowns. This is smaller than, but close to the 40 nm lithographic spacing between the split gates. Assuming $m_x^* = m_y^*$, the longitudinal length is slightly larger for all cooldowns: 26-30 nm. This is consistent with the sharp split gate design of our device. For the vertical confinement, the electron mass m_z^* is expected to be significantly larger than m_x^* and m_z^* due to the anisotropy of electronic band structure in $SrTiO_3$ 2DEGs [S23]. We do not have a measurement of m_z^* in our device, but taking an estimate $m_z^* = 10m_e$ gives l_z = 6-7 nm. $SrTiO_3$-based 2DEGs with carrier densities in the 10^{13}-10^{14} cm^{-2} typically have a vertical extent estimated in the 1-15 nm range [S23, S24], consistent with our estimate of l_z.

An interesting comparison is between the two different data sets taken at $V_{\mathrm{GIL}} = 10$ and 7 V during the 3.0×10^{13} cm^{-2}. The average of l_z across measured subbands is 6.2 and and 7.1 nm for $V_{\mathrm{GIL}} = 7$ and 10 V respectively. This difference is consistent with the picture of V_{GIL} (at sufficiently low T to freeze the ionic liquid) acting similarly to a back gate, incrementally modulating the vertical depth of the 2DEG [S3].

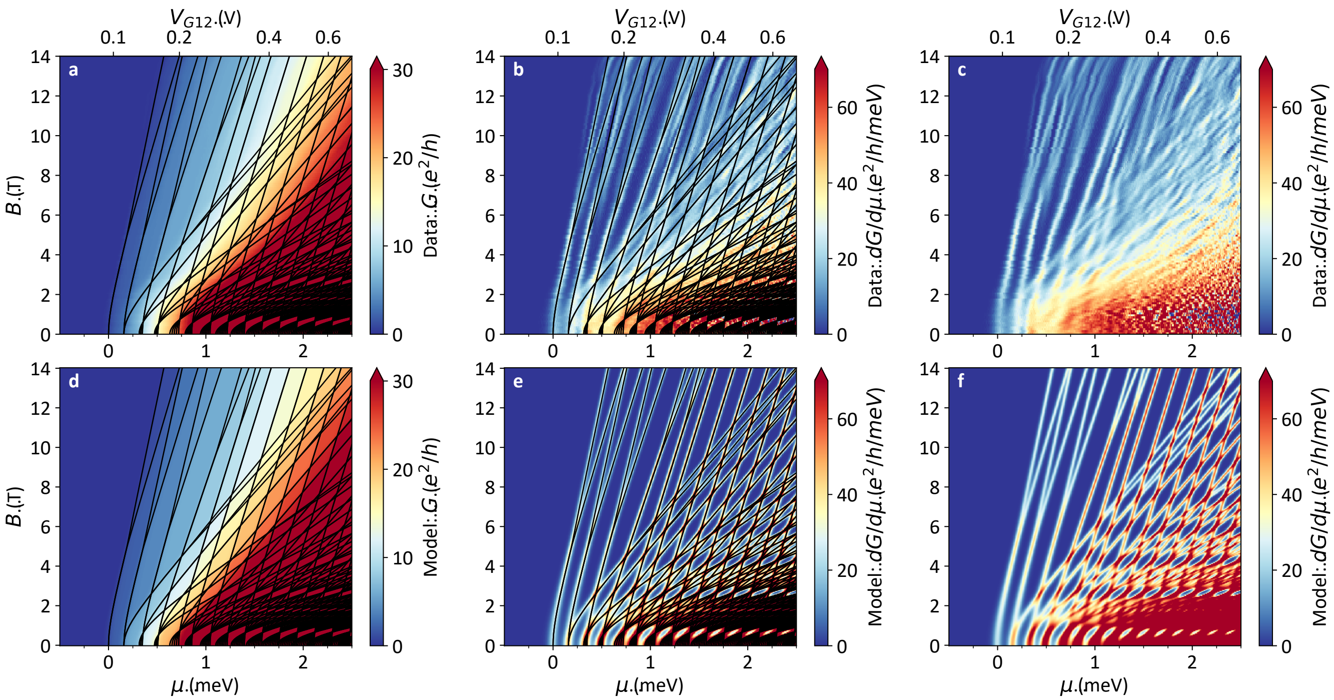

Fig. S21. Direct data-model comparison. 4.6×10^{13} cm^{-2} cooldown. (a,d) conductance map (b,c,e,f) transconductance map. Lines in (a,b,d,e) are subband energies. All data are shown against chemical potential, converted from raw split gate voltage shown as top axis in (a-c).

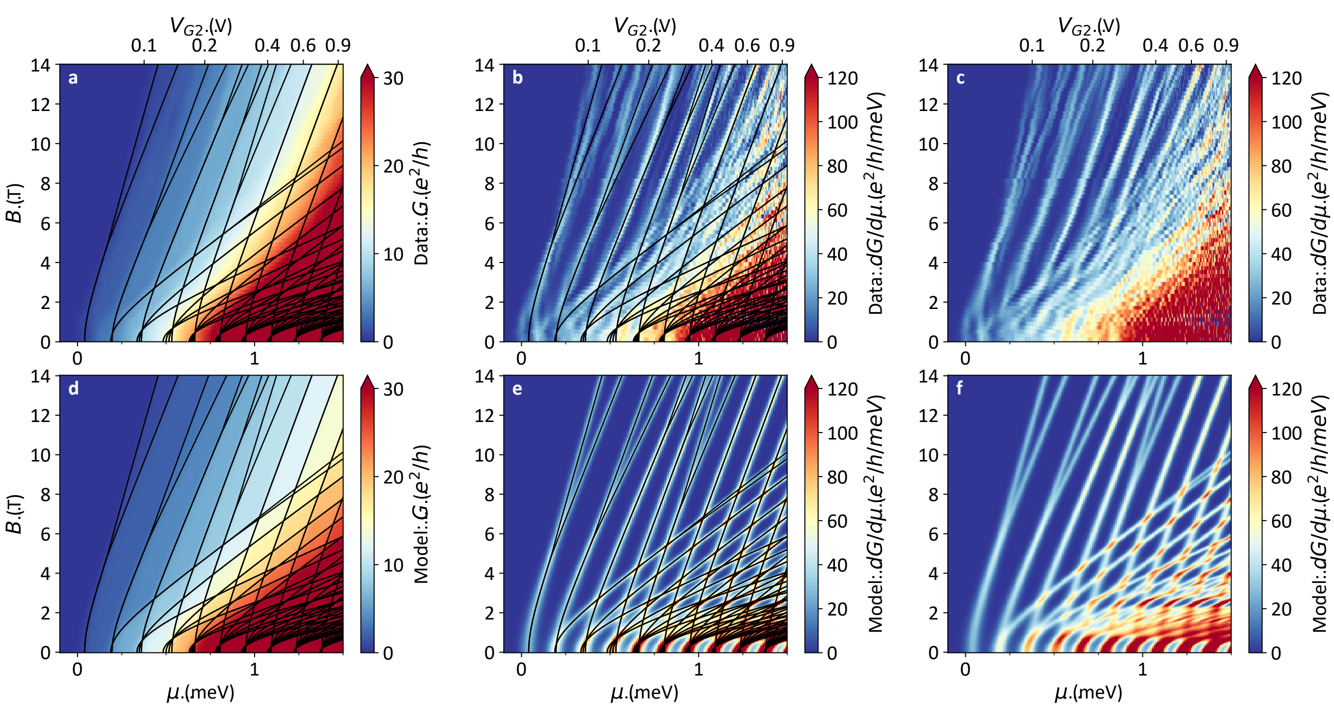

Fig. S22. Direct data-model comparison. 4.6×10^{13} cm^{-2} cooldown, $V_{\mathrm{GIL}} = 10$ V. Same plots as Fig. S21

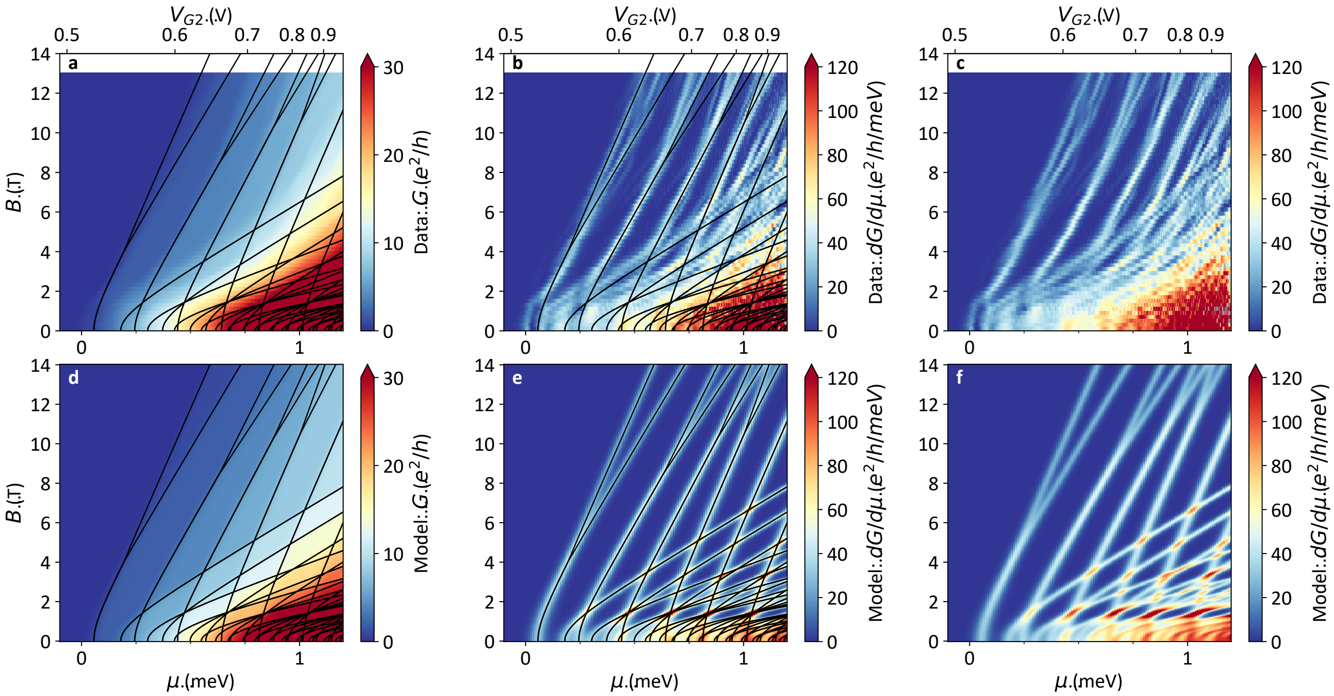

Fig. S23. Direct data-model comparison. 4.6×10^{13} cm^{-2} cooldown, $V_{\mathrm{GIL}} = 7$ V. Same plots as Fig. S21

D. Reduction of Zeeman splitting due to nanostructure confinement

In this section, we present a simple band model for the electrons at the interface between $SrTiO_3$ and the ionic liquid that could explain why the Landé g factor [Eq. (1) in the main text] is smaller than in standard 2D interfaces due to the transverse confinement of the electrons in the QPC.

In STO-based interfaces, the Fermi energy lies in the $3d$ t_{2g} orbitals d_{yz}, d_{xz}, and d_{xy} of the Ti ions near the interface [S25, S26]. In the orbital and spin basis $(d_{yz}, d_{xz}, d_{xy}) \otimes (\uparrow, \downarrow)$, the electron dynamics can be accounted for by a six-dimensional Hamiltonian H of the form [S13, S26–S28]

$$H = H_0 + H_{\mathrm{aso}} + H_{\mathrm{a}} \tag{S14}$$

where the Hamiltonian

$$H_0 = \begin{pmatrix} \frac{\hbar^2 k_x^2}{2m_h} + \frac{\hbar^2 k_y^2}{2m_l} & 0 & 0 \\ 0 & \frac{\hbar^2 k_x^2}{2m_l} + \frac{\hbar^2 k_y^2}{2m_h} - \Delta E_y & 0 \\ 0 & 0 & \frac{\hbar^2 k_x^2}{2m_l} + \frac{\hbar^2 k_y^2}{2m_l} - \Delta E_z \end{pmatrix} \otimes \mathbb{1}_2 + \mathbb{1}_3 \otimes \left(\frac{g_0}{2}\mu_B B\right)\sigma_z \tag{S15}$$

contains the kinetic energies of the electrons with effective heavy and light masses m_h and m_l, the bare Zeeman splitting energy with initial Landé factor g_0 and Pauli operator σ_z, and the confinement-induced splitting energies ΔE_y and ΔE_z along y and z due to the presence of the ionic liquid and the additional transverse trapping potential used to realize the QPC. Here, $\mathbb{1}_2$ and $\mathbb{1}_3$ are identity operators acting respectively on the two-dimensional spin and three-dimensional orbital Hilbert spaces. The Hamiltonian H_{aso} describes the effects of atomic spin-orbit coupling and takes the form

$$H_{\mathrm{aso}} \propto \mathbf{L} \cdot \boldsymbol{\sigma} = i\Delta_{\mathrm{ASO}} \begin{pmatrix} 0 & \sigma_z & -\sigma_y \\ -\sigma_z & 0 & \sigma_x \\ \sigma_y & -\sigma_x & 0 \end{pmatrix}, \tag{S16}$$

where $\mathbf{L} = \mathbf{r} \times \mathbf{p}$ is the orbital momentum operator, $\boldsymbol{\sigma} = (\sigma_x, \sigma_y, \sigma_z)$ is the vector of Pauli operators, and Δ_{ASO} is the atomic spin-orbit coupling strength. Finally, due to the broken inversion symmetry at the interface along z, an additional coupling of the orbital d_{xy} to d_{yz} and d_{xz} appears, at the origin of the Rashba spin-orbit coupling. This effect can be accounted for via a third Hamiltonian of the form [S25, S26, S29, S30]

$$H_a = i\Delta_z a \begin{pmatrix} 0 & 0 & k_x \\ 0 & 0 & k_y \\ -k_x & -k_y & 0 \end{pmatrix} \otimes \mathbb{1}_2 \tag{S17}$$

where $a = 0.392$ nm is the lattice spacing and Δ_z the overall energy scale.

An effective Landé g factor can be obtained from the model above by diagonalizing H [Eq. (S14)] and fitting the difference between the minima of its two lowest energy bands by a linear function of B. The slope of the fit provides $g\mu_B$ with g the Landé factor appearing in the main text.

Figure S24 shows the ratio g/g_0 as a function of ΔE_y and ΔE_z for different values of Δ_{ASO} and Δ_z. For similar confinement along y and z (i.e., $\Delta E_y \approx \Delta E_z$), the ratio g/g_0 is reduced, which could explain why the Landé factor observed in the QPC is lower than typical values of g in standard $SrTiO_3$-based interfaces. The width of the region of parameters where this effect appears increases with atomic spin-orbit coupling strength Δ_{ASO}. Note nonetheless that for large broken symmetry inversion energy Δ_z compared to Δ_{ASO}, our model describes an enhanced ratio g/g_0 at small ΔE_y.

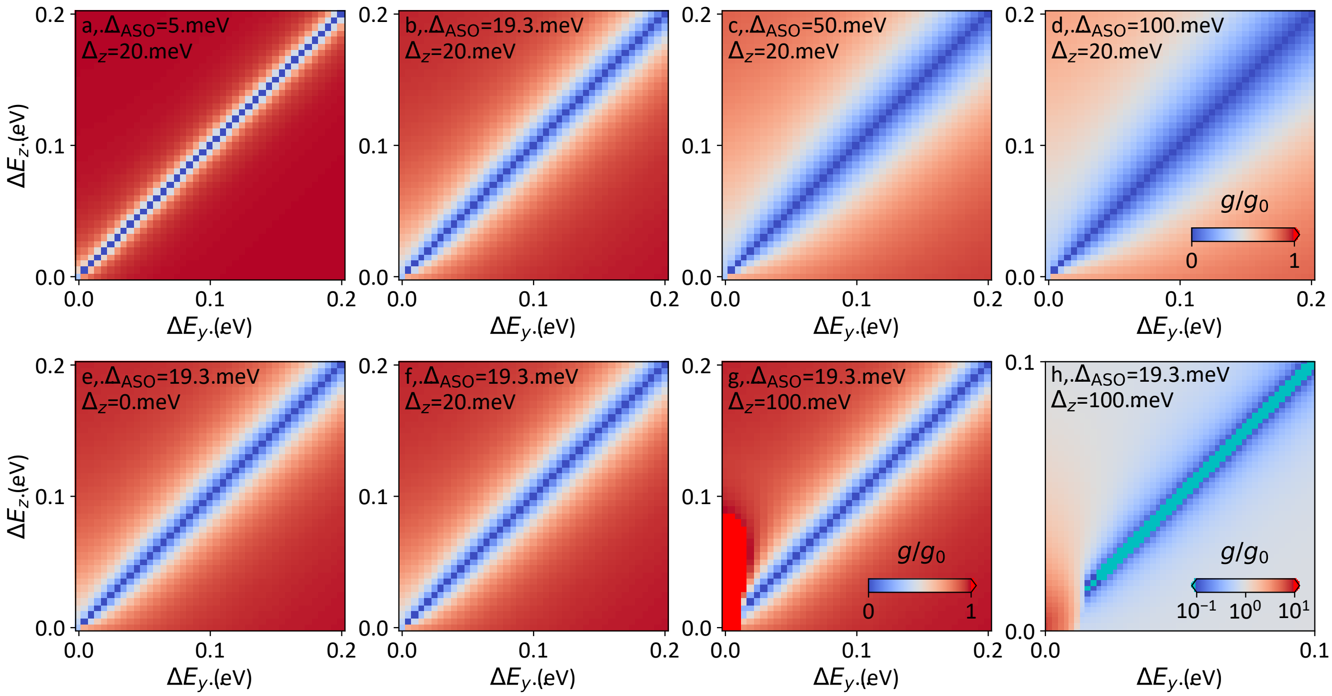

Fig. S24. Reduction of Zeeman splitting by confinement and spin-orbit-coupling. Ratio g/g_0 between the effective and initial Landé factors g and g_0 as a function of splitting energies ΔE_y and ΔE_z induced by the confinement along y and z, for different atomic spin-orbit coupling energy Δ_{ASO} and broken inversion symmetry energy Δ_z. Other parameters are $m_h = 6.8m_e$, $m_l = 0.41m_e$ with m_e the electron mass. For $\Delta E_y \approx \Delta E_z$, the ratio g/g_0 is drastically reduced. The width of the region of reduced g/g_0 increases with Δ_{ASO}. For $\Delta_z \gtrsim \Delta_{\mathrm{ASO}}$, a region of enhanced g/g_0 can be obtained at small ΔE_y.

E. Mean-field model for electron pairing

The 'Y' shape (locking of subbands) observed in the conductance and transconductance data could be explained as the result of attractive interactions between the electrons. We summarize here a minimal mean-field model presented in [S12, S13, S31] accounting for electron pairing without superconductivity, which has been used in the context of transport of electrons in 1D waveguide at the LAO/STO interface [S12, S13, S31] and in the main text to produce the mean-field model traces in Figures 4b and c.

For this purpose, we first assume that the electrons act as free particles along x, which amounts to neglect the weak potential along that direction. Although this is a 1D model, it provides a reasonable agreement with the experimental data for the QPC. The single-particle Hamiltonian of this model in Landau gauge $\mathbf{A} = (-By, 0, 0)$ reads

$$H^0_{\mathrm{1D}} = \frac{(p_x - eBy)^2}{2m_x} + \frac{p_y^2}{2m_y} + \frac{p_z^2}{2m_z} + V(y) + V(z) - \mu - g\frac{\mu_B}{2}B\sigma_z + \frac{(\alpha_v\sigma_y + \alpha_l\sigma_z)}{\hbar}(p_x - eBy). \tag{S18}$$

The first six terms describes the spin-degenerate kinetic and potential energies of the electrons with electron momentum operators p_i $(i = x, y, z)$, effective masses m_i, parabolic transverse confinement $V(y) = m_y\omega_y^2y^2/2$ and $V(z) = m_z\omega_z^2z^2/2$ with trapping frequencies ω_y and ω_z, and chemical potential μ. The next terms describe the lifting of the spin degeneracy via the Zeeman splitting energy and different forms of spin-orbit coupling (SOC) characterized by strengths α_v and α_l, modelling e.g. Rashba SOC at the $SrTiO_3$-based interface. Without SOC (i.e., $\alpha_v = \alpha_l = 0$), the Hamiltonian can be diagonalized in a basis of subbands $|n_y, n_z, \sigma\rangle$ where n_y, n_z are quantum numbers for transverse harmonic oscillator eigenstates with spin $\sigma = \downarrow, \uparrow$ and single-particle energies

$$\xi_{n_yn_z\sigma k} = \frac{\hbar^2k^2}{2m_x}\frac{\omega_y^2}{\Omega^2} + \hbar\Omega\left(n_y + \frac{1}{2}\right) + \hbar\omega_z\left(n_z + \frac{1}{2}\right) - \mu - s(\sigma)g\mu_B B, \tag{S19}$$

where k is electron wavevector along x, $\Omega = \sqrt{\omega_y^2 + \omega_c^2}$ the renormalized trapping frequency along y, $\omega_c = eB/\sqrt{m_xm_y}$ the cyclotron frequency and $s(\downarrow) = -1/2$ and $s(\uparrow) = 1/2$. The presence of SOC mixes the different electron spin species within a given transverse mode $|n_y, n_z\rangle$.

On top of the single-particle model above, we consider attractive interactions between electrons in subbands of opposite spins labelled as $\alpha = |n_y, n_z, \downarrow\rangle$ and $\beta = |n'_y, n'_z, \uparrow\rangle$. In second quantization and at the mean-field level our interaction Hamiltonian takes the form

$$H^{\mathrm{I}}_{\mathrm{1D}} = \sum_k\left[\sum_{\gamma=\alpha,\beta}\Sigma_\gamma c^\dagger_{\gamma k}c_{\gamma k} - \left(\chi c^\dagger_{\alpha k}c_{\beta k} + \mathrm{h.c.}\right) + (\Delta c^\dagger_{\alpha k}c^\dagger_{\beta -k} + \mathrm{h.c.})\right], \tag{S20}$$

where $c_{k\alpha}$ is the annihilation operator of an electron in the subband α with a wavevector k, and where Σ_γ, χ and Δ are the Hartree, Fock and Bogoliubov mean fields defined as

$$\Sigma_\gamma = \frac{U}{2\pi}\int_{-\infty}^{\infty}\langle c^\dagger_{\overline{\gamma}k}c_{\overline{\gamma}k}\rangle\,\mathrm{d}k, \qquad \chi = \frac{U}{2\pi}\int_{-\infty}^{\infty}\langle c^\dagger_{\alpha k}c_{\beta k}\rangle\,\mathrm{d}k, \qquad \Delta = \frac{U}{2\pi}\int_{-\infty}^{\infty}\langle c_{\beta k}c_{\alpha -k}\rangle\,\mathrm{d}k, \tag{S21}$$

where $\overline{\gamma}$ denotes the opposite subband of γ $(\gamma = \alpha, \beta)$ and where U is the interaction strength (in dimensions of energy $\times$ length). We consider that U has the following empirical scaling with the magnetic field

$$U \equiv U(B) = U_0\sqrt{1 - \frac{\omega_c^2}{\Omega^2}} = U_0\frac{\omega_y}{\Omega}, \tag{S22}$$

where U_0 is a bare interaction strength. This makes $|U|$ decreasing as a function of the magnetic field and the mean-fields (S21) independent of this effective scaling.

The total Hamiltonian $H_{\mathrm{1D}} = H^0_{\mathrm{1D}} + H^{\mathrm{I}}_{\mathrm{1D}}$ in second quantization reads

$$H_{\mathrm{1D}} = \sum_k\left[\sum_{\gamma=\alpha,\beta}\left(\xi_{\gamma k} + \Sigma_\gamma + 2s(\gamma)\frac{\omega_y^2}{\Omega^2}\alpha_l k\right)c^\dagger_{\gamma k}c_{\gamma k} + \left[\left(i\alpha_v\frac{\omega_y^2}{\Omega^2}k - \chi\right)c^\dagger_{\alpha k}c_{\beta k} + \mathrm{h.c.}\right] + \left(\Delta c^\dagger_{\alpha k}c^\dagger_{\beta -k} + \mathrm{h.c.}\right)\right]. \tag{S23}$$

and defines the following self-consistent eigenvalue problem in the electron and hole basis $\{c_{\alpha k}, c^\dagger_{\alpha -k}, c_{\beta k}, c^\dagger_{\beta -k}\}$

$$\begin{pmatrix} \xi_{\alpha k} + \Sigma_\alpha - \alpha_l\frac{\omega_y^2}{\Omega^2}k & 0 & i\alpha_v\frac{\omega_y^2}{\Omega^2}k - \chi & \Delta \\ 0 & -\xi_{\alpha k} - \Sigma_\alpha - \alpha_l\frac{\omega_y^2}{\Omega^2}k & -\Delta^* & -i\alpha_v\frac{\omega_y^2}{\Omega^2}k + \chi^* \\ -i\alpha_v\frac{\omega_y^2}{\Omega^2}k - \chi^* & -\Delta & \xi_{\beta k} + \Sigma_\beta + \alpha_l\frac{\omega_y^2}{\Omega^2}k & 0 \\ \Delta^* & i\alpha_v\frac{\omega_y^2}{\Omega^2}k + \chi & 0 & -\xi_{\beta k} - \Sigma_\beta + \alpha_l\frac{\omega_y^2}{\Omega^2}k \end{pmatrix}\phi_{jk} = E_{jk}\phi_{jk}, \tag{S24}$$

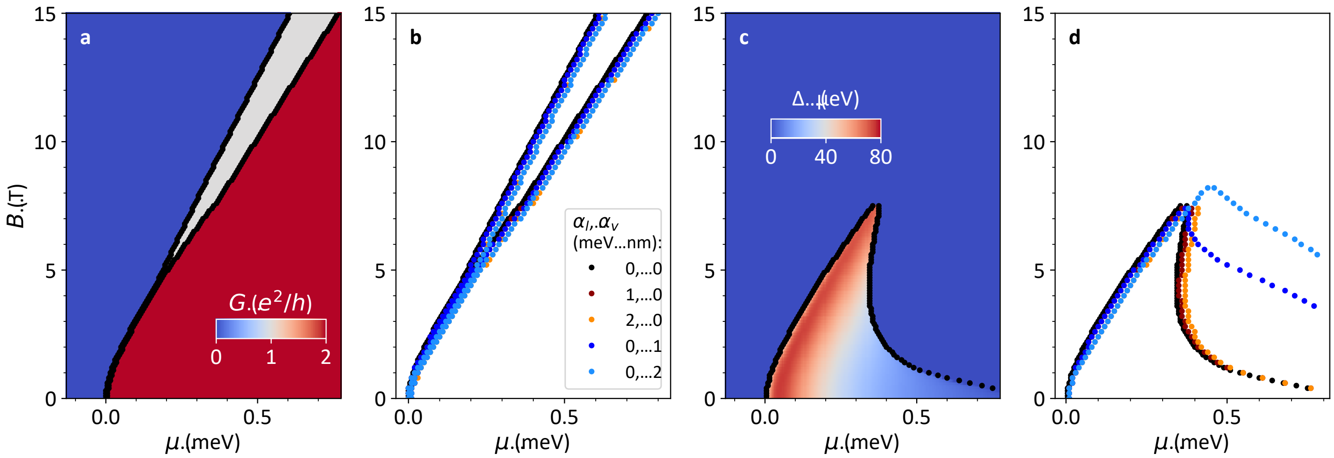

Fig. S25. Mean-field simulations. (a) Conductance as a function of μ and B and without spin-orbit coupling ($\alpha_v = \alpha_l = 0$). (b) Transconductance lines for different SOC strength α_v and α_l. (c) Pairing area (i.e., region where $|\Delta| > 2.6$ μeV) as a function of B and μ without spin-orbit coupling ($\alpha_v = \alpha_l = 0$). (d) Modifications of the contour of the pairing area due to SOC, with the same legend as in (b). All simulations were performed for $m_x = m_y = 1.124 m_e$, $g = 0.3$, $U_0 = -5.0$ meVnm, $\hbar\omega_y = 0.157$ meV, and $T = 30$ mK.

where E_{jk} and ϕ_{jk} ($j = 1, 2$) are the quasi-energies of the quasi-particle wave function solutions. Equation (S24) must be solved self-consistently, by inserting initial random values of Σ_γ, χ and Δ into Eq. (S24) to obtain E_{jk} and ϕ_{jk}, computing new mean fields via Eq. (S21) and repeating the procedure until convergence of the mean fields is reached (unless otherwise stated we run the self-consistent convergence procedure until the mean-fields are converged to within 10^{-6} meV). Note that their calculations require to use Bogoliubov transformations of the electrons operators $c_{\gamma k}$ ($\gamma = \alpha, \beta$) appearing in Eq. (S21) into quasi-particle operators γ_{jk} ($j = 1, 2$) satisfying

$$\langle \gamma_{ik}^\dagger \gamma_{jk} \rangle = \delta_{ij} n(E_{ik}), \qquad \langle \gamma_{ik} \gamma_{jk}^\dagger \rangle = \delta_{ij} [1 - n(E_{ik})], \qquad \langle \gamma_{ik} \gamma_{jk} \rangle = \langle \gamma_{ik}^\dagger \gamma_{jk}^\dagger \rangle = 0, \tag{S25}$$

where $n(E) = 1/[1 + e^{E/(k_B T)}]$ is the Fermi distribution with k_B the Boltzmann constant and T the temperature. Note also that since we work in the electron-hole basis twice as big as the physical basis, the quasi-energies E_{jk} appear in conjugate pairs $(E_{1k}, -E_{1-k})$ and $(E_{2k}, -E_{2-k})$ and one has to select only one member of each pair.

This mean-field model makes it possible to construct phase diagrams and associated conductance maps. We identify the presence of single-particle phases when the converged single-particle spectra cross the zero-energy axis, indicating the presence of electrons in the single-particle bands. Each non-zero positive Fermi momentum contributes e^2/h to the conductance G. By contrast, we identify the presence of a pair phase when $|\Delta| \gtrsim k_B T$ emerges from the calculations (i.e., when the single-particle spectra are gapped), indicating the presence of electron pairs. Since we consider that the pairs unbind when they reach the leads before dissipating energy [S32], we associate a conductance of $2e^2/h$ to the pair phase, i.e., the sum of the conductances of the individual electrons.

Figure S25 shows the results of the mean-field model for the two lowest subbands $|0, 0, \downarrow\rangle$ and $|0, 0, \uparrow\rangle$ with parameters $m_x = m_y = 1.124 m_e$, $g = 0.3$, $U_0 = -5.0$ meVnm, $\hbar\omega_y = 0.157$ meV, and $T = 30$ mK throughout all simulations. Since the confinement along z only contributes a constant energy shift to the Hamiltonian, Eq.(S19), we ignored this in the simulations, and used $\hbar\omega_z = 0.0$ meV for simplicity. Panel (a) shows the conductance as a function of μ and B without spin-orbit coupling ($\alpha_v = \alpha_l = 0$). Due to the presence of the attractive interactions, the electrons in the two first subbands are paired at low B up to some critical field B_P. Below B_P, this leads to a conductance step of $2e^2/h$ as μ is increased. Above B_P the Zeeman term dominates over the pairing strength, the pairs unbind, and we observe two distinguishable conductance steps of e^2/h. The inclusion of SOC effects can reshape conductance steps [S13, S33], but as shown in panel (b), inclusion of either non-zero α_v or α_l only negligibly modifies the transconductance lines. This suggests that SOC can be safely neglected for the understanding of the transport data. We chose reasonable values of SOC up to 2 meVnm, motivated by the fact that whilst typical values of Rashba SOC in STO-based interfaces can be of the order of 1-5 meV nm [S34, S35], a recent study suggests that it can be strongly reduced due to confinement [S13]. Panel (c) shows the pairing area as a function of μ and B, and (d) how it is modified when including SOC with $\alpha_v \neq 0$. It can be seen, that the SOC does increase the pairing area to larger μ, but since the paired phase is indistinguishable from the phase where both single-particle bands are occupied (from a conductance perspective), this effect cannot be observed in the present experimental conductance data.

S3. QPC PLATEAU STABILITY AND FRACTIONAL STRUCTURES

In this section, extensive supplementary data are presented on stability of the subband plateau structure. It is tested at zero DC bias, in the multi-dimensional phase space defined by V_{GIL} (acting similarly to a back gate voltage), and asymmetrically sweeping split gate voltages V_{G1} and V_{G2}. We find the plateau structure originating from $|n_y = 0, n_z \geq 0, s = \pm 1/2\rangle$ subbands to be largely stable to such perturbations at B above a few Tesla. Near $B = 0$, the plateau structure can be highly unstable and present fractional transitions between conductance values that are non-integer multiples of the spin-polarized conductance quantum e^2/h.

Fig. S26 presents the case of a stable plateau structure, of which the clearest examples were found for $|0, n_z \geq 0, \pm 1/2\rangle$ subbands that are disentangled by B from $|1, 0, \pm 1/2\rangle$ and the underlying subband "forest". This is the case for the first three plateaus shown in Fig. S26a-f, at $B = 5$ T for the 4.6×10^{13} cm^{-2} cooldown. The $G(V_{\mathrm{G2}}, V_{\mathrm{G1}})$ map shows an approximately equal modulation by each split gate, confirming similarity of their capacitance and lever arm. Subbands can be identified in line traces as midpoints of transitions between flat regions in G. In the parametric plot of $dG/V_{\mathrm{G2}}(G, V_{\mathrm{G1}})$, narrow dark blue regions near integer multiples of e^2/h correspond to flat plateaus in G, while extended bright regions correspond to sharp transitions at subband filling. Plateau locations in G (especially at higher filling) are slightly lower than integer multiples of e^2/h, which is consistent with the presence of a series resistance between the constriction and the voltage probes. In Fig. S26a-c, the first three plateaus remain stable when G is tuned by V_{G2}, while V_{G1} is swept independently. Similarly, the same plateaus in Fig. S26d-f are stable when G is tuned by $V_{\mathrm{G2}} = V_{\mathrm{G1}} = V_{\mathrm{G12}}$ while V_{GIL} is swept independently. For $G > 6e^2/h$, apparent higher order degeneracies are created by overlap with $n_y > 0$ subbands (see extensive discussion in previous sections S2 B and S2 C). The resulting plateau structure is also largely stable. A switch in Fig. S26f of the plateau value between 14 and 16 e^2/h is consistent with a change of subband order from slight rearrangement of z and/or y confinement by V_{GIL}.

Broadly similar phenomenology is observed at $B = 5$ T for the 3.0×10^{13} cm^{-2} cooldown and at $B = 14$ T for both 3.0 and 4.6×10^{13} cm^{-2} cooldowns (Fig. S26 and S27). At $B = 14$ T, Zeeman splitting results in appearance of plateaus at odd multiples of e^2/h, although at high filling the subbands still appear doubly degenerate due to increased B_{P} of order 14 T (see previous section S2 C, Fig. S13 and S17). At lower filling, gate-driven switches in plateau degeneracy are observed. This is consistent with overlap between adjacent Zeeman split bands (see Fig. S26g-l, S27j-l), combined with alteration of the confinement potential by the gates.

The opposite case of an unstable plateau structure is most clearly apparent near $B = 0$, particularly for the 3.0×10^{13} cm^{-2} cooldown (Fig. S28). The parametric transconductance plots present a rich structure that rapidly shifts with assymetrically swept V_{G1} and V_{GIL} and with B. Only a few features can be tentatively assigned to an integer multiple of the conductance quantum (e.g. several spots with low dG/dV_{G2} at $G = 4$ and 8 e^2/h). Otherwise, the position of most features gradually evolves through fractional values of G. This is inconsistent with the basic expectations of conduction via discrete ballistic subbands. However, DC bias spectroscopy in this regime (see section S2 A and Fig. S7e) does yield a subband-like diamond pattern, even in absence of expected quantization in G. Particularly noteworthy are the gradual fractional features near pinch off, where the small value of G minimizes uncertainty from finite series resistance. In Fig. S28c, the first plateau moves position between $G = 2e^2/h$ and $0.5e^2/h$. The latter small value of G corresponds to half of a spin-polarized ballistic mode, clearly unexpected at $B = 0$.

For the 4.6×10^{13} cm^{-2} cooldown (Fig. S29), the plateau structure at $B = 0$ has similarities in showing rapid shifts in V_{G1} and V_{GIL}, but also much less tendency for gradual movement of subband-like transitions through obviously fractional values. This is also consistent with the overall reduced repeatable noise in the transconductance signal for this cooldown for the entire B range. In the 3.0×10^{13} cm^{-2} cooldown, the stable integer plateau structure at $B = 5$ and 14 T appears overlayed with repeatable noise, likely a residual of the behavior that dominates near $B = 0$.

We do not have a crisp explanation for the physics of the unstable plateau regime, but several factors are likely to be relevant here:

- Interplay of y and z confinement, producing closely spaced subbands. Gradual tuning of the confinement potentials by V_{G1}, V_{G2} and V_{GIL} does produce detectable shifts in band order at higher B, and is likely even more relevant for subband structure at $B = 0$. This cannot explain fractional values of G and the gradual transitions between them, only the presence of rapid evolution in the (V_{G1}, V_{G2}, V_{GIL}) phase space.

- Various disorder-related mechanisms can be put forward as a conventional explanation. For instance, tuning of disorder potential in InAs-based QPC's has been shown to produce gradual transitions between non-integer conductance plateaus [S36]. It was related to the disruption of the assumption that the coupling between the constriction and the adjacent electron reservoirs is adiabatic [S36]. Alternatively, an accidental Coulomb blockade in the vicinity of the constriction could produce resonant features that resemble short plateaus at any value of G.

- Alternatively, quantization anomalies can be connected to electron interactions. This is a rich and still largely unresolved research direction in GaAs-based QPC's (see e.g. [S37]). For instance, in [S38] fractional quantization phenomenology (resembling some aspects of our device) was explained in terms of spin-incoherent transport arising from Luttinger liquid physics.

At this point we do not attempt to disentangle these explanations. Future attempts to do so would strongly benefit from reducing broadening by the longitudinal potential (i.e. making the constriction longer and wire-like), since it dominates the $B = 0$ behavior in our current device.

For completeness, constriction conductance in the $10.4{\times}10^{13}$ cm^{-2} (largest studied) cooldown is shown in Fig. S30. Gate voltages V_{GIL} and V_{G12} can modulate G in the 220-420 e^2/h range. But constriction pinch-off could not be reached within the safely available range of gate voltages.

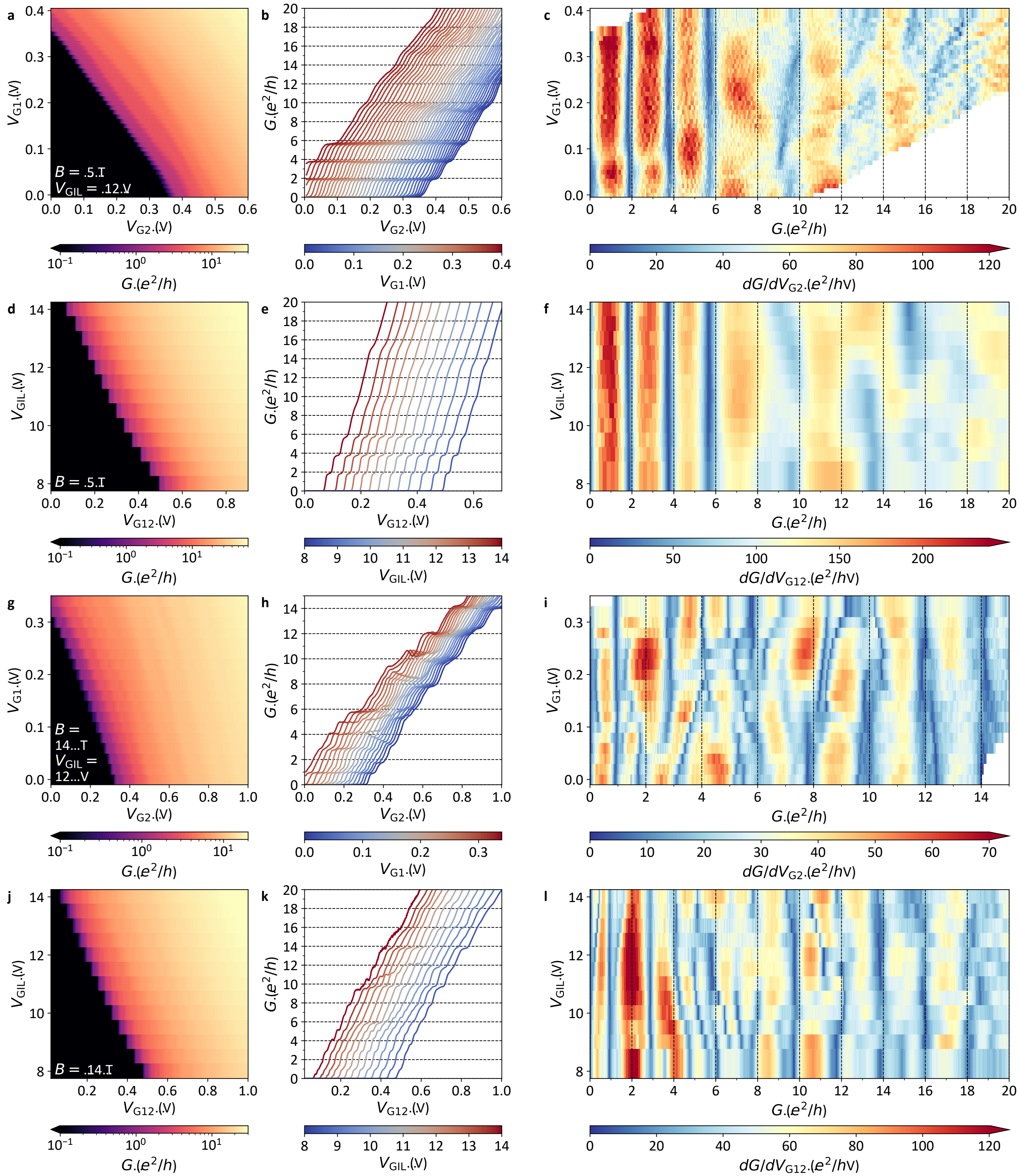

Fig. S26. Stable integer plateau structures, 4.6×10^{13} cm^{-2} cooldown. (Left) Constriction conductance map, (center) conductance line cuts in fast gate voltage axis, (right) parametric plot of transconductance against conductance and slow gate voltage axis. (a-c) $B = 5$ T, $V_{\mathrm{GIL}} = 12$ V, V_{G1}-V_{G2} map. (d-f) $B = 5$ T, V_{GIL}-V_{G12} map. (g-i) $B = 14$ T, $V_{\mathrm{GIL}} = 12$ V, V_{G1}-V_{G2} map. (j-l) $B = 14$ T, V_{GIL}-V_{G12} map.

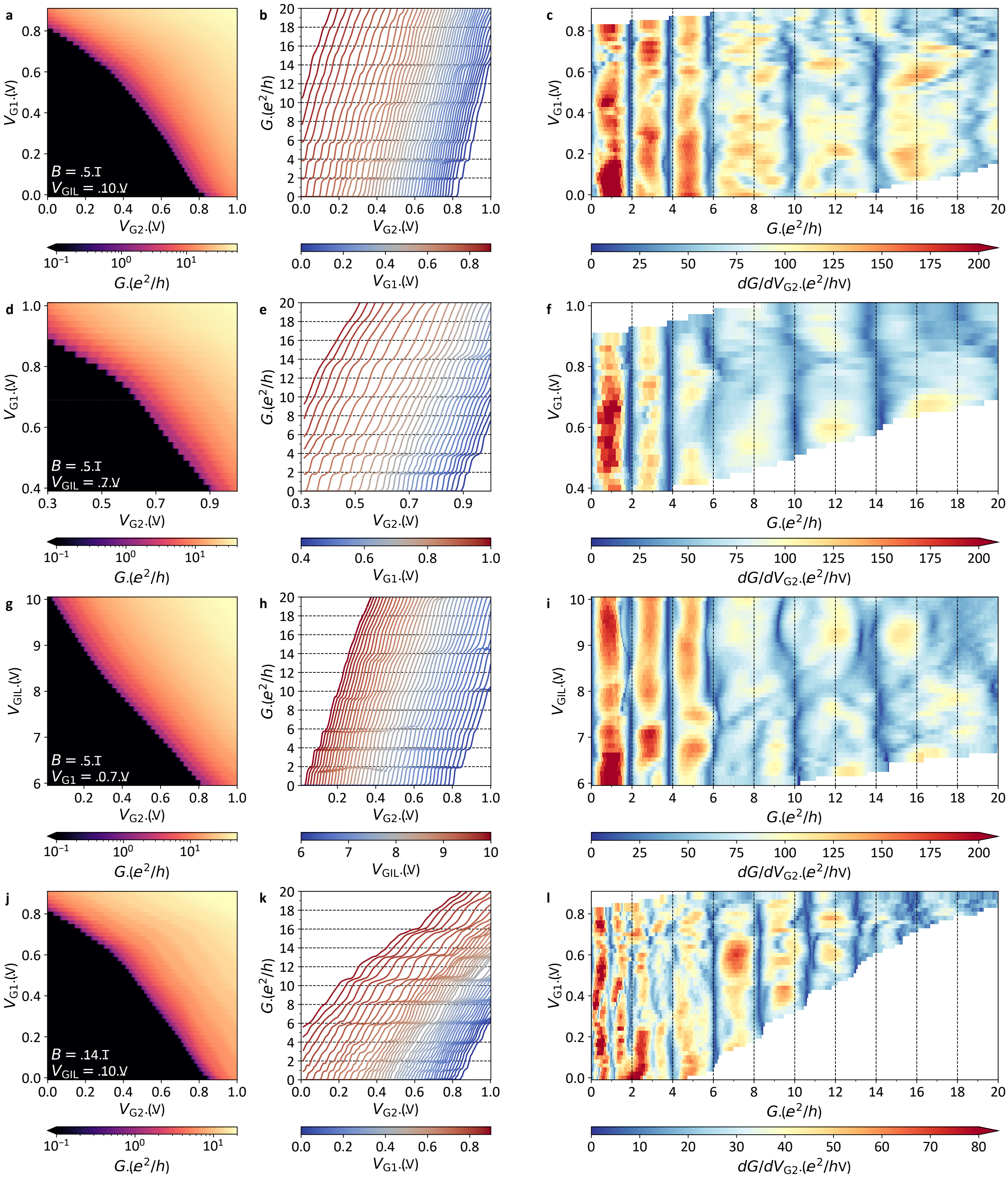

Fig. S27. Stable integer plateau structures, 3.0×10^{13} **cm^{-2} cooldown.** (Left) Constriction conductance map, (center) conductance line cuts in fast gate voltage axis, (right) parametric plot of transconductance against conductance and slow gate voltage axis. (a-c) $B = 5$ T, $V_{\mathrm{GIL}} = 10$ V, V_{G1}-V_{G2} map. (d-f) $B = 5$ T, $V_{\mathrm{GIL}} = 7$ V, V_{G1}-V_{G2} map. (g-i) $B = 5$ T, $V_{\mathrm{G1}} = 0.7$ V, V_{GIL}-V_{G2} map. (j-l) $B = 14$ T, $V_{\mathrm{GIL}} = 10$ V, V_{G1}-V_{G2} map.

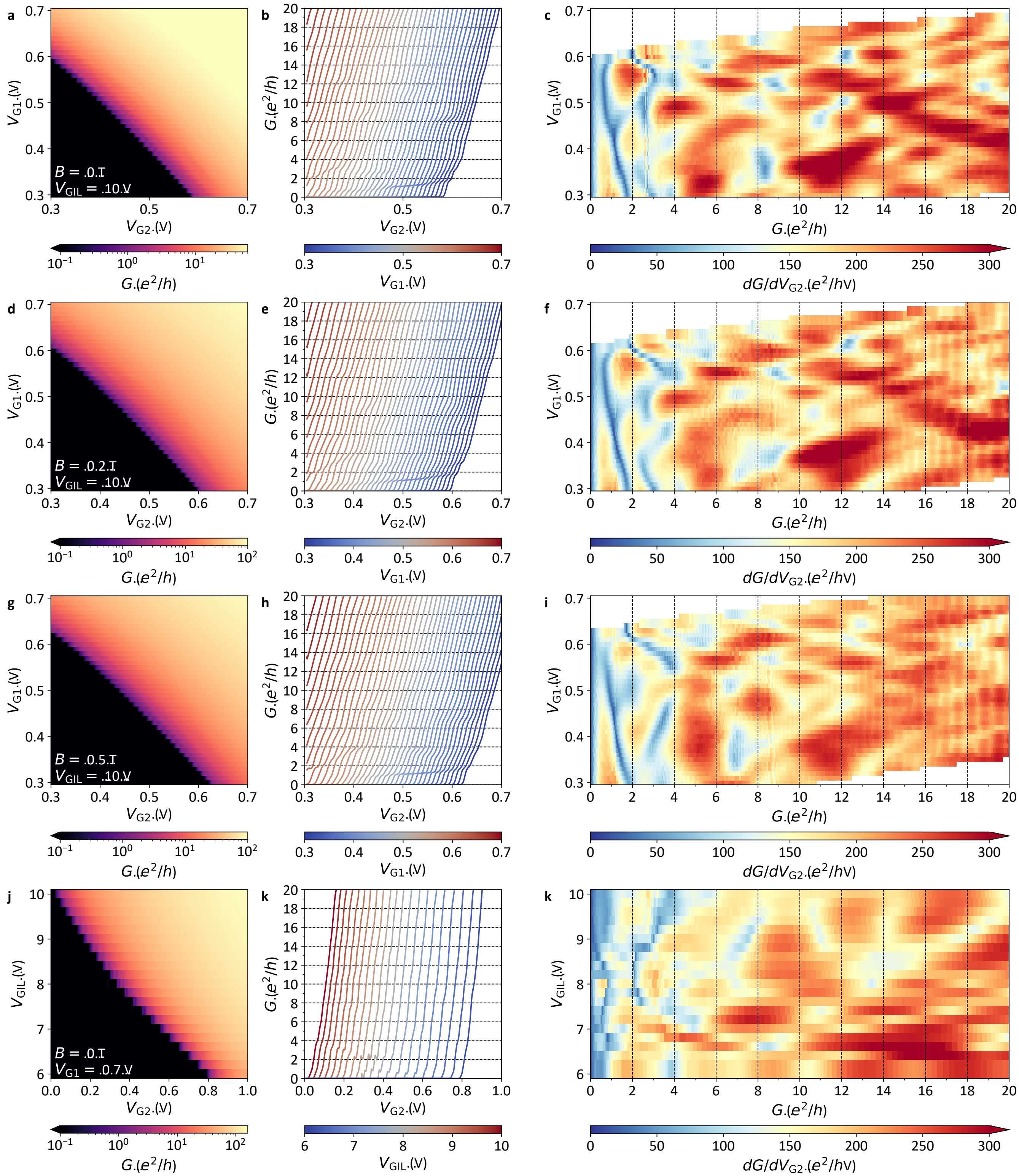

Fig. S28. Unstable, incoherent plateau structures, 3.0×10^{13} $\mathbf{cm^{-2}}$ **cooldown.** (Left) Constriction conductance map, (center) conductance line cuts in fast gate voltage axis, (right) parametric plot of transconductance against conductance and slow gate voltage axis. $B = 0$ T (a-c), 0.2 T (d-f), 0.5 T (g-i), $V_{\mathrm{GIL}} = 10$ V, V_{G1}-V_{G2} map. (j-l) $B = 0$ T, $V_{\mathrm{G1}} = 0.7$ V, V_{GIL}-V_{G2} map

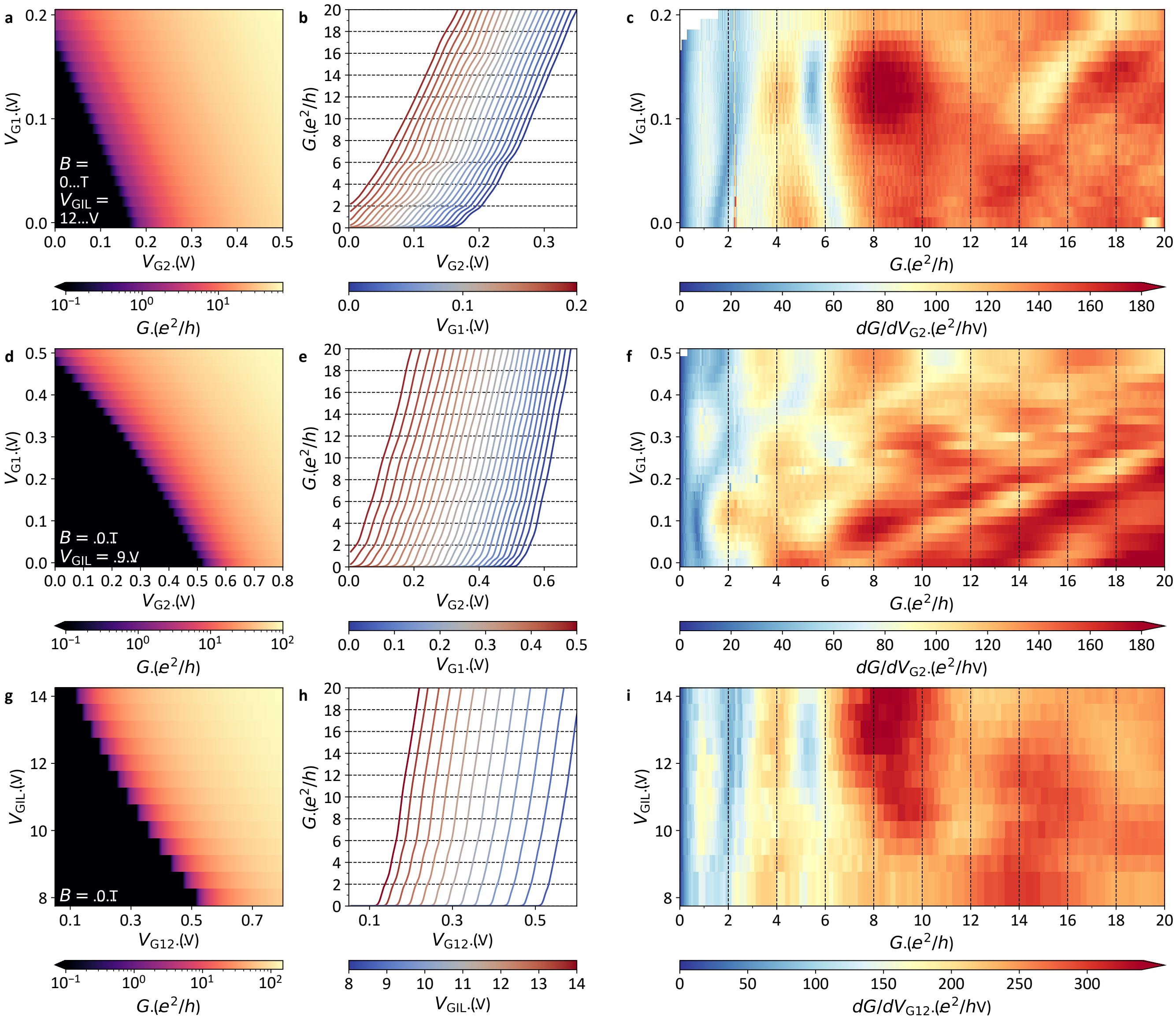

Fig. S29. Zero field plateau structures, 4.6×10^{13} cm^{-2} cooldown. (Left) Constriction conductance map, (center) conductance line cuts in fast gate voltage axis, (right) parametric plot of transconductance against conductance and slow gate voltage axis. $B = 0$ T, (a-c) $V_{\mathrm{GIL}} = 12$ V, V_{G1}-V_{G2} map. (d-f) $V_{\mathrm{GIL}} = 9$ V, V_{G1}-V_{G2} map. (g-i) V_{GIL}-V_{G12} map.

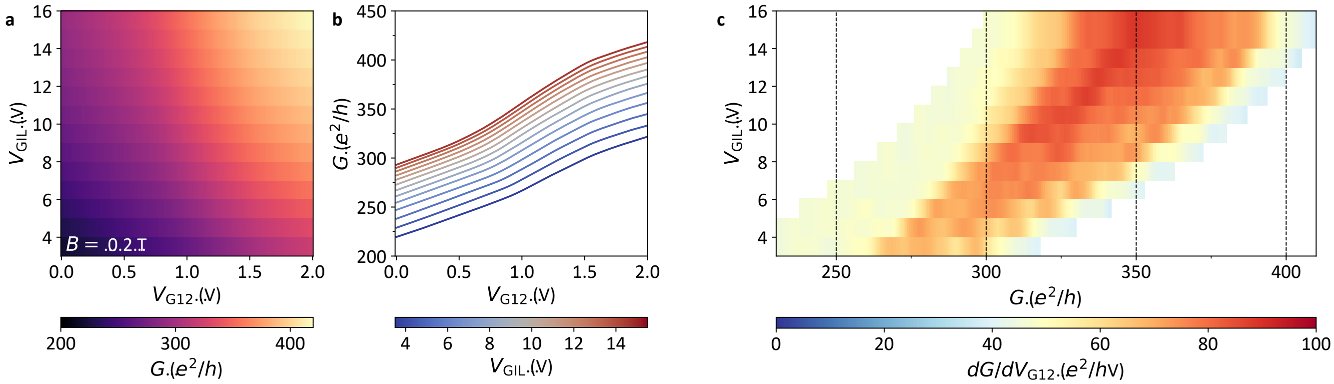

Fig. S30. An open constriction at high carrier density. 10.4×10^{13} cm^{-2} cooldown, $B = 0.2$ T. (a) Constriction conductance map with V_{GIL} and V_{G12}, (b) conductance line cuts in V_{G12}, (c) parametric plot of transconductance against conductance and V_{GIL}.

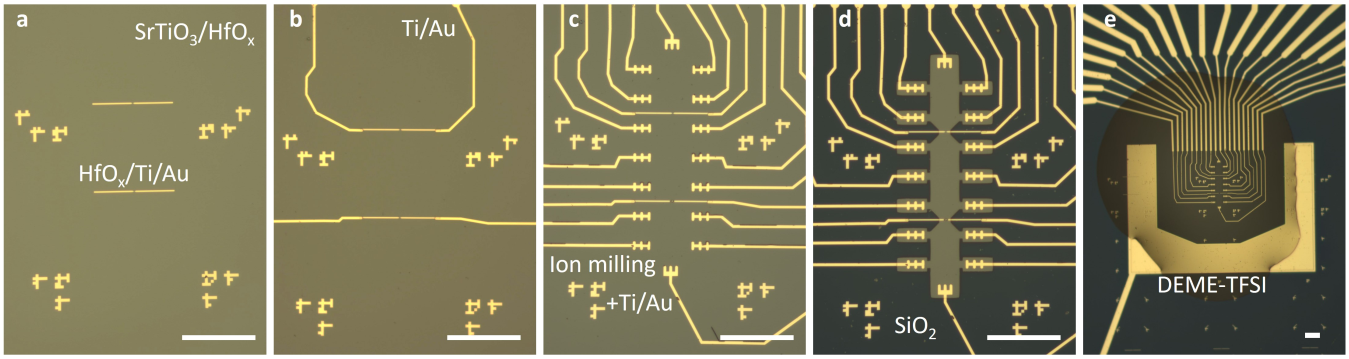

Fig. S31. Main device fabrication. Optical images after lift-off of (a) split gates, (b) gate contacts, (c) ohmic contacts, (d) mesa insulation. (e) Finished device with ionic liquid. All scale bars are 50 μm.

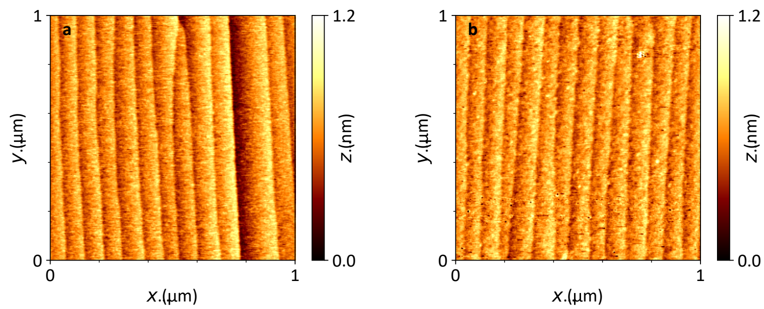

Fig. S32. $SrTiO_3$ and $SrTiO_3/HfO_x$ surface. Atomic force microscopy images of (a) $SrTiO_3$ substrate after TiO_2-terminated surface preparation, (b) same chip after 10 HfO_x ALD deposition cycles.

S4. FABRICATION DETAILS AND ADDITIONAL DEVICES

This section complements the methods section in the main text. Additionally, selected data are presented for additional $SrTiO_3/HfO_x$ Hall bar devices with and without split gates.

Fig. S31 shows optical images of the main studied device at different stages of fabrication of the main device. Small area images of the Hall bar region are shown after each of the four lithography steps, as described in the main text. A large area image is also shown of the device with the ionic liquid deposited, shortly prior to loading into the dilution refrigerator.

Additionally, Fig. S32 shows a comparison of atomic force microscopy images taken on the same $SrTiO_3$ chip before and after deposition of a blanket HfO_x barrier layer. The number of ALD cycles used for depositing HfO_x was 10 in this case, i.e. thicker than 4 cycles used for the main measured device. We do not observe any appreciable change in the terrace step morphology or surface roughness, consistent with a highly conformal and smooth ALD deposition on $SrTiO_3$.

A. Additional Hall bar devices

As part of fabrication flow and device geometry iteration, a total of 9 simplified Hall bar devices were fabricated and rapidly tested in a cryostat with a 1.6 K base temperature. These devices followed the same general fabrication flow as the main constriction device, but skipping two lithography steps for gate and gate contact fabrication. A TiO_2-terminated $SrTiO_3$ crystal was coated with sub-nm thick HfO_x, using 3-10 cycles of atomic layer deposition (85° C in all devices presented below). E-beam lithography step 1 was followed by ion milling, deposition of Ti/Au ohmic contact, and lit-off. E-beam lithography step 2 was followed by sputtering of SiO_2 insulation and lift-off..

Fig. S33 shows optical images of 3 devices with different Hall bar geometry and HfO_x target thickness. Device A: 5-30 μm wide channels, 3 HfO_x ALD cycles. Device B: 40 μm wide channel, 5 HfO_x ALD cycles. Device C: 5, 10, and 20 μm wide channels, 4 HfO_x ALD cycles. These devices were fabricated in separate processing runs. Device C was fabricated in the same run as the main device with split gates.

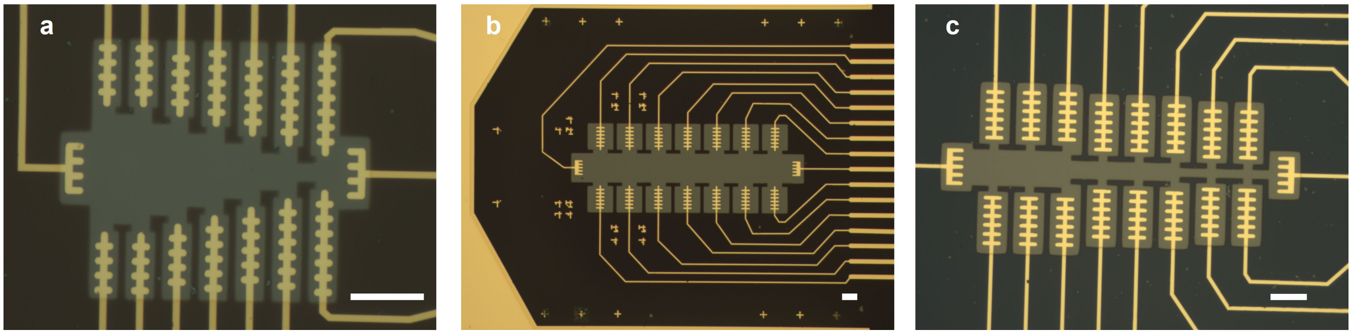

Fig. S33. Optical images of additional devices. (a) device A, (b) B, (c) C. Estimated HfO_x barrier thickness in (a,b,c) was 0.45, 0.75, 0.6 nm (3, 5, 4 ALD cycles), respectively. Scale bars are 20 μm.

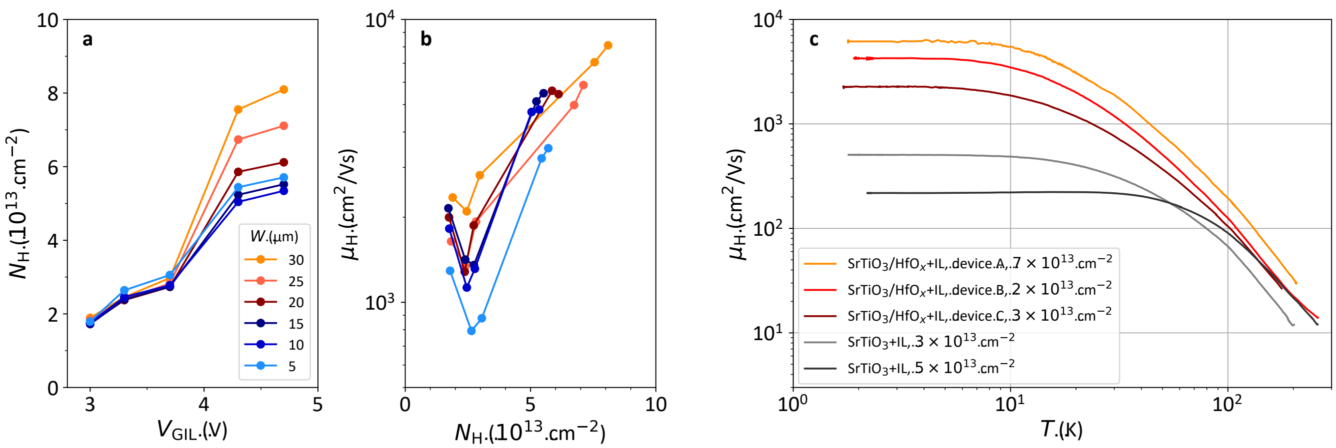

Fig. S34. High mobility 2DEGs in additional devices. Device A: (a) Hall density at 1.6 K, tun by $V_{\rm GIL}$ above 220 K, (b) corresponding Hall mobility. Different traces are for different channel widths along the device. (c) Temperature dependence of Hall mobility in devices A, B, C and in typical devices without a barrier layer. Devices labeled in order of low temperature mobility.

Typical transport characterization involved accumulation of a 2DEG near 265 K, followed by alternation between Hall measurements at 1.6 K base temperature, thermal cycling up to $\approx$ 200 K to measure temperature dependence of the 4-terminal resistance, and thermal cycling up to $\approx$ 250 K to adjust $V_{\rm GIL}$ and the 2DEG carrier density. Below 220K, $V_{\rm GIL}$ was typically adjusted a few volts above its high temperature value to decrease ohmic contact resistance and marginally optimize mobility. Carrier density shown in Fig. S34 was determined by a linear fit to the Hall slope at 1.6 K, neglecting non-linearity of the Hall coefficient in B (typically 10-20% in our devices). The temperature-dependent Hall mobility $\mu_{\rm H}$ was calculated as $\mu_{\rm H}(T) = (eN(1.6\ {\rm K})R(T))^{-1}$, i.e. a T-independent carrier density is assumed.

Fig. S33a,b shows an example of systematic carrier density tuning in the 2-8$\times 10^{13}$ cm^{-2} range (measured at 1.6 K) by adjusting $V_{\rm GIL}$ above 220 K. Gradual non-uniformity of measured Hall density over tens of microns was usually present, especially in larger devices. The density shown for each Hall bar region was taken to be an average between the two adjacent pairs of Hall contacts. The Hall mobility in optimized conditions typically reached several thousands of cm^2/Vs (see Fig. S34b,c). The general trend of increasing $\mu_{\rm H}$ at high $N_{\rm H}$ was common in studied devices.

Between 1.6K and near room temperatures, metallic behavior was observed for carrier densities that were high enough to get reliable ohmic contacts (usually above $\approx 10^{13}$ cm^{-2}). Extrapolated mobility at room temperature was always close to 10 cm^2/Vs, as typical for electron-doped $SrTiO_3$ [S39]. Typical traces for $SrTiO_3$ Hall bar devices without HfO_x barrier layers are also shown for comparison in Fig. S34c. Such devices have mobilities of order 100-1000 cm^2/Vs at base temperature, see also [S1, S40, S41]. Comparison of temperature dependence also showcases the much larger residual resistivity ratio in high mobility $SrTiO_3/HfO_x$ devices (up to $\approx$ 500).

Consequently, despite significant statistical scatter between devices, the insertion of a thin HfO_x barrier layer consistently improves Hall mobility from 10^2-10^3 cm^2/Vs into the 10^3-10^4 cm^2/Vs range. Correspondingly, the mean free path is improved from tens of nm into the range of hundreds of nm to a few microns.

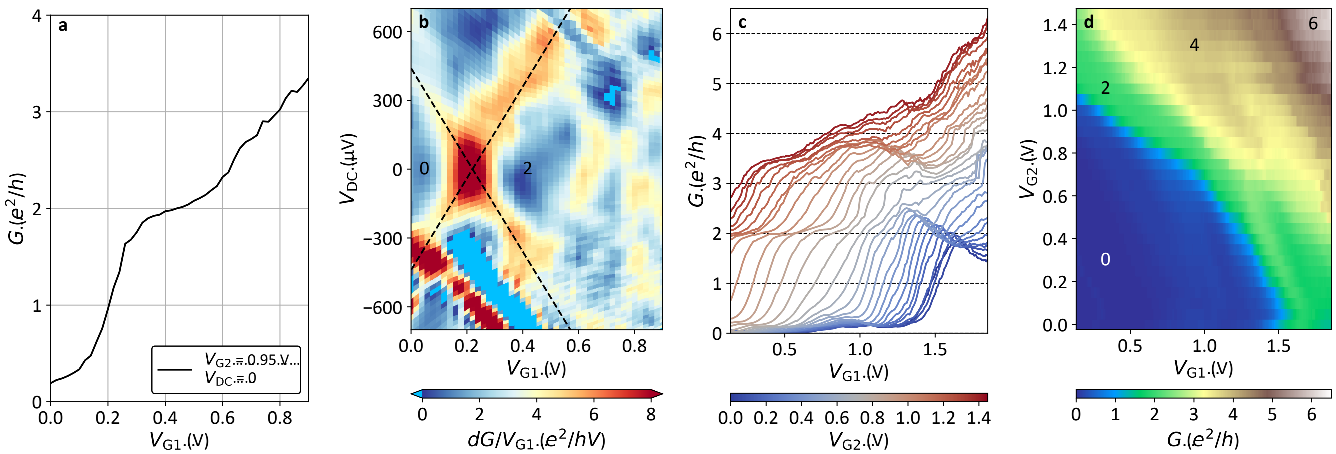

Fig. S35. Second constriction device. (a) Zero bias conductance tuned by V_{G1}. (b) Map of transconductance with DC bias and V_{G1}. (c, d) Zero bias conductance at zero DC bias with the two split gate voltages (V_{G1} and V_{G2}) tuned separately. Temperature is 440 mK and $B = 0$ T in (a-c). V_{G2} is fixed at 0.95 V in (a) and (b).

B. Additional device with split gates

In this section we show data from a second device that includes nanopatterned split gates. The layout design and fabrication procedures are identical to the main device described in this work. The second device was fabricated on a separate $SrTiO_3$ chip with one intentional difference: the barrier layer thickness was reduced from 4 to 3 HfO_x ALD deposition cycles.

In the coarsely patterned 2DEG at base temperature (34 mK), we measured a carrier density of 4.7×10^{13} cm^{-2} and a mobility of 4800 cm^2/Vs (540 nm mean free path).

Fig. S35 shows split-gate tuning of a 40-nm constriction near a single ballistic mode. Various spurious features are readily seen in the data, including likely accidental Coulomb blockade resonances. But by fine tuning the constriction away from such features in the V_{G1}-V_{G2} space, the $G = 2e^2/h$ plateau can be observed at zero DC bias (Fig. S35a). In finite DC bias, a crossing between the corresponding left and right-moving subbands is resolved in the transconductance map (dashed lines in Fig. S35b). In the full V_{G1}-V_{G2} map at zero bias (Fig. S35c and d), the $G = 2e^2/h$ plateau is not spurious. It persists in the $V_{\mathrm{G2}} = 0.8$-1.2 V range with V_{G1} as the fast axis.

SUPPLEMENTARY REFERENCES

[S1] E. Mikheev, I. T. Rosen, and D. Goldhaber-Gordon, Quantized critical supercurrent in $SrTiO_3$-based quantum point contacts, Science Advances **7**, eabi6520 (2021).
[S2] K. A. Müller and H. Burkard, $SrTiO_3$: An intrinsic quantum paraelectric below 4 K, Physical Review B **19**, 3593 (1979).
[S3] Z. Chen, H. Yuan, Y. Xie, D. Lu, H. Inoue, Y. Hikita, C. Bell, and H. Y. Hwang, Dual-gate modulation of carrier density and disorder in an oxide two-dimensional electron system, Nano Letters **16**, 6130 (2016).
[S4] J. Biscaras, S. Hurand, C. Feuillet-Palma, A. Rastogi, R. Budhani, N. Reyren, E. Lesne, J. Lesueur, and N. Bergeal, Limit of the electrostatic doping in two-dimensional electron gases of $\mathrm{La}X\mathrm{O}_3(X = \mathrm{Al, Ti})/\mathrm{SrTiO}_3$, Scientific Reports **4**, 6788 (2014).
[S5] M. B. Shalom, M. Sachs, D. Rakhmilevitch, A. Palevski, and Y. Dagan, Tuning spin-orbit coupling and superconductivity at the $SrTiO_3/LaAlO_3$ interface: a magnetotransport study, Physical Review Letters **104**, 126802 (2010).
[S6] P. Gallagher, M. Lee, T. A. Petach, S. W. Stanwyck, J. R. Williams, K. Watanabe, T. Taniguchi, and D. Goldhaber-Gordon, A high-mobility electronic system at an electrolyte-gated oxide surface, Nature Communications **6**, 6437 (2015).
[S7] D. W. Reagor and V. Y. Butko, Highly conductive nanolayers on strontium titanate produced by preferential ion-beam etching, Nature Materials **4**, 593 (2005).
[S8] A. Joshua, S. Pecker, J. Ruhman, E. Altman, and S. Ilani, A universal critical density underlying the physics of electrons at the $LaAlO_3/SrTiO_3$ interface, Nature Communications **3**, 1129 (2012).
[S9] A. Jouan, S. Hurand, G. Singh, E. Lesne, A. Barthélémy, M. Bibes, C. Ulysse, G. Saiz, C. Feuillet-Palma, J. Lesueur, and N. Bergeal, Origin of the dome–shaped superconducting phase diagram in $SrTiO_3$–based interfaces, arXiv:2104.08220 (2021).
[S10] B. Jalan, S. Stemmer, S. Mack, and S. J. Allen, Two-dimensional electron gas in δ-doped $SrTiO_3$, Physical Review B **82**, 081103 (2010).
[S11] F. Trier, G. E. D. K. Prawiroatmodjo, Z. Zhong, D. V. Christensen, M. von Soosten, A. Bhowmik, J. M. G. Lastra, Y. Chen, T. S. Jespersen, and N. Pryds, Quantization of Hall Resistance at the Metallic Interface between an Oxide Insulator and $SrTiO_3$, Physical Review Letters **117**, 096804 (2016).
[S12] A. Annadi, G. Cheng, H. Lee, J.-W. Lee, S. Lu, A. Tylan-Tyler, M. Briggeman, M. Tomczyk, M. Huang, D. Pekker, C.-B. Eom, and J. Irvin, P.and Levy, Quantized ballistic transport of electrons and electron pairs in $LaAlO_3/SrTiO_3$ nanowires, Nano Letters **18**, 4473 (2018).
[S13] F. Damanet, E. Mansfield, M. Briggeman, P. Irvin, J. Levy, and A. J. Daley, Spin-orbit-assisted electron pairing in one-dimensional waveguides, Physical Review B **104**, 125103 (2021).
[S14] A. P. Kajdos, D. G. Ouellette, T. A. Cain, and S. Stemmer, Two-dimensional electron gas in a modulation-doped $SrTiO_3/Sr(Ti,Zr)O_3$ heterostructure, Applied Physics Letters **103**, 082120 (2013).
[S15] A. McCollam, S. Wenderich, M. Kruize, V. K. Guduru, H. J. A. Molegraaf, M. Huijben, G. Koster, D. H. A. Blank, G. Rijnders, A. Brinkman, H. Hilgenkamp, U. Zeitler, and J. C. Maan, Quantum oscillations and subband properties of the two-dimensional electron gas at the $LaAlO_3/SrTiO_3$ interface, APL Materials **2**, 022102 (2014).
[S16] A. Fête, S. Gariglio, C. Berthod, D. Li, D. Stornaiuolo, M. Gabay, and J.-M. Triscone, Large modulation of the Shubnikov–de Haas oscillations by the Rashba interaction at the $LaAlO_3/SrTiO_3$ interface, New Journal of Physics **16**, 112002 (2014).
[S17] S. Suzuki, T. Yamamoto, H. Suzuki, K. Kawaguchi, K. Takahashi, and Y. Yoshisato, Fabrication and characterization of $Ba_{1-x}K_xBiO_3$/Nb-doped $SrTiO_3$ all-oxide-type Schottky junctions, Journal of Applied Physics **81**, 6830 (1997).
[S18] F. Nichele, S. Chesi, S. Hennel, A. Wittmann, C. Gerl, W. Wegscheider, D. Loss, T. Ihn, and K. Ensslin, Characterization of spin-orbit interactions of GaAs heavy holes using a quantum point contact, Physical Review Letters **113**, 046801 (2014).
[S19] A. Scherbakov, E. Bogachek, and U. Landman, Quantum electronic transport through three-dimensional microconstrictions with variable shapes, Physical Review B **53**, 4054 (1996).
[S20] M. Büttiker, Quantized transmission of a saddle-point constriction, Physical Review B **41**, 7906 (1990).
[S21] M. Briggeman, M. Tomczyk, B. Tian, H. Lee, J.-W. Lee, Y. He, A. Tylan-Tyler, M. Huang, C.-B. Eom, D. Pekker, R. S. K. Mong, P. Irvin, and J. Levy, Pascal conductance series in ballistic one-dimensional $LaAlO_3/SrTiO_3$ channels, Science **367**, 769 (2020).
[S22] S. Baer, C. Rössler, E. C. de Wiljes, P.-L. Ardelt, T. Ihn, K. Ensslin, C. Reichl, and W. Wegscheider, Interplay of fractional quantum Hall states and localization in quantum point contacts, Physical Review B **89**, 085424 (2014).
[S23] G. Khalsa and A. H. MacDonald, Theory of the $SrTiO_3$ surface state two-dimensional electron gas, Physical Review B **86**, 125121 (2012).
[S24] N. Reyren, S. Gariglio, A. D. Caviglia, D. Jaccard, T. Schneider, and J.-M. Triscone, Anisotropy of the superconducting transport properties of the $LaAlO_3/SrTiO_3$ interface, Applied Physics Letters **94**, 112506 (2009).
[S25] Z. Zhong, A. Tóth, and K. Held, Theory of spin-orbit coupling at $LaAlO_3/SrTiO_3$ interfaces and $srtio_3$ surfaces, Phys. Rev. B **87**, 161102(R) (2013).
[S26] Y. Kim, R. M. Lutchyn, and C. Nayak, Origin and transport signatures of spin-orbit interactions in one- and two-dimensional $srtio_3$-based heterostructures, Phys. Rev. B **87**, 245121 (2013).
[S27] R. Bistritzer, G. Khalsa, and A. H. MacDonald, Electronic structure of doped d^0 perovskite semiconductors, Phys. Rev. B **83**, 115114 (2011).
[S28] A. Joshua, S. Pecker, J. Ruhman, E. Altman, and S. Ilani, A universal critical density underlying the physics of electrons at the laalo3/srtio3 interface, Nature communications **3**, 1129 (2012).
[S29] S. LaShell, B. A. McDougall, and E. Jensen, Spin splitting of an au(111) surface state band observed with angle resolved

photoelectron spectroscopy, Phys. Rev. Lett. **77**, 3419 (1996).
[S30] L. Petersen and P. Hedegård, A simple tight-binding model of spin–orbit splitting of sp-derived surface states, Surface Science **459**, 49 (2000).
[S31] M. Briggeman, H. Lee, J.-W. Lee, K. Eom, F. Damanet, E. Mansfield, J. Li, M. Huang, A. J. Daley, C.-B. Eom, P. Irvin, and J. Levy, One-dimensional Kronig–Penney superlattices at the LaAlO 3/SrTiO 3 interface, Nature Physics , 1 (2021).
[S32] D. L. Maslov and M. Stone, Landauer conductance of luttinger liquids with leads, Phys. Rev. B **52**, R5539 (1995).
[S33] J. Settino, R. Citro, F. Romeo, V. Cataudella, and C. Perroni, Ballistic transport through quantum point contacts of multiorbital oxides, Physical Review B **103**, 235120 (2021).
[S34] A. D. Caviglia, M. Gabay, S. Gariglio, N. Reyren, C. Cancellieri, and J.-M. Triscone, Tunable rashba spin-orbit interaction at oxide interfaces, Phys. Rev. Lett. **104**, 126803 (2010).
[S35] M. Ben Shalom, M. Sachs, D. Rakhmilevitch, A. Palevski, and Y. Dagan, Tuning spin-orbit coupling and superconductivity at the $srtio_3/laalo_3$ interface: A magnetotransport study, Phys. Rev. Lett. **104**, 126802 (2010).
[S36] C. Mittag, M. Karalic, Z. Lei, C. Thomas, A. Tuaz, A. T. Hatke, G. C. Gardner, M. J. Manfra, T. Ihn, and K. Ensslin, Gate-defined quantum point contact in an InAs two-dimensional electron gas, Physical Review B **100**, 075422 (2019).
[S37] A. P. Micolich, What lurks below the last plateau: experimental studies of the $0.7\times 2e^2/h$ conductance anomaly in one-dimensional systems, Journal of Physics: Condensed Matter **23**, 443201 (2011).
[S38] W. Hew, K. Thomas, M. Pepper, I. Farrer, D. Anderson, G. Jones, and D. Ritchie, Spin-incoherent transport in quantum wires, Physical Review Letters **101**, 036801 (2008).
[S39] E. Mikheev, B. Himmetoglu, A. P. Kajdos, P. Moetakef, T. A. Cain, C. G. Van de Walle, and S. Stemmer, Limitations to the room temperature mobility of two-and three-dimensional electron liquids in $SrTiO_3$, Applied Physics Letters **106**, 062102 (2015).
[S40] K. Ueno, S. Nakamura, H. Shimotani, A. Ohtomo, N. Kimura, T. Nojima, H. Aoki, Y. Iwasa, and M. Kawasaki, Electric-field-induced superconductivity in an insulator, Nature Materials **7**, 855 (2008).
[S41] M. Lee, J. R. Williams, S. Zhang, C. D. Frisbie, and D. Goldhaber-Gordon, Electrolyte gate-controlled Kondo effect in $SrTiO_3$, Physical Review Letters **107**, 256601 (2011).